The Dissertation Committee for Liang Zhang
certifies that this is the approved version of the following dissertation:

Theoretical Study of Correlation Between Structure and Function for Nanoparticle Catalysts

Committee:

Graeme A. Henkelman, Supervisor

Richard M. Crooks

Charles Buddie Mullins

Dmitrii E. Makarov

Gyeong S. Hwang

Theoretical Study of Correlation Between Structure and Function for Nanoparticle Catalysts

by

Liang Zhang, B.S.

DISSERTATION

Presented to the Faculty of the Graduate School of
The University of Texas at Austin
in Partial Fulfillment
of the Requirements
for the Degree of

DOCTOR OF PHILOSOPHY

THE UNIVERSITY OF TEXAS AT AUSTIN
December 2014

Dedicated to my parents and my dear wife Ting.

Acknowledgments

Most of all, I wish to give special thanks to my advisor, Graeme Henkelman, for his insightful guidance and endless patience on my research. I wrote this dissertation in case that ”hotpot” will be the only thing Graeme could recall of me after many years. Professor Richard Crooks has also been very nice to work with. Collaboration between two groups as a joint team has promoted my knowledge and understanding in my research. I am grateful to all my co-authors and collaborators. I want to thank all my colleges for sharing the research ideas and tips of working with Graeme, such as absence without being noticed. Penghao Xiao has been a good deskmate and did an excellent job to keep me productive by putting on his earbuds when I chattered to him.

Lastly I would like to thank my parents and loving wife Ting for supporting my pursuit of science. I feel so sorry that all my accomplishments came from your sacrifices of my companion.

Theoretical Study of Correlation Between Structure and Function for Nanoparticle Catalysts

Publication No. __________________

Liang Zhang, Ph.D.
The University of Texas at Austin, 2014

Supervisor: Graeme A. Henkelman

The science and technology of catalysis is more important today than at any other time in our history due to the grand energy and environment challenges we are facing. With the explosively growth of computation power nowadays, computer simulation can play an increasingly important role in the design of new catalysts, avoiding the costly trail-and-error attempts and facilitating the development cycle. The goal to inverse design of new materials with desired catalytic property was once far off, but now achievable. The major focus of this dissertation is to find the general rules that govern the catalytic performance of a nanoparticle as the function of its structure.

Three types of multi-metallic nanoparticles have been investigated in this dissertation, core-shell, random alloy and alloy-core@shell. Significant structural rearrangement was found on Au@Pt and Pd@Pt nanoparticle, which is responsible for a dramatic improvement in catalytic performance. Nonlinear binding trends were found and modeled for random alloy nanoparticles,

providing a prescription for tuning catalytic activity through alloying. Studies of ORR on Pd/Au random alloy NP and hydrogenation reaction on Rh/Ag random alloy NP revealed that binding on individual ensemble should be investigated when large disparity of adsorbate affinity is presented between two alloying elements. In the alloy-core@shell system, I demonstrated a general linear correlations between the adsorbate binding energy to the shell of an alloy-core@shell nanoparticle and the composition of the core. This relationship allows for interpolation of the properties of single-core@shell particles and an approach for tuning the catalytic activity of the particle. A series of promising catalysts were then predicted for ORR, HER and CO oxidation.

As a first attempt to bridge the material gap, bimetallic nano cluster supported on $CeO_2(111)$ was investigated for CO oxidation. A strong support-metal interaction induces a preferential segregation of the more reactive element to the NC-CeO_2 perimeter, generating an interface with the Au component. (Au-Cu)/CeO_2 was found to be optimal for catalyzing CO oxidation via a bifunctional mechanism. O_2 preferentially binds to the Cu-rich sites whereas CO binds to the Au-rich sites. A method called distributed replica dynamics (DRD) is proposed at last to utilize enormous distributed computing resources for molecular dynamics simulations of rare-event in chemical reactions. High efficiency can be achieved with an appropriate choice of N_{rep} and t_{rep} for long-time MD simulation.

Table of Contents

List of Figures

List of Tables

Chapter 1

Introduction

This thesis contains the work I completed with my supervisor, Graeme Henkelman, during my Ph.D. in the physical chemistry division at the University of Texas at Austin. Chapter 2-4 contain the theoretical part of our collaborations with experimental studies by Crooks group (David F. Yancey, Rachel M. Anderson and Ravikumar Iyyamperumal) and Humphrey group (Stephany Garcia) on core-shell, random alloy and alloy-core@shell nanoparticles. Hyunyou Kim was the main motivator behind the supported bimetallic project in Chapter 5. Chapter 6 presents a method collaborated with Samuel T. Chill for accelerated dynamical simulation on distributed machines. This introduction gives a brief review of some general concepts and backgrounds related to these chapters.

1.1 Nanoparticle for Catalysis

The science and technology of catalysis is more important today than at any other time in our history due to the grand energy and environment challenges we are facing. Catalytic processes play an extremely important role in energy conversion, emission control, medicine development and synthesis of a wide variety of new materials. A catalyst by definition is a substance that facilitate the transformation of reactants to products throughout a repeated cycle of elementary steps in which the last step regenerates the catalyst to its original form. With the development of nano-science since1990s, nanoparticles catalysis clearly emerged as an important domain with large research interest.

The most straight forward benefit of size reduction for catalyst is the dramatic enhancement of surface to volume ratio, which leads to an increase of specific activity. On top of this apparent advantage, size reduction to nano-scale tunes the particular intrinsic properties of materials that render them very promising candidates for various application, as shown in Figure 1.1(Taken from Ref[1]). However, this tuning of catalytic property may be limited by the natural of the element itself. For instance, in most of the cases, the reduction of size strengthens the adsorbate-metal interaction. This one-way tuning could worsen the poisoning and over-binding issue suffered by those reactive elements. Alloy nanoparticles offers additional freedom of composition variation that allows to tune the properties of a nanoparticle with respect to mono-metallic counterpart. In certain cases, alloy particles could exhibit catalytic properties that are different to and beyond the corresponding pure materials. The general principles governing the reactivity of metal surfaces and applications to catalysis have been reviewed by Groß[3, 4] and in a recent comprehensive survey by Nørskov *et al*[5].

One of the main objects of studies presented in this thesis is to correlate the structure and catalytic function of multi-metallic nanoparticles comprised

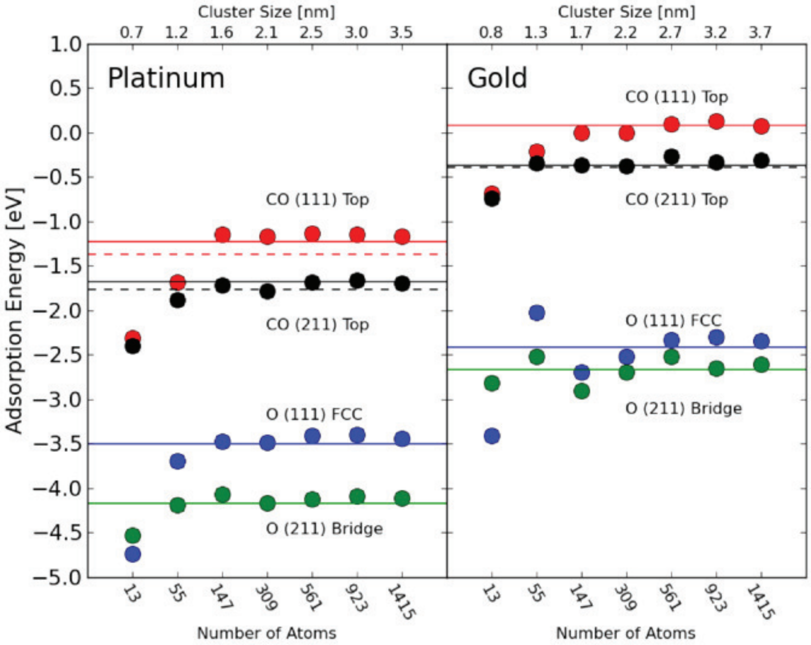

Figure 1.1: O and CO binding as a function particle size, taken from Ref[1]

of 100-200atoms. With the establishment of this correlation and increasing computation power, one can inverse-design new nanoparticles with desired catalytic property, reduce costly trail-and-error effort, and shorten the design cycle to facilitate rapid development of new materials.

1.2 Theoretical Models for Studying Catalytic Activity

There has been a tremendous amount of theoretical work successfully modeling the catalytic activity of as a function of the reactant adsorption energy on the single crystal metal and oxide surface, pioneered Nørskov and others. As a descriptor of reactivity of multi-metallic systems, the adsorbate binding energy (mainly O) is used to study the correlation between structure and the catalytic function of nanoparticle. *d*-band model is a simple but effective concept in understanding the interaction between adsorbate and substrate developed by Hammer and Nørskov, where the interaction strength is modeled as the overlap between metal *d*-band and adsorbate's frontier orbital. Details about the two above theoretical frameworks are given below.

1.2.1 Activity Volcano and Reaction Descriptors

In the past decade, much work has been done to reduce the number of parameters used to describe the activity of complex reactions. Nørskov *et al.* proposed a systematic method to construct the Sabatier rate as a function of one or two key reactants' binding energy using mean-field micro-kinetic models[6, 5, 7]. The Sabatier rate is set to the minimum of all forward rates. It provides an upper limit of the overall reaction rate, where all coverages of surface species are optimal for each elementary step. Strictly, surface species adsorption energy and activation energy of each elementary step is needed to construct the Sabatier rate. However, two single but quite general simplifications can be applied at this stage to reduce the effective parameters of this Sabatier rate model. They are, namely, the adsorption energy scaling[8, 9] and Brønsted-Evans-Polanyi (BEP) relationships[6].

The adsorption energy scaling relations show that, over a variety of metal and metal oxide surface, there is a good linear correlation between the adsorption energy of electronically similar adsorbates with the same binding environment and center, such as C *vs* CH_n (n=1, 2, 3), OH *vs* OOH, N *vs*

NH_n (n=1, 2). The scaling slope was also found to be a function of available valence bonds to form. For example, C can form 4 bonds to be saturated while CH_3 only has one, thus, the slope of $\Delta E_{\mathrm{CH_3}}$ to ΔE_{C} is about 1/3. OH and OOH both have one bond to form, thus difference between binding of OH and OOH is expected to be constant. While the scaling slope is independ of the surface, the intersection is dependent on the surface structure. The BEP relationship, somehow is a related concept to the above adsorption energy scaling relation, considering the transition state as an intermedia between reactant and product. This linear correlation between activation energies and reaction energies has been found to hold for heterogeneous catalysis ever since 1928 first proposed by Brønsted, as stated in Eq 1.1

$$E_a = \gamma \Delta E + \zeta \tag{1.1}$$

where E_a is the activation energy, ΔE is the energy of the chemisorbed final state of the reaction. Thus the stronger binding of the final state, the lower of the activation barrier.

The Sabatier Principle states that the catalytic acidity for a given reaction follows a volcano curve. Too nobel surface suffers the dissociation or adsorption of reactants, while too reactive surface is limited by the release of product. Since the activation barrier and surface species binding can be approximated by the scaling relation and BEP relationship, the Sabatier rate can be constructed as a function of one or two key reactants' binding energy, which are called the descriptors of the reaction. For instance, O binding was found to be an effective descriptor for oxygen reduction reaction (ORR)[10, 11, 12, 13].

1.2.2 *d*-band Model

The *d*-band model proposed by Hammer and Nørskov has been widely used to understand trends in chemisorption of adsorbates on transition-metal surface[14, 15, 16]. In this model, interaction between the metal surface and the adsorbate molecule is described as a function of the *d*-band of the metal. The detailed parameters that determine the chemisorption energy E are shown in Equation 1.2:

$$E \sim -2(1-f_d)\frac{V^2}{|\epsilon_d - \epsilon_a|} \tag{1.2}$$

where f_d is the local filling of the metal *d*-states, ϵ_d and ϵ_a are the centers of the metal *d*-band and the renormalized adsorbate states, respectively, and V^2 is the coupling matrix element between the adsorbate states and the metal *d*-states.

When a shift in *d*-band center of metal surface is the dominant factor determining chemisorption strength, a differential change in chemisorption energy is linearly correlated to the shift in the position of *d*-band center[16, 17]. For instance, in the case of transitional metal(M)-O chemisorption energy E , this linear relationship can be expressed as

$$\delta E_{\mathrm{M-O}} \simeq -4 f_d \frac{V^2}{|\epsilon_d - \epsilon_{\mathrm{O}}|^2}\ \delta\epsilon_d \tag{1.3}$$

where f_d is the local filling of the metal *d*-states, ϵ_{O} is the center of the oxygen $2p$ states, and V is the coupling matrix element between the oxygen $2p$ orbitals and metal *d*-states. When comparing similar binding geometries, changes in

f_d and V can be small as compared to the d-band center shift so that in a small range of ϵ_d, the slope $\delta E_{\mathrm{M-O}}/\delta\epsilon_d$ can be approximated as a constant. When d-band center is lowered from the Fermi-level (E_F), there is less overlap between the d-states of the surface M atoms and the $2p$ states of the adsorbed O, resulting in weaker O binding.

To better understand the relationship between the d-band center and core composition, it is helpful to determine the factors which affect the d-band center. In the discussion by Tang *et al.* on core-shell nanoparticles[18], it was found that changes of d-band filling and d-band width are two important factors that shift the d-band center. Change of the d-band filling is mainly due to charge redistribution between the surface atoms and the alloy core; change of the d-band width is attributed to bond-length variation in the surface (the strain effect) and electronic overlap with subsurface alloy atoms (the ligand effect).

Strain changes the metal-metal distance, and hence, the d-orbital overlap between neighboring atoms. Compression increases d-orbital overlap and widens the d-band width, whereas expansion reduces the d-orbital overlap and narrows the d-band width. The effect of d-band widening δw on the shift of the d-band center can be estimated in a rectangular model of the d-band[19]. The correlation between these two d-band character parameters is given by

$$\delta\epsilon_d = \sqrt{12}(0.5 - f_d)\delta w \tag{1.4}$$

Charge transfer shifts the metal d-band center by changing the Fermi level of the surface. When metals with different Fermi levels (e.g. Pd and Cu) are brought together, charge density shifts between two metals. A new Fermi level is formed and expected to be the intermediate between two original Fermi levels. In this way, the *d*-band center is shifted with respect to the Fermi level.

1.2.3 Oxygen Reduction Reaction

Fuel cells show promise as a future power source that combines the high chemical energy density of fuels with high efficiency conversion to electricity and zero or low emissions. The widespread application of current proton exchange membrane fuel cells, however, is impeded by several limitations in the oxygen reduction catalyst at the cathode. As the best catalyst for the oxygen reduction reaction (ORR) so far, Pt-based materials still have some deficiencies, such as slow oxygen reduction kinetics and a high material cost, preventing them from being commercially valuable in large-scale (e.g. automotive) applications.

Bligaard *et al.* reported that O binding energy is an effective descriptor for ORR activity[6]. Nørskov *et al.* showed a volcano-shaped relationship between the ORR rate and the oxygen adsorption energy[2]. On one side of the volcano peak, O or OH strongly binds to the metal so that the reaction rate is limited by the removal of product (hydroxyl). On the other side of the peak, oxygen binds weakly to metals such as Ag and Au, and the kinetics are limited by high dissociation barriers. According to the volcano plot, the peak in activity is predicted to be at an oxygen binding slightly weaker than on a

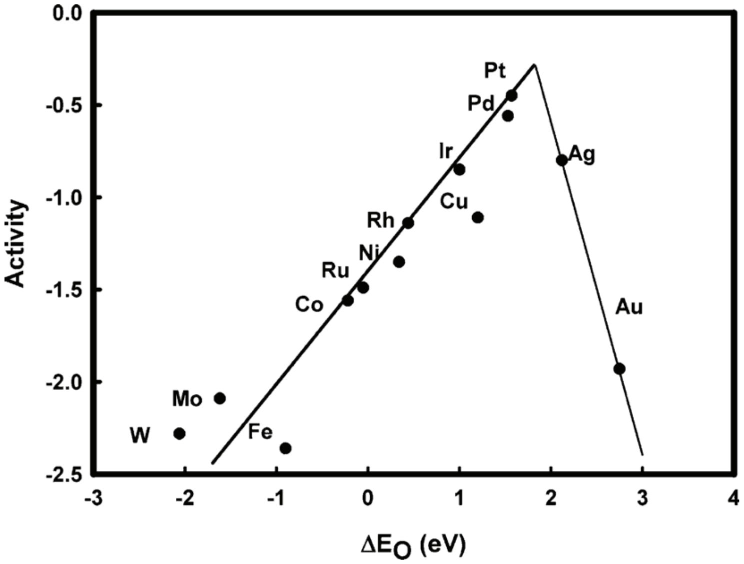

Figure 1.2: Volcano Plot of ORR taken from Ref [2] shows how the activity of catalysts is related to the binding energy of the products. Highly reactive metals on the left bind O too strongly, whereas noble metals on the right have high activation energies. Pt has the optimal balance for O_2 reduction.

Pt(111) surface. In this paper, we choose a target oxygen binding energy of the Pt(111) surface, -1.51 eV, which is calculated on a 4 layer 3×3 slab model using a half of a free O_2 molecule as reference energy. Although oxygen binding on bulk Pt(111) is not necessarily the optimal for ORR, it gives a close enough estimate of the location of the volcano peak to understand trends in nanoparticle activity.

In this thesis, ORR is selected as the model reaction to study the structure-function correlation of different alloy nanoparticle systems.

1.3 DENs as Model Catalysts

The work presented in this thesis about nanoparticle catalysis collaborated tightly with experiment group lead by Prof. Richard Crooks, where dendrimer-encapsulated nanoparticles (DENs), as a model system, are synthesized and characterized at atomic level for direct comparison with theory.

DENs are synthesized by sequestering metal ions within the interior of poly(amidoamine) (PAMAM) dendrimers, followed by chemical reduction of the metal-ion/dendrimer complex with a reducing agent such as borohydride[20, 21, 22, 23]. DENs are good model catalysts for the following reasons. First, their size, composition, and structure can be precisely controlled[24, 25]. Second, the dendrimers stabilize the encapsulated nanoparticles and provide a handle for linking them to an electrode surface, but they do not interfere significantly with reactions on the particle surface[26]. Third, DENs are in a size range (1∼2 nm diameter) that makes it possible to directly compare theoretical and experimental results from structural and catalytic studies.

Figure 1.3 illustrates the synthesis routes of mono-metallic[27], core-shell[28, 29, 30, 31], random alloy[32, 25, 33, 34, 35] and alloy-core@shell DENs[36]. As shown in Figure 1.3 (a), the synthesis of mono-metallic DENs consists in two steps, including the complexation of ligand sites in the dendrimers by transition metal cations, and reduction of these cation to metal atoms that further agglomerate into metallic nanoparticle inside the dendrimer. Multi-metallic DENs can be synthesized on this basis. Random alloy DENs can be prepared by co-complexation method, where two types of metal cations are reduced simultaneously to form an alloy particle (see Figure 1.3 (b)). Core-shell nanoparticles are usually produced *via* a post-synthesis of mono-metallic DENs with core metal. As illustrated in Figure 1.3 (c) and (d), shell atoms can be deposited on the core cluster by sequential reduction or under potential deposition (UPD)[37, 38, 39]. Similar approach can be applied to a pre-synthesized random-alloy DENs to form a alloy-core@shell DENs (see Figure 1.3 (e)). Galvanic exchange also known as redox displacement reaction is elegant and useful to replace reactive metals of the DENs with a relative noble element, increasing the varieties of shell types available in DENs synthesis.

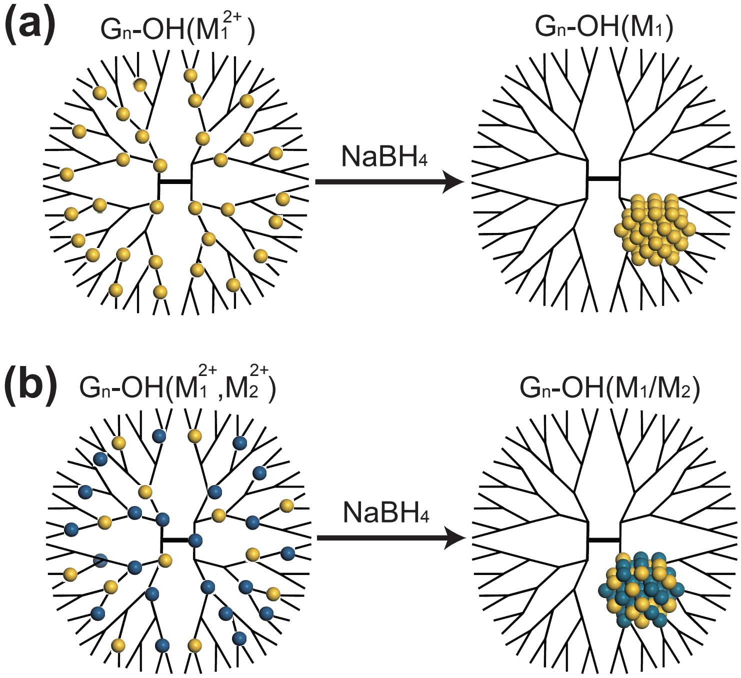

Figure 1.3: Routes to synthesize different metallic DENs (a)mono-metallic (b) random alloy.

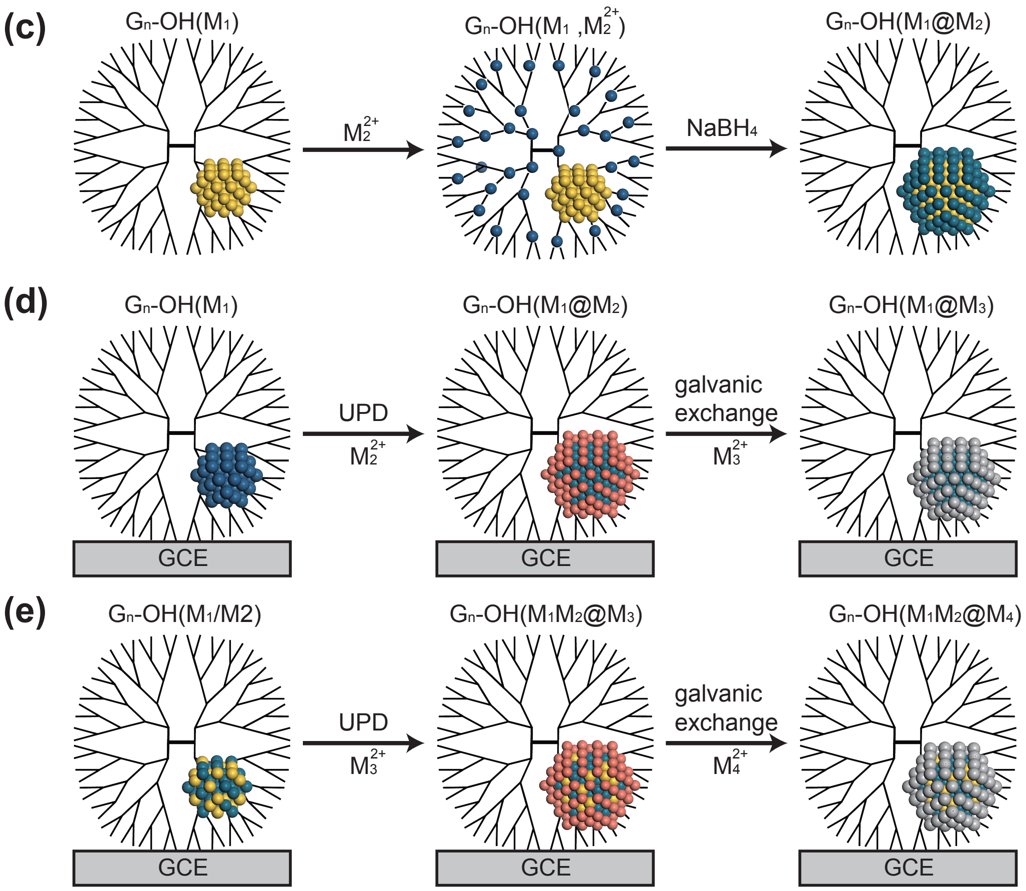

Figure 1.3: Routes to synthesize different metallic DENs. (c) core-shell via sequential reduction (d)core-shell *via* UPD and subsequent galvanic exchange (e)alloy-core@shell via UPD and subsequent galvanic exchange on random alloy core cluster

Chapter 2

Core-shell Nanoparticles for Catalysis

2.1 Abstract

Core-shell nanoparticles is a class of near surface alloy catalyst. Previous studies have shown that the catalytic activity of such nanoparticles can be generally tuned by varying the core and shell metal combination. In this chapter, two systems where nanoparticles exhibit unusual structure deformation were studied with both theory and experiment, demonstrating the power of theory-experiments collaboration in correlating the structure and function of core-shell nanoparticles. Structure deformation of Au_{147}@Pt was found to efficiently promote electro-catalytic oxidation of formic acid. Unconventional Core-shell inversion found on Pd_{147}@Pt was examined and explained by theory.

2.2 Introduction

As introduced in Section 1.3, DENs are good model catalyst that have well defined structures, compositions and sizes. Core@shell nanostructures are important because they exhibit tunable properties arising from the ability of the core metal to influence the properties of the shell[18, 40, 41, 42, 43].

This phenomenon has been applied to electrocatalytic[41, 42, 44] and spectroscopic applications[43]. Early examples demonstrating the importance of Pt-shell nanoparticles as active electrocatalysts for the ORR were reported by Adzic and coworkers[41, 42]. The relationship between bimetallic nanoparticle structure and catalytic activity has been correlated to DFT calculations by a number of groups[44, 45, 46, 47].

Synthesis of core-shell DENs is usually done in a manner of sequential systhesis. In the first step, monometallic DENs consisted by core element is clustered in the dendrimer template. After that, shell atoms are deposited on the core cluster by either chemical reduction or (illustrated in Figure 1.3). UPD originally developed by Adzic group provides a systematic scheme to generate a well-defined monolayer shell. Chemical reduction has less control of the shell thickness but is able to cover low-coordinated sites (corner/edge) that are usually exposed in UPD. Moreover, subsequent galvanic exchange can be used to prepare core-shell DENs that are difficult to synthesize by the above means. For instance, Pt shell is hard to be introduced to Au DENs. However Au@Pt DENs can be obtained by galvanic exchange of under potential deposited Pb on Au@Pb with Pt^{2+}.

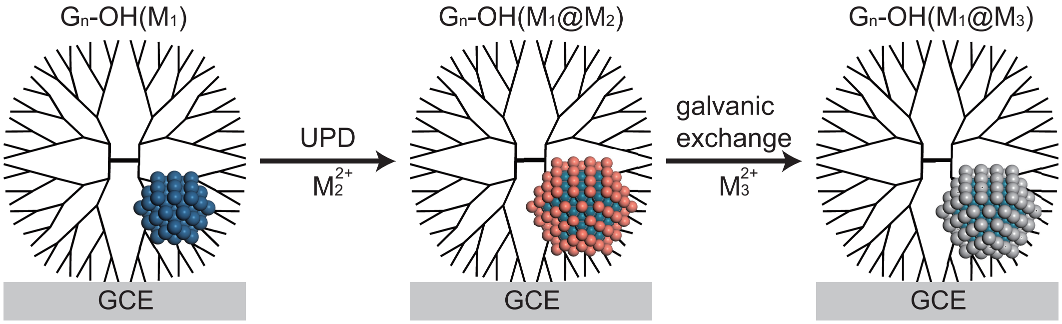

Figure 2.1: Synthesis procedure of core-shell DENs

Pb UPD onto bulk Au surfaces, as well as onto Au nano- structures, has been studied extensively by Feliu and coworkers[39, 38, 37]. They have shown that Pb UPD onto Au is a surface-selective reaction and that the morphology of the Au surface can be determined by analyzing voltammetric UPD peaks. With regard to nanoparticles, Feliu and his group have shown that the location of voltammetric Pb UPD peaks for well- defined single-crystal surfaces can be related to peak positions derived from nanoparticles, and that this correspondence can be used to help elucidate details of nanoparticle surface structure[39]. One fact to emerge from these studies is that Pb UPD occurs on the low-index faces of Au in the following order: first Au(110), then Au(100), and finally Au(111)[39].

Formic acid is used as a substitute fuel for hydrogen in proton exchange membrane fuel cells (PEMFCs), because oxidation of hydrogen and formic acid occurs at similar thermodynamic potentials[48]. Electro-oxidation of HCOOH to CO_2 on Pt electrocatalysts occurs via two mechanisms: (1) through formation of a reactive intermediate (direct oxidation pathway), and (2) through formation of CO_{ads} and subsequent oxidation of CO_{ads} to CO_2 (indirect oxidation pathway)[49]. The second pathway is problematic, because CO_{ads} poisons the Pt surface. However, it has been shown that the presence of Au can improve the CO tolerance of Pt, and hence its catalytic performance[50, 51, 52]. For example, Xu and co-workers found that Au@Pt nanoparticles having submonolayer Pt shells exhibit improved electro-catalytic activity for formic acid oxidation due to specifically engineered electronic interactions between the two metals[53]. An alternative to improving CO tolerance is to simply avoid CO altogether. For example, Masel and co- workers found that carbon-supported Pd is highly active for formic acid oxidation, because it favors the direct oxidation pathway[54]. However, Pd/C suffers significant loss in activity during formic acid oxidation due to slow adsorption of CO-like intermediates, bridge-bonded formate, perchlorate, and other anions[55].

It has been reported that Pd@Pt nano- particles exhibit enhanced electrocatalytic activity for the oxygen reduction reaction (ORR) compared to monometallic Pt catalysts[56, 41, 57]. Techniques such as high-resolution scanning transmission electron microscopy (HR-STEM)[58], Fourier-transform infrared spectroscopy (FT-IR)[59, 60], and EXAFS[61, 62] have been used to investigate the structure and structural stability of Pd@Pt nanoparticles within the size range of 2.0$\sim$5.0 nm. For example, Chen and co-workers prepared 4.5 nm Pd@Pt nanoparticles using a surface-limited-growth procedure. This is a three-step synthesis in which (1) Pd nanoparticles are exposed to hydrogen, thereby forming a PdH shell; (2) Cu^{2+} is reduced onto the Pd surface via cross reaction with the hydride; and (3) the Pd_{147}@Cu_{162} nanoparticles are exposed to Pt^{2+}, which leads to galvanic exchange and formation of the final ∼4.5 nm product having a Pd core and an ultrathin Pt shell[61]. We used a synthetic strategy similar to this in the present study to prepare ∼2 nm $Pd_{147}Pt_{162}$ DENs.

2.3 Computation Models and Methods

DFT was used to calculate the deposition process of Pb UPD on Au_{147} as well as the structures and oxygen binding energies to the Au_{147}@Pt_n particles. All calculations were performed with the VASP code[63, 64] where electron correlation was evaluated within the generalized gradient approximation using the PW91 functional[65]. Core electrons were described with the projector augmented-wave method[66, 67]. KohnSham wave functions for the valence electrons were expanded in a plane wave basis set with an energy cutoff of 250 eV. The energy cutoff was increased to 400 eV to test for convergence, and oxygen binding energies were found to vary by less than 0.01 eV. Spin polarization was tested and used as required.

The Au_{147} particles were modeled as face-centered cubic (FCC) crystallites in the shape of a cuboctahedron having 6 (100) facets and 8 (111) facets. The structures of Au_{147}@Pb and Pd_{147}@Pt were built by attaching atoms on the facets of the Au nanoparticles. In all calculations, the nanoparticles were isolated in a cubic box having edge lengths of 28 Å. The vacuum gap in all directions was large enough to avoid artificial interactions between periodic images. The Pt_{162}@Pt_{162} nanoparticles were modeled as 309 atom FCC crystallites in the shape of a cuboctahedron with 147 core atoms and 162 shell atoms, which is consistent with the size of the synthesized DENs.

2.4 Au_{147}@Pt Nanoparticle: structure and catalysis

In this section, we report the electrochemical synthesis of core@shell dendrimer-encapsulated nanoparticles (DENs) consisting of cores containing 147 Au atoms (Au_{147}) and Pt shells having 54 or 102 atoms (Au_{147}@Pt_n(n= 54 or102)). DFT calculations show that Pb binding is stronger on the (100) facets of Au as compared to (111), and the calculated deposition and stripping potentials are consistent with those measured experimentally. Galvanic exchange is used to replace the surface Pb atoms with Pt, and a surface distortion is found for Au_{147}@Pt_n particles using molecular dynamics simulations in which the Pt-covered (100) facets shear into (111) diamond structures. DFT calculations of oxygen binding show that the distorted surfaces are the most active for the ORR, and that their activity is similar regardless of the Pt coverage. These calculations are consistent with rotating ring-disk voltammetry measurements.

2.4.1 Pb UPD onto Au_{147} DENs

Pb UPD was modeled on Au_{147} particles using DFT calculations. First, the stability of Pb monolayers on the (100) and (111) facets was investigated by comparing two models. In the first model, each of the 6 Au(100) facets were covered with 9 Pb atoms. In the second model, each of the 8 Au(111) facets were covered with 6 Pb atoms. The average adsorption energies of the above two models were calculated using Eq. 2.1.

$$< E_{ad} >= \frac{1}{N}(E_{\mathrm{Au_{147}Pb}_n} - E_{\mathrm{Au}_{147}} - nE_{\mathrm{Pb}}) \qquad (2.1)$$

Here, N is the number of Pb atoms on the shell (54 in the first model and 48 in the second), $E_{\mathrm{Au_{147}Pb}_n}$ is the energy of the Au_{147}-core Pb-shell particle, $E_{\mathrm{Au}_{147}}$ is the energy of the bare Au_{147} particle, and E_{Pb} is the energy of one Pb atom in the bulk metal. Using Eq. 2.1, the average adsorption energy on the (100) facet was found to be 0.1eV per Pb atom stronger than on the (111) facet, showing that Pb adlayers on (100) are more stable than those on the (111) facet. This finding is consistent with an increase in favorable Pb-Au bonding of Pb on the (100) facet as compared to the (111) facet, and hence our assignment of the UPD peaks shown in Fig. 2. Due to the high energies of the edge and corner sites, Pb UPD does not occur there. That is, the energy of adsorption of Pb on the edge or corner sites is weaker than the energy of adsorption of Pb on a bulk Pb surface.

To model the Pb UPD process in detail, an atom-by-atom deposition calculation was done. Pb atoms were successively added to the lowest energy site on the Au particle, and the particle was relaxed before the addition of the next atom. The adsorption energy of the n^{th} Pb atom, $E_{ad}(n)$, was calculated using Eq. 2.2.

$$E_{ad}(n) = E_{\mathrm{Au_{147}Pb}_n} - E_{\mathrm{Au_{147}Pb}_{n-1}} - E_{\mathrm{Pb}}) \qquad (2.2)$$

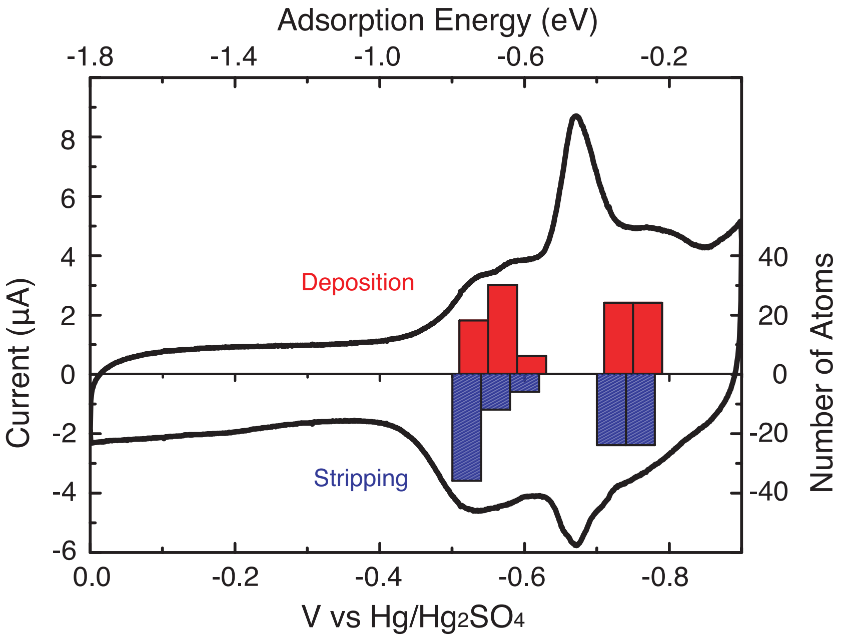

Figure 2.2: A cyclic voltammetry showing the Pb UPD process at a Au_{147} DEN-modified glassy carbon electrode. The DFT-calculated potentials for Pb deposition (red bars) and stripping (blue bars) are also shown

The calculated E_{ad} values of each successive Pb atom binding site on (100) and (111) facets are plotted in Figure 2.3The first (or lowest energy) binding sites on the Au_{147} particle are on the (100) facets. Once the (100) facet sites are covered, the next Pb atoms deposit on the (111) sites. This means that the order of facet decoration on Au_{147} is consistent with bulk Au and larger Au nanoparticles[37]. The values of E_{ad} were converted to potentials, $V_{\mathrm{Pb}}^{\mathrm{DFT}}$, for comparison with the experimental voltammograms. For this conversion, we assume that the binding energy per atom in bulk Pb corresponds to the onset potential of bulk Pb deposition. The DFT-calculated potential is given

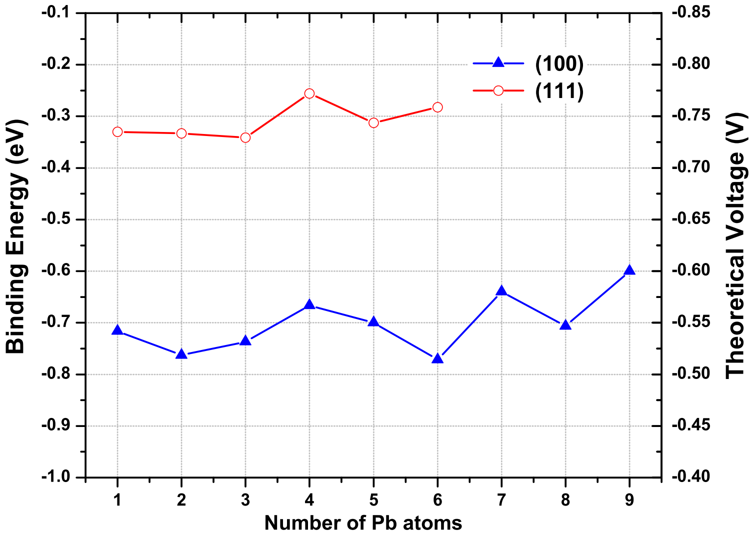

Figure 2.3: The calculated energies for Pb deposition onto the (100) (blue) and (111) (red) facets of Au_{147} DENs are plotted in terms of binding energy (left y-axis) and theoretical voltage (right y-axis). See Eq. 2.3 for the conversion between binding energy and the theoretical voltage of deposition.

by Eq. 2.3.

$$V_{\mathrm{Pb}}^{\mathrm{DFT}} = V_{\mathrm{Pb-bulk}}^{\mathrm{Exp}} - \frac{1}{2}E_{ad}(n) \tag{2.3}$$

Here $V_{\mathrm{Pb-bulk}}^{\mathrm{Exp}}$ is the experimentally measured Pb bulk deposition potential (-0.90 V vs Hg/Hg_2SO_4),and the factor of 1/2 accounts for the two-electron Pb deposition and stripping process.

Figure 2.2 compares a histogram of $V_{\mathrm{Pb}}^{\mathrm{DFT}}$ values for deposition and stripping of Pb atoms on Au_{147} with the UPD voltammogram. Based upon the order of deposition, and the separation of the peaks corresponding to UPD on the (100) and (111) facets, we constructed partially and fully covered models for the Au_{147}@Pb_n particles (left side of frames a and b, Figure 2.4). In the partially covered Au_{147}@Pb_{54} model, the 6 (100) facets of the Au_{147} core are covered by 9 Pb atoms. In the fully covered Au_{147}@Pb_{102} model, the Au_{147} core has an additional 6 Pb atoms on each of the 8 (111) facets.

2.4.2 Au_{147}@Pt_n (n=54 and 102) Structure and ORR Activity

For simplicity, Pb atoms were assumed to be directly replaced by Pt in the galvanic exchange process. MD simulations were carried out on the Au_{147}@Pt_{102} and Au_{147}@Pt_{54} particles for 10 ps at 350 K to allow them to escape from any shallow local minima. Forces from DFT were used for these dynamics, as well as in a subsequent minimization for comparison with the initial (Au_{147}@Pb_n) structures. Figure 2.4a shows the considerable deformation for the partial-shell structure induced by the short-time MD simulations, indicating the instability of the ordered structures upon substitution of the Pb shell atoms with Pt. The deformation has two distinct features: First, Au atoms in the sublayer rise to the surface edge sites. Second, the original square (100) Pt facets deform to diamond-shaped (111) facets. The relaxed Au_{147}@Pt_{54} particle is 0.2 eV per Pt atom lower in energy than the ordered structure. A similar distortion occurs on the full shell Au_{147}@Pt_{102} particle. The (100) ordered facets of the Au_{147}@Pt_{102} structure, shown in Figure 2.4b, spontaneously deform to diamond-shaped (111) facets.

To better understand these deformations, we calculated the (100) and (111) surface energies of Pt, Au, and a Pt monolayer on Au using 4-layer slab

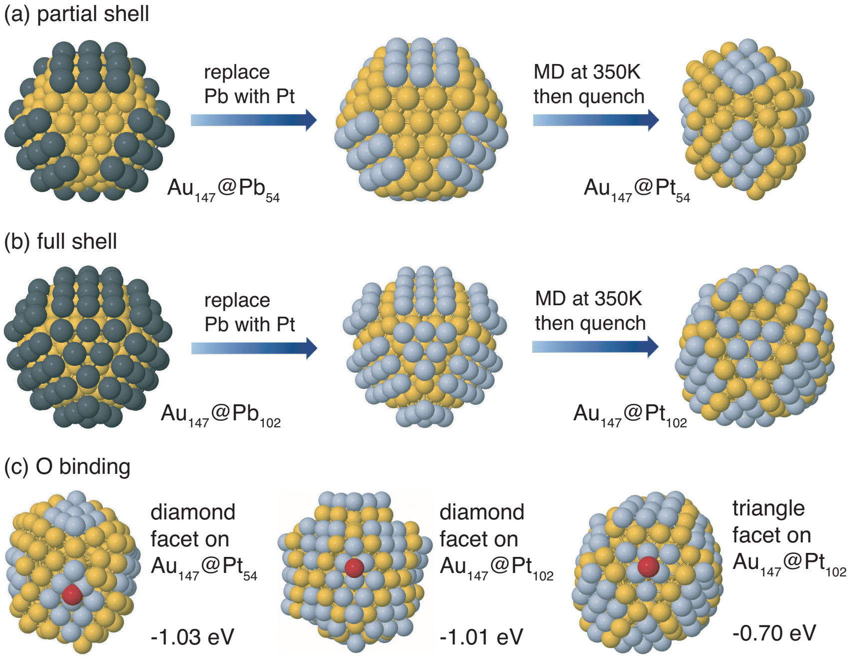

Figure 2.4: DFT-calculated structures for (a) Au_{147}@Pb_{54} and Au_{147}@Pt_{54} DENs and (b) Au_{147}@Pb_{102} and Au_{147}@Pt_{102} DENs. (c) Oxygen binding sites and energies for Au_{147}@Pt_{54} and Au_{147}@Pt_{102} DENs.

models containing 9 atoms per layer. The results indicate that the surface energy of Au(111) is 0.11 eV/atom lower (more stable) than that of Au(100), and Pt(111) is 0.25 eV/atom lower than Pt(100). Moreover, the cohesive energy of a Pt monolayer on Au(111) is 0.17 eV/atom lower than on Au(100). These two results account for the deformation of Pt-covered Au(100) facets to a (111) diamond structure by lowering of the Pt surface energy and increasing the stability of the particle.

To determine the catalytic activity of the Au_{147}@Ptn particles, we rely on the binding energy of O as a descriptor for ORR activity[2, 7]. A volcano plot analysis of the ORR shows that the O binding energy on Pt(111) is near optimal[2]. Figure 2.4c shows O binding to hollow sites on different Pt facets of $Au_{147}@Pt_{54}$ and $Au_{147}@Pt_{102}$. Oxygen binding to the deformed diamond (111) facets of the two nanoparticle structures have similar values of -1.03 and -1.01 eV, respectively. The triangular (111) facet of the $Au_{147}@Pt_{102}$ particle has an O binding energy that is 0.3 eV weaker. All of these O binding energies are weaker than for Pt(111), which was calculated with the slab model to be -1.51 eV. This is in contrast to other reported cases where a Pt monolayer on a Au surface leads to a lattice expansion of the Pt, and stronger binding of oxygen to the surface[68, 69, 70]. In the present case, Au atoms that rise to the surface during the structural reorganization actually compress the small Pt(111) domains. The PtPt bond length in the diamond-shaped domains, as calculated from the DFT structures of $Au_{147}@Pt_{54}$ and $Au_{147}@Pt_{102}$, is 2.65 Å, which is shorter than that of bulk Pt (Å). This compression of the PtPt bonds leads to a weaker binding of O on the nanoparticle Pt surface as compared to bulk Pt(111)[68, 69]. Because O binding on the nanoparticle facets is weaker than on Pt(111), the particle facets are too noble to give optimal activity, and the ORR mechanism is limited by OO dissociation. However, the diamond facets (with stronger O-binding) are expected to have a higher activity than the triangular facets, so it is the diamond facets that are active for the ORR on both the $Au_{147}@Pt_{102}$ and $Au_{147}@Pt_{54}$ particles. Note also that the nearly identical calculated O binding energy for these two structures is consistent with the experimentally determined specific ORR activities measured for the partial and full shell Au_{147}@Pt_n DENs (*vide supra*).

2.4.3 Au_{147}@Pt for Formic Acid Oxidation

Other than ORR, electro-oxidation of formic acid is another reaction of energy applications using Au_{147}@Pt synthesized in the above section. Electro-oxidation of formic acid to CO_2 on Pt electro-catalysts occurs via two mechanisms: (1) through formation of a reactive intermediate (direct oxidation pathway), and (2) through formation of CO_{ads} and subsequent oxidation of CO_{ads} to CO_2 (indirect oxidation pathway), potentially leading to the poisoning on the Pt surface. Figure 2.5 shows cyclic voltammograms for formic acid

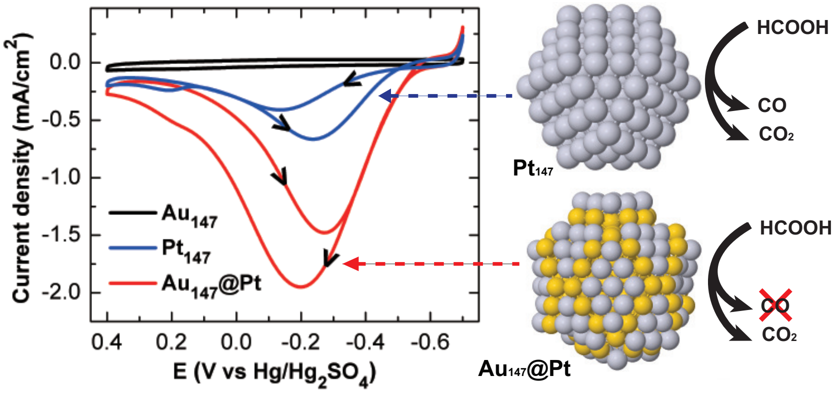

Figure 2.5: CVs for formic acid oxidation of Au_{147}, Pt_{147}, and Au_{147}@Pt DEN-modified GCEs in a N2-saturated aqueous electrolyte solution containing 0.10 M HClO4 and 0.10 M HCOOH. The scan rate was 50 mV/s, and the geometric area of the GCE was 0.071 cm^2. For the Pt_{147} and Au_{147}@Pt DENs, the current axis is normalized to the electrochemically active surface area of Pt as measured by H UPD. For the Au_{147} DENs, the current is normalized to the electrochemically active surface area of Au as measured by reduction of the Au oxide peak. Inserts show that Au_{147}@Pt suppresses the indirect pathway.

oxidation using Au_{147}, Pt_{147} and Au_{147}@Pt DEN-modified GCEs in 0.10 M HClO4 containing 0.10 M HCOOH. The Au_{147}@Pt DEN electrocatalysts display superior catalytic performance compared to the Pt_{147} DENs and a bulk, polycrystalline Pt electrode. This is demonstrated by the red CV shown in Figure 2.5 . There are four striking differences between this CV and the Pt-only CV. First, the peak at 0.2 V, which corresponds to oxidation of CO_{ads}, is nearly absent on the Au_{147}@Pt DENs. The fact that very little CO_{ads} on the bimetallic DENs indicates that formic acid is oxidized almost exclusively via the direct pathway on this electrocatalyst. Second, the Au_{147}@Pt electrocatalyst exhibits an onset potential (defined here as the potential at which the current density = 0.10 mA/cm^2)[71] for formic acid oxidation of -0.54 V, which is 0.14 and 0.20 V lower than for Pt_{147} DENs and a polycrystalline Pt electrode, respectively. Third, the maximum current density for direct formic acid oxidation is substantially higher for the Au_{147}@Pt DENs compared to either Pt_{147} DENs or the bulk, polycrystalline Pt electrode. The increased activity of the Au_{147}@Pt DENs results from the desirable electronic properties of the core@shell structure. Fourth, the peak current for the forward (positive-going) scan for the Au_{147}@Pt DENs is higher than for the reverse scan, which is the opposite of what is observed for the Pt_{147} DENs and for a bulk polycrystalline electrode. This is a consequence of a decrease in CO poisoning at the more negative potentials and differences in the rate of oxide formation and subsequent reduction at more positive potentials.

One of the most distinctive features of formic acid oxidation on Au_{147}@Pt

DENs is near-elimination of the indirect formic acid oxidation pathway. We hypothesized that the reduction in CO poisoning could arise from either of the following phenomena: (1) slowed dehydration of HCOOH, which eliminates formation of CO, or (2) weakening of the CO binding energy. With regard to the first hypothesis, as mentioned above, a surface distortion of Au_{147}@Pt was observed during molecular dynamics simulations in which the Pt-covered (100) facets sheared into a diamond (111) structure. We denote this deformed partial shell model as Au@Pt_{dps}. This distortion may play an important role in the rate of dehydration of HCOOH to CO on the DENs, because formation of CO during formic acid oxidation on Pt(111) single-crystal electrodes is not favorable[72, 73]. The second hypothesis was tested using DFT to calculate the CO binding energies on Pt_{147}, the Au@Pt_{dps} model, and a complete shell model of Au@Pt (Au@Pt_{cs}). These three structures, showing possible CO binding sites, are provided in Figure 2.6, and the corresponding CO binding

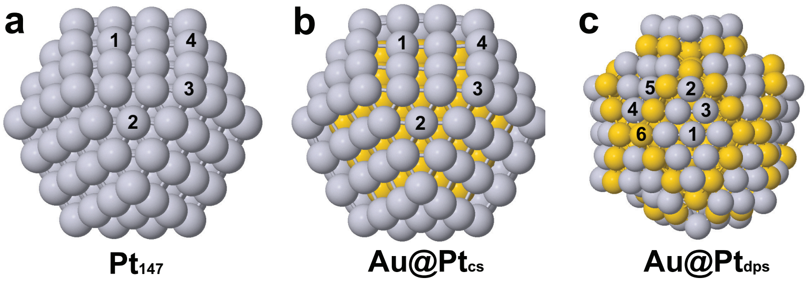

Figure 2.6: Optimized structures for (a) the Pt-only DEN model (Pt_{147}), (b) the complete shell model (Au@Pt_{cs}), which is equivalent to Au_{55}@ Pt_{92}, and (c) the deformed partial-shell model (Au@Pt_{dps}), which is equivalent to Au_{147}@Pt_{102}. The superimposed numbers represent possible CO binding sites for each model.

Table 2.1: CO Binding Energies(eV) for Different Sites on the Pt_{147}, Au_{55}@ Pt_{92}, and Au_{147}@Pt_{102} Model. D(111) and T(111) Denote the Diamond (111) and Triangle (111)

	Pt_{147}			Au@Pt_{cs}			Au@Pt_{dps}	
	sites	Eb_{CO}		sites	Eb_{CO}		sites	Eb_{CO}
1	(100)	-3.12	1	(100)	-3.34	1	D(111) center	-1.74
2	(111)	-2.65	2	(111)	-3.07	2	D(111) corner	-1.96
3	corner	-3.30	3	corner	-3.36	3	D(111) edge	-1.80
4	edge	-3.15	4	edge	-3.40	4	T(111)corner	-1.44
						5	T(111)edge	-1.37
						6	Au	-0.47

energies are listed in Table 2.1. The results indicate that Au@Pt_{cs} binds CO more strongly than Pt_{147}, which is in agreement with results from previous DFT calculations on bulk model surfaces and with temperature-programmed desorption experiments[74]. Importantly, however, the binding energy calculations reveal significant weakening of CO binding to Au@Pt_{dps}. These CO binding trends can be interpreted in terms of the average Pt-Pt bond lengths in the different models: Au@Pt_{cs}, 2.79 Å; Pt_{147}, 2.76 Å; and Au@Pt_{dps}, 2.65 Å. The compression of the Pt-Pt bond in Au@Pt_{dps} leads to weaker binding of CO on the Pt surface compared to either Pt_{147} or Au@Pt_{cs} DENs[74].

2.5 Core-shell Inversion of Pd@Pt DENs

Bimetallic PdPt DENs having sizes of about 2 nm were synthesized by a homogeneous route that involved (1) formation of a Pd core, (2) deposition of a Cu shell onto the Pd core in the presence of H2 gas. Unlike UPD, this approach ensures a homogenous complete shell covering the Pd core. (3) galvanic exchange of Pt for the Cu shell. Under these conditions, a ?Pd@Pt core@shell DEN is anticipated, but detailed characterization by in-situ EXAFS spectroscopy and other analytical methods indicate that the metals invert to yield a Pt-rich core with primarily Pd in the shell.

2.5.1 Coordination Numbers of Pd@Pt and Pd@Pt

The bottom part of Table 2.2 shows coordinating numbers (CNs) extracted from EXAFS data for the $Pd_{147}Pt_{162}$ final product. These data were obtained from the simultaneous first-shell fitting of the Pd and Pt edges. The experimentally determined CN values are compared to three theore- tical structures: $Pd_{147}@Pt_{162}$, a $Pd_{147}Pt_{162}$ alloy, and an inverted $Pt_{147}@Pd_{147}Pt_{15}$ structure. The EXAFS data were found to most closely match the inverted $Pt_{147}@Pd_{147}Pt_{15}$ structure. Most strikingly, the CN_{Pt-Pt} (10.9±3.7) is much larger than would be expected for a complete Pt shell (calculated CN_{Pt-Pt} = 4.7) or if the structure was alloyed (calculated CN_{Pt-Pt} = 5.0±0.2). Also, the total Pt-metal CN (CN_{Pt-M}) of 12.2 (the sum of CN_{Pt-Pt} and CN_{Pt-Pd}) is larger than the total Pd-metal CN (CN_{Pd-M}) of 7.4 (the sum of CN_{Pd-Pd} and CN_{Pd-Pt}). This implies that Pt is more fully coordinated than Pd, which would be expected if Pt is predominantly in the interior of the nanoparticle as surface atoms have fewer nearest neighbors[75].

Table 2.2: CNs Obtained from the Fitting of Experimental $Pd_{147}@Cu_{162}$ and $Pd_{147}Pt_{162}$ DENs EXAFS Data Compared to Calculated CNs of Model Structures. Alloy Values Are the Average of 20 Random Configurations.

$Pd_{147}Cu_{162}$	Exp	Calculated		
CN	$Pd_{147}Cu_{162}$	Pd@Cu	PdCu alloy	$Cu_{147}@Pd_{147}Cu_{15}$
Pd-Pd	7.8±0.7	9.0	4.6±0.2	4.1
Pd-Cu	1.7±0.9	3.0	5.1±0.2	3.3

$Pd_{147}Pt_{162}$	Exp	Calculated		
CN	$Pd_{147}Pt_{162}$	Pd@Pt	PdPt alloy	$Pt_{147}@Pd_{147}Pt_{15}$
Pd-Pd	4.8±1.1	9.0	4.6±0.2	4.1
Pd-Pt	2.6±1.2	3.0	5.1±0.2	3.3
Pt-Pt	10.9±3.7	4.7	5.0±0.2	8.7
Pt-Pd	1.3±0.6	2.7	4.6±0.2	3.0

2.5.2 Segregation Energy of $Pd_{147}Pt_{162}$ and Pd/Pt bulk

DFT calculations were used to better understand the observed inversion of $Pd_{147}Pt_{162}$ DENs. The thermodynamic stability of $Pd_{147}@Pt_{162}$ nanoparticles was evaluated using the segregation energy (E_{seg}), which is the energy required to swap a shell atom with its neighboring Pd-core atom. Figure 2.7 illustrates the computation models of segregation energy at (111) facet of

$Pd_{147}@Cu_{162}$ and $Pd_{147}@Pt_{162}$. Negative values of E_{seg} correspond to favorable exchange of atoms between the shell and core. The effect of an aqueous environment was taken into consideration by adsorbing a hydroxyl group (OH) to surface sites neighboring the swapped atom. Because Cu binds OH more strongly than Pd, the Cu shell is stabilized and the $Pd_{147}@Cu_{162}$ structure is predicted to be stable. This is the same result found in the aforemen tioned experiments.

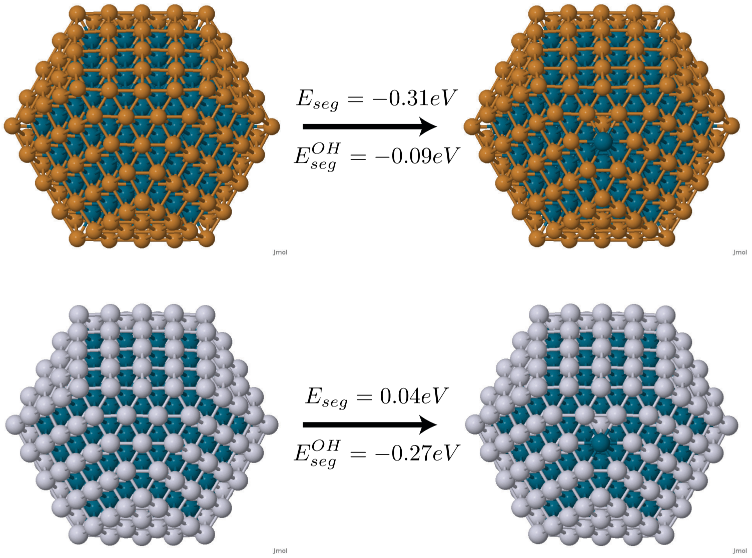

Figure 2.7: Computation models of segregation energy at (111) facet of $Pd_{147}@Cu_{162}$ and $Pd_{147}@Pt_{162}$

Here we focus on the inversion of $Pd_{147}Pt_{162}$ DENs. The segregation energy for different sites on $Pd_{147}@Pt_{162}$ and Pd/Pt bulk are listed in 2.3. For $Pd_{147}@Pt_{162}$ in vacuum, the corner site has the most negative segregation energy (-0.26 eV), indicating that Pt atoms at corner sites are the least stable with respect to migration into the core. The presence of adsorbed OH groups does not significantly change the value of E_{seg} for the (100) facet, or the edge and corner sites. However, E_{seg} of atoms on the (111) facet, which is energetically unfavorable for swap- ping in the vacuum, drops to -0.27 eV in the presence of OH, becoming another reactive site for core-shell inversion.

Table 2.3: Summary of Segregation Energies of $Pd_{147}Pt_{162}$ Compared to Bulk Pd/Pt, with and without Surface Hydroxyl Present

	Pd_{147}@Pt_{162}				**Pd/Pt**	
site	(111)	(100)	edge	corner	(111)	(100)
E_{seg}	0.04	-0.17	-0.06	-0.26	0.03	-0.18
E_{seg}^{OH}	-0.27	-0.11	-0.05	-0.27	-0.28	-0.11

Previous studies showed that Pt can form a stable mono- layer on a bulk Pd surface and on large (∼3.5-9 nm) Pd nanoparticles[56, 41, 61, 58, 62, 70]. Accordingly, the same thermo-dynamic stability calculations used for the DENs, with and without surface OH groups, were performed on 4-layer, 4×4 Pd(111) and Pd(100) slab models supporting a Pt monolayer. The calculated segregation energies of both bulk facets are almost the same (within 0.01 eV, Table 2.3) as for the DEN model. This calculation indicates the inversion we observed on $Pd_{147}Pt_{162}$ is likely due to the unstable corner sites. Within the context of this model, as the size of the nanoparticle increases, the ratio of corner sites to surface sites drops, and the inversion will be less likely to occur. In addition, a Pt monolayer on larger Pd particles is likely kinetically stabilized. The nanoparticles in this study are only 2 nm in diameter and, hence, have a relatively flexible structure as compared to bulk materials, which is expected to lower the barrier for atom swapping especially at low coordinated sites.

2.6 Conclusion

Studies in this chapter represents good examples in which a well-defined structural deformation of a very small nanoparticle. results in a dramatic improvement in catalytic performance. The experimental findings correlate well with DFT calculations. Theory suggests that the increased disorder associated with <2 nm diameter nanoparticles, along with the relatively large number of edge and corner sites, drives the structural rearrangement. This type of rearrangement is not observed on larger nanoparticles or in bulk metals. The most significant outcome here, however, is that there appear to be major structural differences between particles in the 1∼2 nm size range of DENs, and the more commonly studied (and more experimentally tractable) nanoparticles having sizes >3 nm. This is likely due to the lower stability of the smaller particles, and thus their enhanced ability to deform in the presence of adsorbates and during catalysis. Deformation of very small nanoparticle may result in a dramatic improvement in catalytic performance.

Chapter 3

Random Alloy Nanoparticles for Catalysis

3.1 Abstract

Trends in the oxygen reduction activity of Pd/Cu bimetallic alloy nanoparticles are determined with calculations of oxygen binding to the particles for a range of Pd/Cu ratios. Thermodynamically, these nanoparticles favor random alloy structures. A reduction in the average oxygen binding is found as Cu is added to Pd, indicating an increase in catalytic activity up to a peak at a 1:1 Pd:Cu composition. Calculations show that Cu reduces the Pd-O binding energy and Pd increases the Cu-O binding energy. These changes are understood in terms of charge transfer from Cu to Pd, lowering the *d*-band center of Pd and raising that of Cu. The peak in activity occurs because these two effects not equivalent. A greater overlap between the *d*-states of Pd and the adsorbed oxygen as compared to Cu makes the reduction in binding at Pd more significant than the increase in binding at Cu. We present a simple model of the average binding energy which can generally predict activity trends in random alloys.

3.2 Introduction

Alloying is a strategy that has been used to find non-Pt electrocatalysts that are effective and less expensive for the oxygen reduction reaction (ORR)[76, 77, 25]. Mixing two or more metals can result in a catalyst that has distinct properties from its monometallic components. For example, it has been found that the addition of metals which bind oxygen strongly (Co, Ni and Cu, etc.) can lower oxygen binding to more noble metals (Pt or Pd) and improve their ORR catalytic activity[78, 79, 80, 81]. To aid the design of new alloy catalysts, calculations can be used to understand trends in activity and predict promising candidates for further investigation. The use of modern techniques to synthesize alloy nanoparticles with precise size and composition makes it easier to directly compare experiment with theory, and better understand the relationship between the structure of nanoparticles and their catalytic function[32].

The reduction of oxygen to water at a catalytic surface is a multistep reaction that includes at least two types of processes: O-O bond-breaking and the removal of the dissociation products by further reduction to H_2O. While the overall reaction is complicated, it has been found that some simple reactivity descriptors can be used to predict activity trends across different catalysts. In the case of the ORR, Bligaard *et al.* have shown through the use of micro-kinetic models that the binding of oxygen (or hydroxyl) is an effective indicator of activity[6]. A reason that this simplification works is that, for each elementary step in the reaction, there is a Brønsted-Evans-Polanyi (BEP) correlation between the transition state energy and the binding energy of the products[82, 83]. Trends in oxygen binding are thus correlated to trends in transition state energies for the dissociation of oxygen. In the weak binding regime, barriers are high and limit the overall kinetics. In the strong binding regime, the kinetics are limited by the removal of products from the catalysts. These two regimes can be seen in the so-called volcano plots where both weak and strong binding have low activity and the active catalysts, which provide a balance between these competing factors, are at the peak of the activity volcano. Using atomic oxygen binding as a reactivity descriptor for the ORR, a peak in activity is predicted at a binding strength slightly weaker than on the surface of bulk Pt[2].

In this work we investigate the effect of alloy composition in Pd/Cu nanoparticles on the ORR activity. Experimentally, Cu has been found to promote the activity of Pd at a ratio of 50%[84, 85]. This enhancement in activity is intriguing because the binding of oxygen to Pd is stronger than optimal and the binding to Cu is stronger than both Pt and Pd. In a previous study it was shown that Cu core-Pd shell particles have higher activity than monometallic Pd because subsurface Cu serves to weaken the binding of oxygen to the Pd surface, bringing it closer to the optimal[18]. The synergy between the two metals was understood in terms of an electronic interaction between subsurface Cu which lowered the *d*-band center of the surface Pd, and thus weakened the interaction with the oxygen adsorbate. In the case of random alloy particles, however, it is less clear how Cu could serve as a promoter, since

Cu on the surface of the particle will bind oxygen more strongly than Pd. In this study, we calculate the binding of oxygen to random Pd/Cu alloys at different compositions and show that there is in fact weaker binding in the alloy than in pure Pd or Cu particles, consistent with the experimental observations. An analysis of the *d*-band center shows that the change in binding for the two metals is not the same, and this difference gives rise to the enhanced activity of the random alloys.

3.3 Computation Models and Methods

Calculations of oxygen adsorption on Pd/Cu random alloy nanoparticles were done with density functional theory (DFT) implemented in the VASP code[63, 64]. The Kohn-Sham one-electron valence states were expanded in a basis of plane waves with a kinetic energy cutoff of 274 eV. The exchange-correlation energy was evaluated within the generalized gradient approximation with the PW91 functional[65]. Core electrons were described by pseudopotentials with the projector augmented-wave (PAW) method[66, 67]. Spin-polarization was tested and was used when necessary. A single Γ-point sampling of the Brillouin zone was used for the isolated particles. A vacuum gap of 8 Å separated the nanoparticles from their periodic images. All atoms in the nanoparticle were allowed to relax. Geometries were considered optimized when the force on each atom was less than 0.005 eV/Å.

Pd/Cu alloy nanoparticles were modeled as truncated octahedra containing 79 atoms. It is not known if this structure is the global minimum for each alloy particle, but it is the lowest energy structure that we found for a Pd nanoparticle of this size. As well as making the calculations simpler, keeping the same overall geometry allowed us to isolate the effects of varying the alloy composition. Random alloy particles with five different compositions were considered, varying in 25% increments. Particles with a 25%:75% ratio of component metals were considered in both random alloy and core-shell structures. A core-shell particle with 25% Cu, for example, has a core of 19 Cu atom and a shell of 60 Pd atoms and is denoted Cu@Pd. Random alloy geometries were constructed by randomly assigning each atom to the constituent metals, constrained to the specified overall composition. Ten configurations were generated for each random alloy composition. The binding of oxygen was calculated in the face centered cubic (FCC) hollow site in the center of each of the eight (111) facets, giving a total of 80 binding energies in each average. The logic for focusing on the (111) facets is that these sites provide the weakest binding and, therefore, the highest activity for metals which bind oxygen stronger than Pt. Corner and edge sites bind oxygen more strongly and are assumed to be less active or poisoned during the reaction. While there certainly could be a range in activities for sites with different binding energies, the average is the simplest measure which captures the trends in binding as a function of composition.

As part of our analysis to understand trends in binding energies, we use a Bader decomposition of the charge density into volumes around each atom[86, 87].

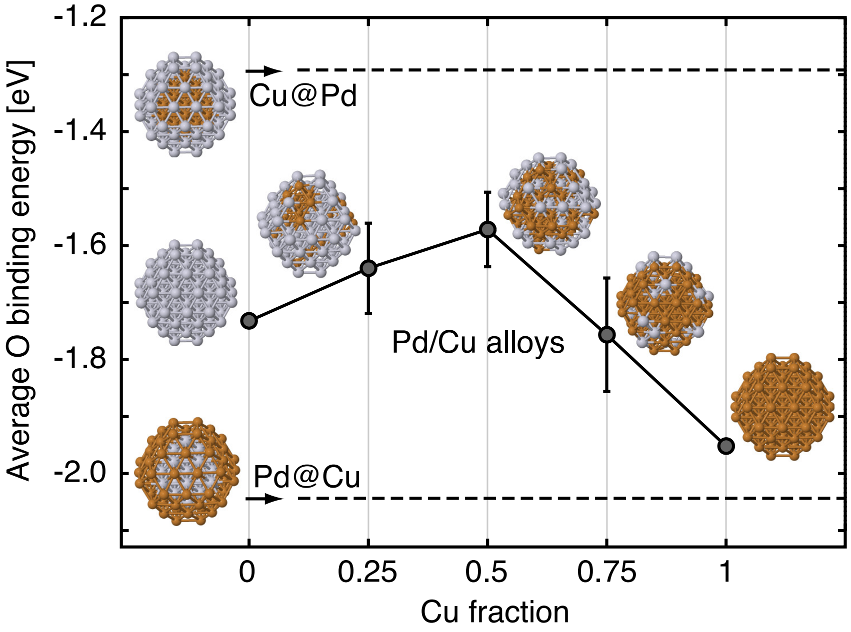

Figure 3.1: Average binding energy of oxygen on alloy Pd/Cu nanoparticles. Using this binding energy as a reactivity descriptor for the ORR indicates a peak in activity for random alloy particles at 1:1 compositions of Cu (dark color) and Pd (light color).

3.4 Catalytic Activity of Random Alloy Nanoparticles for Oxygen Reduction

3.4.1 Oxygen Binding to PdCu Alloy Particles

The average binding energy of atomic oxygen on Pd/Cu random alloy particles is shown in Figure 3.1. Since the binding of oxygen is an indicator of ORR activity, these data indicate that random alloy particles can have higher activity than those of pure Pd. The peak in activity is at a Pd:Cu ratio of 1:1, consistent with experiment[85, 84]. The error bars show the standard deviation of the distribution of binding energies in the average over

80 sites. While different local environments give rise to this distribution in binding energies, the trends over composition are significant. When the ratio of Cu is 75% and 100%, activity decreases to below that of Pd. The core-shell structures, Cu@Pd and Pd@Cu, fall beyond the extremes of the random alloy particles; Cu@Pd has the highest activity while Pd@Cu has the lowest. It is interesting that the trend in oxygen binding for the random alloy particles is not linear between Pd and Cu. Even though Cu itself has a strong affinity for atomic oxygen, it weakens the binding in alloy particles. To determine the reasons for the activity enhancement in random alloys, we have studied in more detail how the addition of Cu affects the average binding of oxygen in Pd particles.

3.4.2 *d*-band Model of Oxygen Binding

The origin of the average binding energy trends in the alloy nanoparticles can be understood by decomposing the interactions of oxygen with the individual metal types. Direct binding of oxygen to Cu is stronger than to Pd. Hollow sites with three Cu atoms bind oxygen the strongest, on average, and those with three Pd atoms, the weakest. Second neighbors also play a role; Cu atoms neighboring Pd decrease the Pd-O binding strength and Pd atoms neighboring Cu increase Cu-O binding. These effects, however, are not symmetric because the average binding does not vary linearly as a function of composition between monometallic Cu and Pd particles. Particles with a 50% Cu/Pd composition bind oxygen significantly weaker than would be expected from a linear interpolation, as shown in Figure 3.1. The use of a d-band model to separately model the Pd-O and Cu-O interactions can help explain how the composition changes the average oxygen binding energy.

Hammer and Nøskov proposed a model in which the interaction between a metal surface and an adsorbate can be described as the interaction between the metal d-band and the adsorbate s or p orbitals[14, 15, 88]. When the change of the metal-O interaction, $\delta E_{\mathrm{metal-O}}$, is dominated by a shift in the d-band center position, $\delta\epsilon_d$, a linear relationship arrises,

$$\begin{aligned} \delta E_{\mathrm{M-O}} &\simeq -4 f_d \frac{V_{\mathrm{M-O}}^2}{|\epsilon_d - \epsilon_{\mathrm{O}}|^2}\ \delta\epsilon_d \\ &= \alpha_{\mathrm{M-O}}\ \delta\epsilon_d \end{aligned} \tag{3.1}$$

where f_d is the local filling of the metal d-states, ϵ_{O} is the center of the oxygen $2p$ states, and V^2 is the coupling matrix element between the oxygen orbitals and metal d-states. To a good approximation, changes in these values in alloys are smaller than changes in ϵ_d so to first order in $\delta\epsilon_d$, the binding of oxygen, $E_{\mathrm{M-O}}$, varies linearly about ϵ_d[88, 17]. We label the proportionality constant $\alpha_{\mathrm{M-O}}$. In order to use this model to evaluate changes in oxygen binding due to alloying, we first need to quantify the change in the d-band level of surface atoms in the alloy particles. Figure. 3.2 shows how the average d-band level of surface atoms change with respect to the pure metal particles. The lowering of the Pd d-band and the raising of the Cu d-band can be understood in terms of charge redistribution in the alloy. In the 50:50 Cu:Pd alloy, a Bader analysis shows that 0.15 e is transferred from Cu to Pd. For Pd, the d-type density

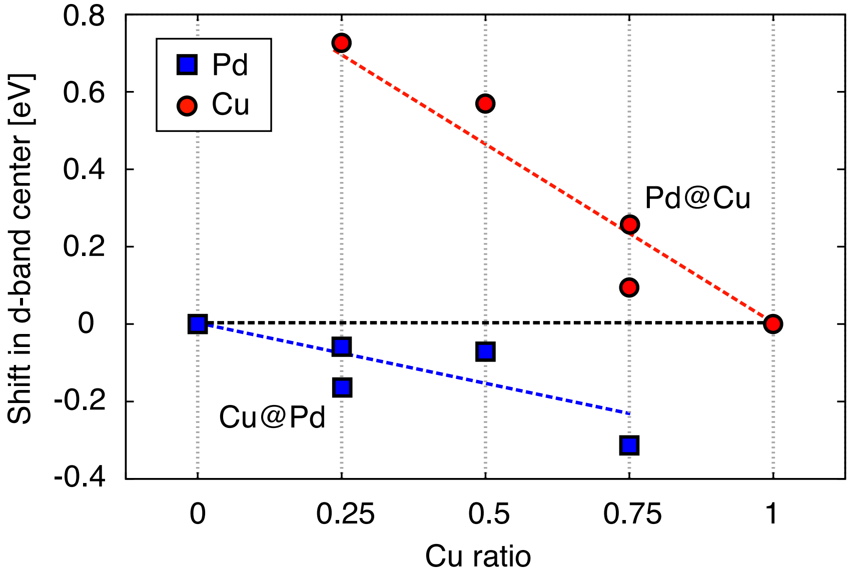

Figure 3.2: The *d*-band center shifts for Pd and Cu surface atoms in alloy particles with respect to the pure Pd and Cu particles, respectively. The *d*-band center of Pd is lowered by the addition of Cu, whereas the *d*-band center of Cu is raised by the addition of Pd.

of states at the Fermi level is 1.2 states/eV/atom so that the charge transfer lowers the *d*-band with respect to the (increased) Fermi level by 0.125 eV. This *d*-band shift is consistent with the data in Figure. 3.2.

To evaluate the effect of the *d*-band shifts on binding, we need to evaluate the constants $\alpha_{\mathrm{M-O}}$ (M = Pd, Cu) from Eq. 3.1. These constants can not be cleanly determined from the calculated energies of oxygen binding to the alloy particles, since the contributions from the two metal types are not separable. It is this interaction between the metals which we would like to understand in terms of the *d*-band model. Instead of using the random alloy geometries, we use core-shell structures to determine $\alpha_{\mathrm{M-O}}$, because there is a single metal type in the shell to which oxygen binds. Comparing a pure Pd particle to Cu@Pd shows a decrease in oxygen binding of 0.45 eV and a lowering of the surface Pd d-band by 0.17 eV, yielding a slope $\alpha_{\mathrm{Pd-O}}$ of -2.6. A fit of this correlation over a wider range of core metals gives a slope of -2.0[18]. Comparing Cu to Pd@Cu shows an increase in oxygen binding of 0.10 eV and an increase of the surface Cu d-band of 0.26 eV, giving a slope $\alpha_{\mathrm{Cu-O}}$ of -0.4.

The difference between $\alpha_{\mathrm{Pd-O}}$ and $\alpha_{\mathrm{Cu-O}}$ is central for understanding trends in oxygen binding to alloy particles. While the magnitudes of charge transfer between the metal types and shifts in d-band centers are comparable, the larger magnitude of $\alpha_{\mathrm{Pd-O}}$ as compared to $\alpha_{\mathrm{Cu-O}}$ means that the change in oxygen binding energy will be larger for Pd than for Cu. The difference in magnitude can be understood in terms of the larger coupling matrix element [$V^2_{\mathrm{M-O}}$ in Eq. 3.1] between the oxygen adsorbate states and the metal d states in Pd as compared to Cu. The value of V^2 is estimated to be 2.8 times larger for Pd as for Cu, primarily because Pd is a larger element with diffuse d electrons which overlap with the adsorbate states[15, 88]. Using our estimated values of $\alpha_{\mathrm{M-O}}$ and Eq. 3.1, we can linearly transform the d-band data in Figure 3.2 to the binding energy data shown in Figure 3.3. Since $\alpha_{\mathrm{Pd-O}} > \alpha_{\mathrm{Cu-O}}$, there is a much larger change in the binding to Pd then to Cu, as a result of alloying.

The linear relationship between the oxygen binding energy to the com-

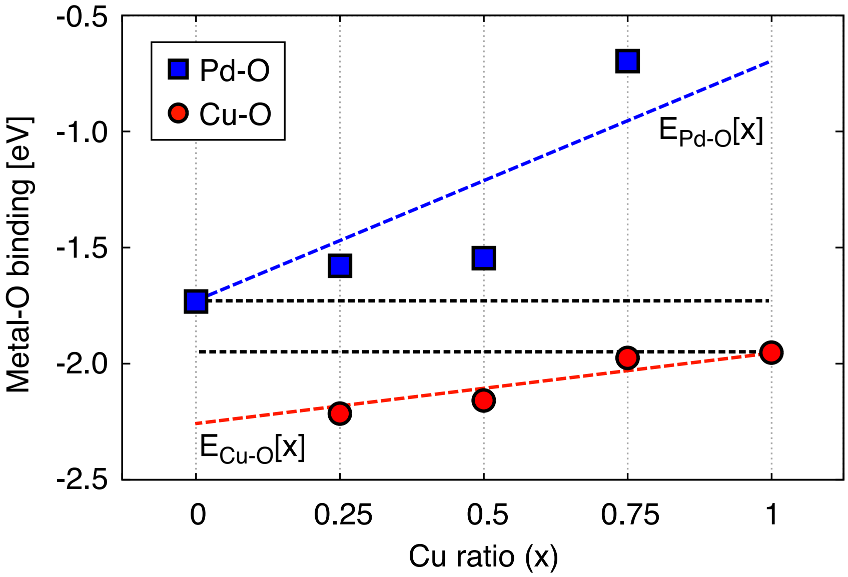

Figure 3.3: The Pd-O binding (blue squares) and the Cu-O binding (red circles) from Eq. 3.1 for alloy particles with different ratios of Cu. The (dashed) trend lines are calculated from the linear fits in Figure 3.2 and Eq. 3.1. The Cu-O binding changes by a small amount whereas the Pd-O binding is largely reduced by the addition of Cu.

ponent metals as a function of composition can be written as

$$E_{\mathrm{Pd-O}}[x] = E^0_{\mathrm{Pd-O}} + x\ m_{\mathrm{Pd-O}} \tag{3.2}$$

$$E_{\mathrm{Cu-O}}[x] = E^0_{\mathrm{Cu-O}} + (1-x)\ m_{\mathrm{Cu-O}}, \tag{3.3}$$

where x is the composition of Cu, $E^0_{\mathrm{M-O}}$ is the binding to a pure particle of metal M, and $m_{\mathrm{M-O}}$ (M=Pd,Cu) are the slopes of the trend lines in Figure 3.3. The average binding to an alloy particle can then be written as a linear combination of these two functions, weighted by the composition of the component metals,

$$E_b[x] = (1-x)\ E_{\mathrm{Pd-O}}[x] + x\ E_{\mathrm{Cu-O}}[x]. \tag{3.4}$$

Expanding this gives

$$E_b[x] = (1-x)\ E^0_{\mathrm{Pd-O}} + x\ E^0_{\mathrm{Cu-O}} \\ + (x - x^2)\ (m_{\mathrm{Pd-O}} + m_{\mathrm{Cu-O}}), \tag{3.5}$$

where the first two terms are the linear interpolation between the binding at the pure metal particles, and the final term is a quadratic function that describes the relative change in binding due the metals' influence on each other. The values of $m_{\mathrm{Pd-O}}$ and $m_{\mathrm{Cu-O}}$ are of opposite sign because charge is transferred from Cu to Pd, and the shift in d-band are in opposite directions. If the magnitude of $m_{\mathrm{Pd-O}}$ and $m_{\mathrm{Cu-O}}$ were the same, $E_b[x]$ would be a linear function; it is the difference in magnitude that gives rise to the non-linear function and the peak in activity for the alloy. The binding trend predicted by Eq. 3.4 fits the average binding energies calculated directly from DFT (see Figure 3.4). In the region of high Pd concentration oxygen binding is largely determined by the Pd-O interaction, which becomes weaker as the Cu ratio increases. At high Cu concentrations, the binding is dominated by the strong Cu-O interaction. The weakest binding occurs at an intermediate Cu ratio,

$$x^* = \frac{1}{2} - \frac{E^0_{\mathrm{Pd-O}} - E^0_{\mathrm{Cu-O}}}{2(m_{\mathrm{Pd-O}} + m_{\mathrm{Cu-O}})}. \tag{3.6}$$

is predicted by the model to be 40%, which is consistent to that found in our DFT binding calculations.

Activities of Pd/Cu random alloy particles are determined indirectly from the average binding energy of atomic oxygen on the (111) facets. Particles with 50% Cu are identified as the most active catalyst. The activity

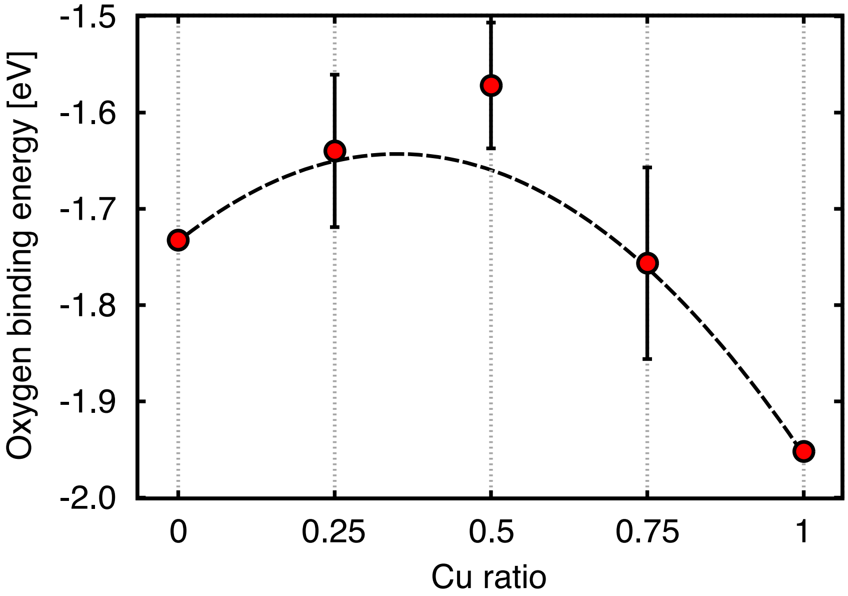

Figure 3.4: Comparison of the atomic oxygen binding energy calculated by DFT (red circle) and from Eq. 3.4 (dashed line).

enhancement is due to a difference in how the two metals respond to a shift in their d-band centers. A charge transfer from Cu to Pd raises the d-band of Cu and lowers that of Pd, resulting in a stronger oxygen binding to Cu and weaker to Pd. The change in Pd is much greater, however, due to stronger electronic coupling between Pd and the O adsorbate.

3.4.3 General Binding Trends of Random Alloy

We expect the above non-linear binding trend to be a general description of adsorbate binding to random alloys, providing a prescription for tuning catalytic activity through alloying. The curvature is determined by the sign and relative magnitude of $m_{\mathrm{M-O}}$, which can be roughly estimated from the O binding on core@shell nanoparticles. As shown in Figure 3.5, Pd/X (X=Au, Cu, Ir) random alloy NPs all exhibit non-linear O binding trend. O binding trend of Pd/Ir has the opposite curvature of Pd/Cu and Pd/Au. Let's take Pd/Au for example. Au has a lower Fermi level than Pd, charge transfer from Pd to Au when they are mixed. Table 3.1 shows that replacing the core of Pd@Pd to Au enhawnces the O binding while Pd@Au binds O more weakly than Au@Au, shows a negative $m_{\mathrm{Pd-O}}$ and a positive $m_{\mathrm{Au-O}}$. What's more, $|Eb_{\mathrm{Au@Pd}} - Eb_{\mathrm{Pd@Pd}}| < |Eb_{\mathrm{Pd@Au}} - Eb_{\mathrm{Au@Au}}|$ indicates that the magnitude of $m_{\mathrm{Au-O}}$ is larger than $m_{\mathrm{Pd-O}}$. Therefore, O binding trend of Pd/Au has a negative curvature for $-(m_{\mathrm{Pd-O}} + m_{\mathrm{Au-O}}) < 0$ in Figure 3.5. Similar discussion can also be applied to Pd/Cu and Pd/Ir system. In the Pd/Cu system, $m_{\mathrm{Pd-O}} > 0$, $m_{\mathrm{Cu-O}} < 0$ and $|m_{\mathrm{Cu-O}}| < |m_{\mathrm{Pd-O}}|$, the O binding trend shows a negative curvature. While, in Pd/Ir random alloy nanoparticles, $m_{\mathrm{Pd-O}} > 0$, $m_{\mathrm{Ir-O}} < 0$ and $|m_{\mathrm{Ir-O}}| > |m_{\mathrm{Pd-O}}|$ give raise to a positive curvature.

Table 3.1: Oxygen Binding Energy (eV) of Core-shell NPs for Pd/Au, Pd/Cu and Pd/Ir systems

Eb_{O}(eV)	Pd@Pd	X@Pd	X@X	Pd@X	X@Pd-Pd@Pd	Pd@X-X@X
Pd/Au	-1.73	-2.03	-0.60	0.05	-0.30	0.65
Pd/Cu	-1.73	-1.31	-1.95	-2.04	0.42	-0.09
Pd/Ir	-1.73	-1.56	-2.01	-2.33	0.17	-0.32

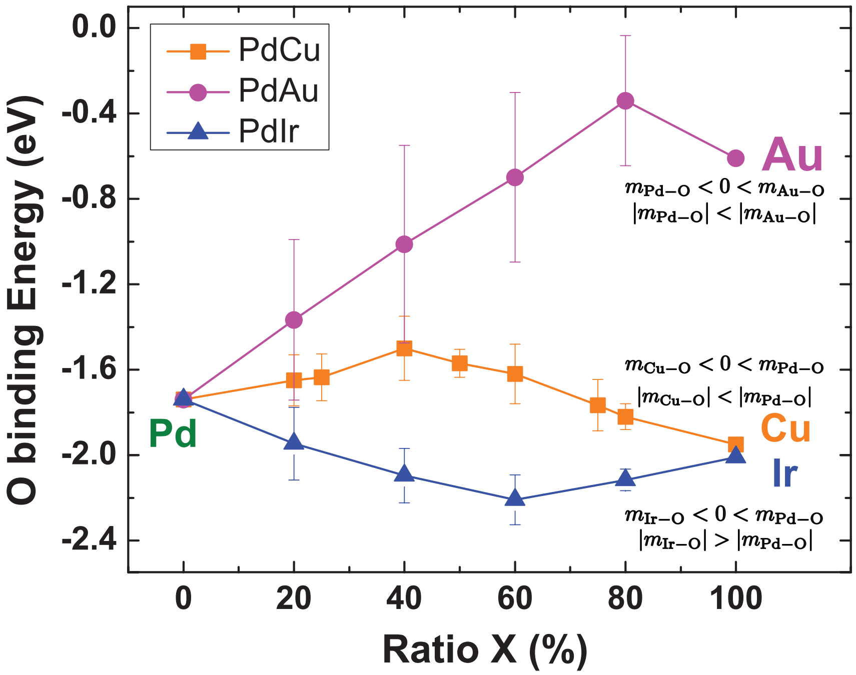

Figure 3.5: The average O binding energy trend of Pd/X (X=Au, Cu, Ir) random alloy.

Pd/Au has similar shape of nonlinear binding trend as Pd/Cu. The most significant difference between two system is the length of error bar, as shown in Figure 3.5. Pd/Au has much larger variation of O binding than Pd/Cu random alloy at all ratios. This difference in the binding distribution is not surprising given the factor that the difference of O affinity between Pd and Au is much larger than that between Pd and Cu.

3.4.4 Average Binding Energy *vs* Ensemble Effect

As shown by the error bar in Figure 3.5, such large disparity in the binding energy of Pd/Au random alloy raise an important concern that whether average binding energy is still a effective quantity to evaluate the catalytic function. Figure 3.6, shows the histogram of sited decomposed O binding energy for Pd/Au random alloy NP. Binding sites are classed to four possible combination of Pd and Au atoms in each three-fold hollow site (Pd_3, Pd_2Au_1, Pd_1Au_2, Au_3), showing in the insert of Figure 3.6. The O binding distribution of these four ensembles are quite separated from each other. The average binding energy of each Au ratio (green dash) is at somewhere few sites are distributed. In this kind of situation, average binding energy cannot reflect the catalytic function of the system. Thus different ensembles should be considered separately.

For instance, Figure 3.5 shows that the average binding energy of Pd/Au reaches a intersection with target O binding (-1.51eV) at around Au ratio=%20. However, the histogram in Figure 3.6 clarifies that all the four ensembles have no distribution at the target O binding energy. In other words, the performance of Pd/Au can hardly to be competitive as Pt.

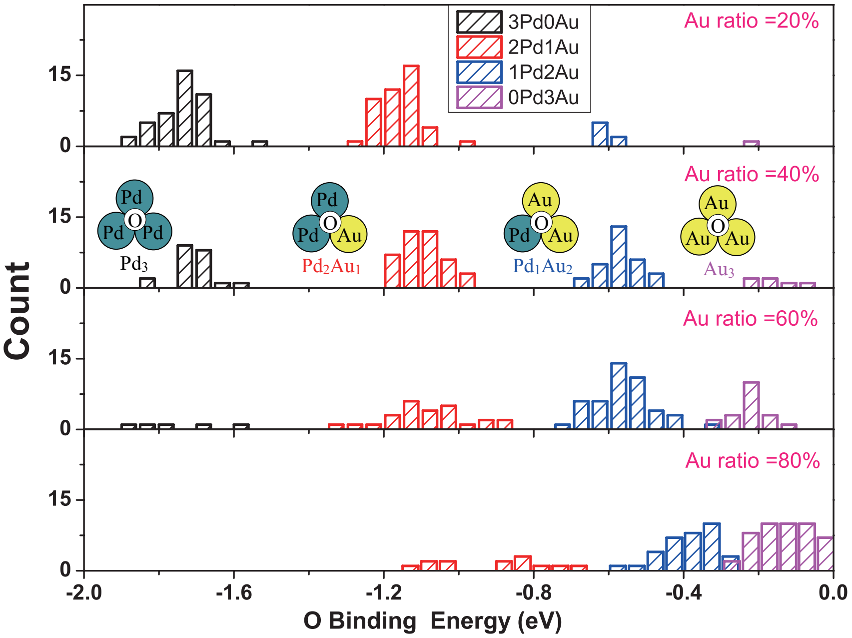

Figure 3.6: Histogram of ensemble decomposed O binding distribution of Pd/Au random alloy with %Pd=0.2, 0.4,0.6,0.8

Another example (Pd/Cu) where average binding energy is valid is also given here. As shown Figure 3.7, the binding distribution of the four ensembles overlaps closely with each other (scale is much smaller than Pd/Au). The average binding energies are at where most sites are distributed.

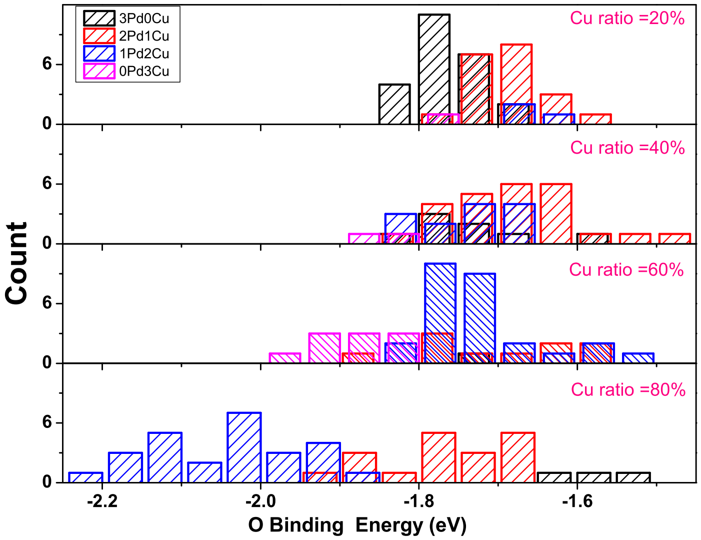

Figure 3.7: Histogram of ensemble decomposed O binding distribution of Pd/Cu random alloy with %Pd=0.2, 0.4,0.6,0.8

3.5 AgRh Alloy for Hydrogenation Reaction of Cyclohexene

3.5.1 Standard Free Energy Diagram of Cyclohexene Hydrogenation

Reaction mechanism of cyclohexene (CHE) hydrogenation is fundamental to understand the volcano-like activity trend of RhAu and RhAg alloy. Thus we have used density functional theorey (DFT) to study the hydrogenation reaction paths on a serial of close-packed fcc(111) transitional metal surfaces. The logic for focusing on (111) facet is that (111) has lower surface energy than the other low index surfaces for the elements of interest in this study[89]. Dispersion energy term was treated using the scheme of Tkatchenko and Scheffler[90]. The following elementary steps are considered:

$$\mathrm{CHE}(g) + * \rightarrow \mathrm{CHE}^* \tag{R1}$$

$$\mathrm{H}_2(g) + 2* \rightarrow 2\mathrm{H}^* \tag{R2}$$

$$\mathrm{CHE}^* + \mathrm{H}^* \rightarrow \mathrm{CHE}^* + * \tag{R3}$$

$$\mathrm{HCHE}^* + \mathrm{H}^* \rightarrow \mathrm{CHA}^* + * \tag{R4}$$

$$\mathrm{CHA}^* \rightarrow \mathrm{CHA}(g) + * \tag{R5}$$

where CHE, HCHE and CHA are short for cyclohexene (C_6H_{10}), first hydrogenated cyclohexene (C_6H_{11}) and cyclohexane (C_6H_{12}), respectively. * denotes for available binding sites on the surface. For each steps, the free energy change can be computed as:

$$\begin{aligned}
\Delta G_1 &= \Delta G_{\mathrm{CHE}} - \Delta G_* - \Delta G_{\mathrm{CHE}(g)} \\
&= E^{DFT}_{\mathrm{CHE}^*} - E^{DFT}_* - E^{DFT}_{\mathrm{CHE}(g)} - T\Delta S_1 \\
&= \Delta E_{\mathrm{CHE}^*} - T\Delta S_1 \\
\Delta G_2 &= 2\Delta E_{\mathrm{H}^*} - T\Delta S_2 \\
\Delta G_3 &= \Delta E_{\mathrm{HCHE}^*} - \Delta E_{\mathrm{CHE}^*} - \Delta E_{\mathrm{H}^*} - T\Delta S_3 \\
\Delta G_4 &= \Delta E_{\mathrm{CHA}^*} - \Delta E_{\mathrm{HCHE}^*} - \Delta E_{\mathrm{H}^*} - T\Delta S_4 \\
\Delta G_5 &= -\Delta E_{\mathrm{CHA}^*} - T\Delta S_5 + E^{DFT}_{\mathrm{CHA}(g)} - E^{DFT}_{\mathrm{CHE}(g)} - E^{DFT}_{\mathrm{H}_2(g)}
\end{aligned}$$

E_{X}^{DFT} is DFT calculated energy and ΔE_{X^*} is the binding energy of surface intermediates referenced to H_2(g) and CHE(g):

$$\begin{aligned}
\Delta E_{\mathrm{CHE}^*} &= E_{\mathrm{CHE}^*}^{DFT} - E_{*}^{DFT} - E_{\mathrm{CHE}(g)}^{DFT} \\
\Delta E_{\mathrm{H}^*} &= E_{\mathrm{H}^*}^{DFT} - E_{*}^{DFT} - 1/2 E_{\mathrm{H}_2(g)}^{DFT} \\
\Delta E_{\mathrm{HCHE}^*} &= E_{\mathrm{HCHE}^*}^{DFT} - E_{*}^{DFT} - E_{\mathrm{CHE}(g)}^{DFT} - 1/2 E_{\mathrm{H}_2(g)}^{DFT} \\
\Delta E_{\mathrm{CHA}^*} &= E_{\mathrm{CHA}^*}^{DFT} - E_{*}^{DFT} - E_{\mathrm{CHE}(g)}^{DFT} - E_{\mathrm{H}_2(g)}^{DFT}
\end{aligned}$$

Entropic corrections of gas phase CHA, CHE, and H_2 at standard condition (T=298.15K, P=1bar) are 0.98 eV, 0.90 eV and 0.40 eV, respectively. Figure 3.8 shows the free energy profile of the above reaction path on Ag, Au, Cu, Ir, Pd, Pt and Rh at standard condition (T=298.15K, P=1bar). Although barriers of each elementary step are not included, this level of thermodynamic analysis has been demonstrated in previous study for its capability to capture the primary activity trend[91, 2]. As shown in Figure 3.8, noble metals such as Ag and Au bind CHE and hydrogen too weakly so that the adsorption is endothermic. Rh on the other hand, binds them too strongly so that the hydrogenation and CHA release process and unfavorable in free energy.

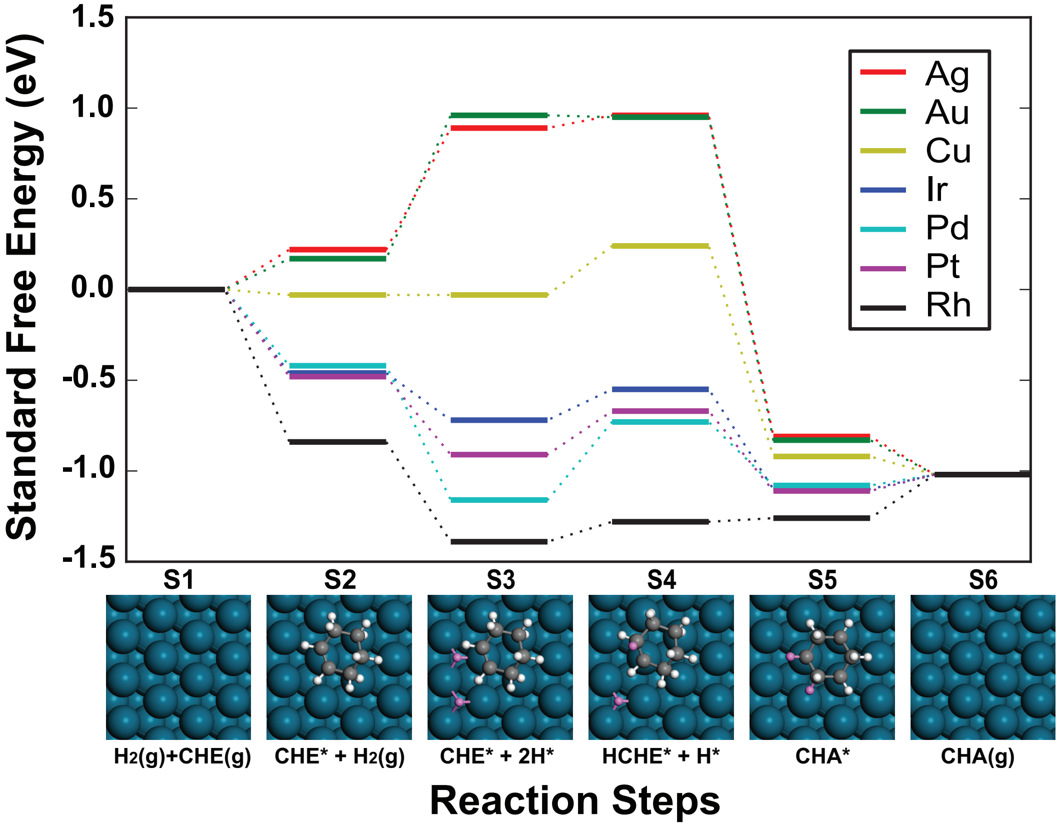

Figure 3.8: Standard free energy profile for CHE hydrogenation. Inserts schematically illustrate the surface intermediates at different reaction steps: blue spheres Metal, grey C, white H from CHE, pink H from H_2.

3.5.2 Activity Model of CHE Hydrogenation

The catalytic performance is estimated from the free energy that needs to be overcome along the reaction path, ΔG^{up}. Linear correlations between the binding energies of CHE, HCHE, and CHA (see Figure 3.9) allow for ΔG^{up} to be expressed simply in terms of the binding energies of H and CHE, as shown in Figure 3.10(a) . As can also be seen from the free energy diagram in

Figure 3.8, Ag/Au and Rh are located on opposite sides of the ΔG^{up} volcano. As indicated from the white dashed line in Figure 3.10(a), alloying Au and Ag to Rh weakens the binding of CHE and H, raising the free energy of S3-5 with respect to S6, and subsequently reducing ΔG^{up}. This picture validates the experimental observation of enhanced hydrogenation activity for the RhAu and RhAg alloy nanoparticles shown in Figure 3.10(b) . Another interesting finding from Figure 3.10(a) is that the binding of CHE and H are also correlated with each other, for the fcc(111) transition metal surfaces we investigated, which allows us to use the binding energy of hydrogen as a qualitative reactivity descriptor for the hydrogenation reaction in the following discussion.

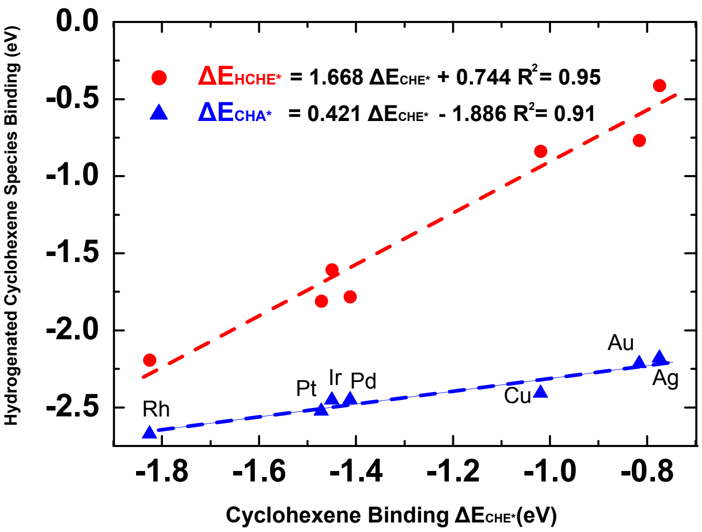

Figure 3.9: The Linear scaling relation between binding of CHE, HCHE and CHA on transition metal surface

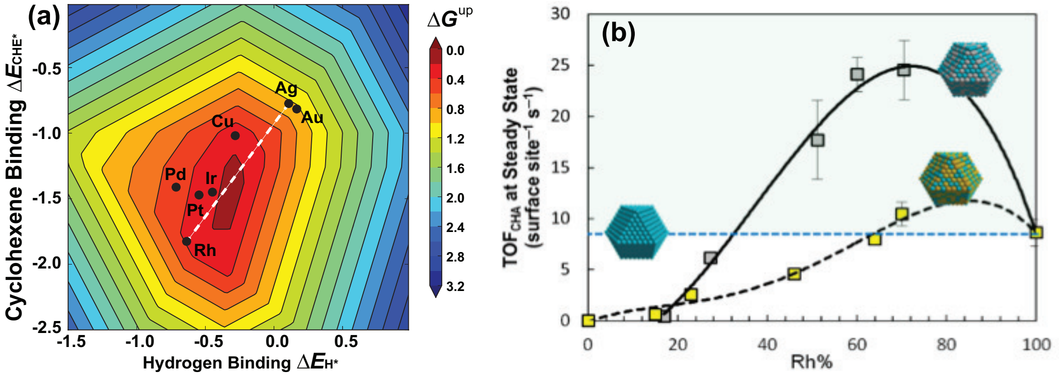

Figure 3.10: (a) Contour of ΔG^{up} as a function of binding energy of CHE and H. It can be minimized by alloying metals on different side of the volcano as shown in white dash line. (b) The steady-state rates of cyclohexene hydrogenation at 298.15K as a function of %Rh composition for the RhAg (grey) and RhAu (yellow) NPs versus pure Rh NPs (blue dashed line) prepared by microwave irradiation.

3.5.3 Hydrogenation Activity Trend of RhAg Alloy

From the above thermodynamic analysis, the peak of volcano is located near ΔE_{H^*} = -0.4 eV. Considering the large difference in reactants affinity between Ag/Au and Rh, it is important to decompose the hydrogen binding at different compositions into ensembles of binding sites[92, 93]. For clarity, we will focus our discussion on the RhAg system in the main text; the RhAu system (which can be found in the Supplementary Information) differs only in the quantitative values. Figure 3.11 shows that the average binding energy of H increases with Rh composition in the Ag/Rh alloy. For each intermediate alloy composition, the average binding energy (Figure 3.11; black line) is decomposed into individual histograms of binding sites. The target H binding ΔE_{H^*} = -0.4 eV is highlighted by the orange dashed line. Four sites can be distinguished from these data; these correspond to the four possible combinations of Ag and Rh atoms in each three-fold hollow site, where H atoms can be adsorbed (Rh_3, Rh_2Ag_1, Rh_1Ag_2, and Ag_3; Figure 3.11, inset). The large disparity in binding energies at these different sites indicates that they should be considered separately, rather than as part of an average. Interestingly, the H binding energy of the Rh_3 and Rh_2Ag_1 sites increases with increasing Ag content, as compared to the pure Rh particle (red and blue dashed line in Figure 3.11, in contrast to the solid black overall trend), indicating that H or CHE will over-bind and saturate these Rh-rich sites. The Ag_3 site binds H too weakly to adsorb reactants. The most active site, that is closest to the peak of the ΔG^{up} volcano, is the Rh_1Ag_2 site. As more Ag is alloyed to Rh, there is a higher ratio of Rh_1Ag_2 sites on the surface, until the surface is dominated by Ag_3 sites. On the other hand, we can also see that a higher Ag ratio increases the H binding of sites containing Rh, away from the target. The trade off between these two effects results in the volcano-like hydrogenation activity trend of RhAg alloy nanoparticles.

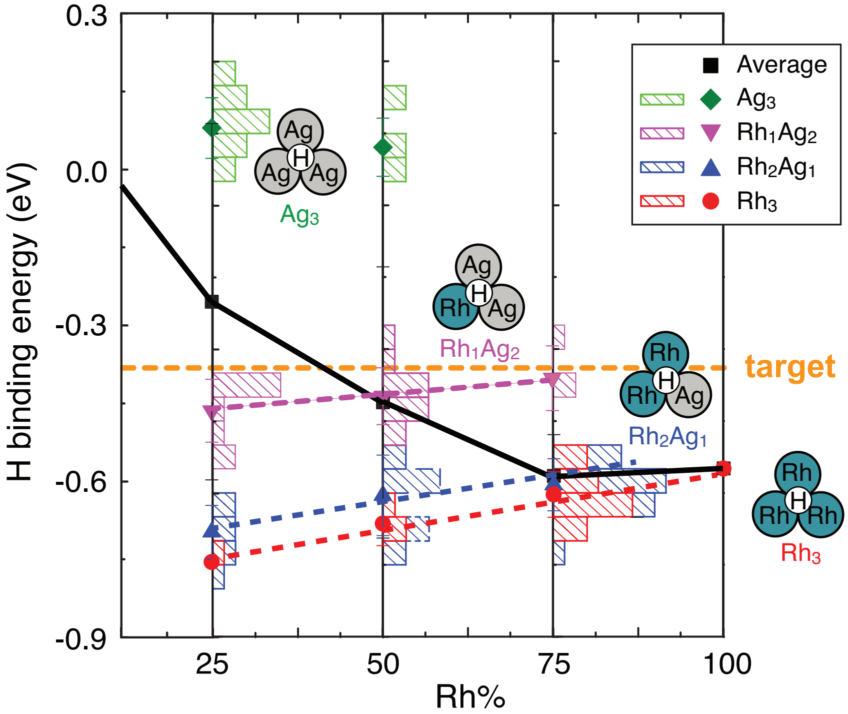

Figure 3.11: Decomposition of the average H binding energy into an ensemble of specific sites determined by the number of Ag vs Rh atoms at the binding site. The bars indicate the frequency of different binding energies at the three intermediate compositions, and the solid symbols indicate the average binding energy per site. Trends in the activity of the most active Rh-rich sites as a function of composition (red and blue dashed lines) are different from the overall trend (black solid line).Target H binding at about -0.4 eV is highlighted in orange dash line.

3.6 Conclusions

Activities of Pd/Cu random alloy particles are determined indirectly from the average binding energy of atomic oxygen on the (111) facets. Particles with 50% Cu are identified as the most active catalyst. The activity enhancement is due to a difference in how the two metals respond to a shift in their d-band centers. A charge transfer from Cu to Pd raises the d band of Cu and lowers that of Pd, resulting in a stronger oxygen binding to Cu and weaker oxygen binding to Pd. We show that this non-linear binding trend a general description of adsorbate binding to random alloys, providing a prescription for tuning catalytic activity through alloying. Additional cautiousness is need to for the binding distribution for the use of average binding energy to be valid. In the presence of large disparity, binding on individual ensemble should be investigated, rather than as a part of the average. Detailed examples are given as ORR on Pd/Au and hydrogenation reaction on Rh/Ag random alloy NP.

Chapter 4

Computational Design of Alloy-core@shell Nanoparticles for Catalysis

4.1 Abstract

The alloy-core@shell nanoparticle structure can combine the advantages of a robust noble metal shell and a tunable alloy-core composition. In this study we demonstrate a set of linear correlations between the binding of adsorbate to the shell and the alloy core composition, that are general across a range of nanoparticle compositions, size, and adsorbate molecules. This systematic tunability allows for a simple approach to design of this type of catalyst. Calculations of candidate structures for the hydrogen evolution reaction predict a high activity for the PtRu@Pd structure, in good agreement with what has been reported previously. Calculations of alloy-core@Pt 140-atoms nanoparticles reveal new candidate structures for CO oxidation at high temperature, including $Au_{0.65}Pd_{0.35}$@Pt and $Au_{0.73}Pt_{0.27}$@Pt, which are predicted to have reaction rates 200 times higher than Pt(111).

4.2 Introduction

As we discussed in the previous Chapter 2 and Chapter 3, Core@shell and random alloy are two bimetallic structures that have been studied in the search for Pt alternatives, largely because of their amenability to tune electrical properties by controlling the particle composition. Each structure, however, has its own shortcomings from the standpoint of design and synthesis. For core@shell nanoparticles, variations in composition are discrete in chemical compound space – elements can only be changed by integer atomic numbers – so that the catalytic properties can not be tuned continuously[18]. The properties of random alloys can be fine-tuned by varying the composition of the components[94], but there are limitations associated with having reactive metals on the particle surface since they can be oxidized and dissolve into solution.

A promising geometry for new nanoparticle catalysis has a homogeneous noble metal shell around a random alloy core of tunable composition. The noble shell stabilizes the particle surface for catalysis and the alloy-core composition allows for fine tuning of the catalytic properties[18, 94]. Alloy-core@shell nanoparticles can be synthesized by covering a random-alloy nanoparticle with the thin layer of the shell metal. There are two common synthetic technique for this. (1) Acid leaching of the non-noble component in the shell and thermal treatment to form a noble-metal skin. Examples of this include Pt_3M for M = Fe, Ni, Co. These bimetallic alloys covered with a Pt-skin, that were synthesized by Stamenkovic and co-workers, exhibited an improved oxygen reduction reaction (ORR) activity versus conventional Pt catalysts[95, 96, 97, 98]. (2) Under potential deposition (UPD) to form a homogenous monolayer shell on the core via careful potential control[29, 30, 99, 28]. Recent work in Adzic's group[100, 101] ,and ours[36], demonstrated successful synthesis of PdAu@Pt nanoparticles by Cu UPD on a PdAu core with subsequent galvanic exchange of the Cu with Pt.

In the past decade, much work has been done to reduce the number of parameters used to describe the activity of complex reactions. Nørskov *et al.* proposed a systematic method to construct the Sabatier rate as a function of one or two key reactants' binding energy using mean-field microkinetic models[6, 5, 7]. Building upon on the adsorption energy scaling[8, 9] and Brønsted-Evans-Polanyi (BEP) relationships[6, 102], this "Sabatier analysis method" significantly reduces the number of parameters and computational effort required for materials screening. Many studies over the past decade have shown that activity of catalytic reactions can be well described by the binding energies of key adsorbates on the catalyst. [10, 11, 12, 13] Given the correlation between binding energy and activity, we are able to optimize the compositions of alloy-core@shell nanoparticles for certain catalytic reaction. Specifically, oxygen reduction reaction (ORR) and hydrogen evolution reaction (HER) and CO oxidation (COox) are considered in this work to demonstrate how the alloy-core@shell structures can be tuned for catalysis.

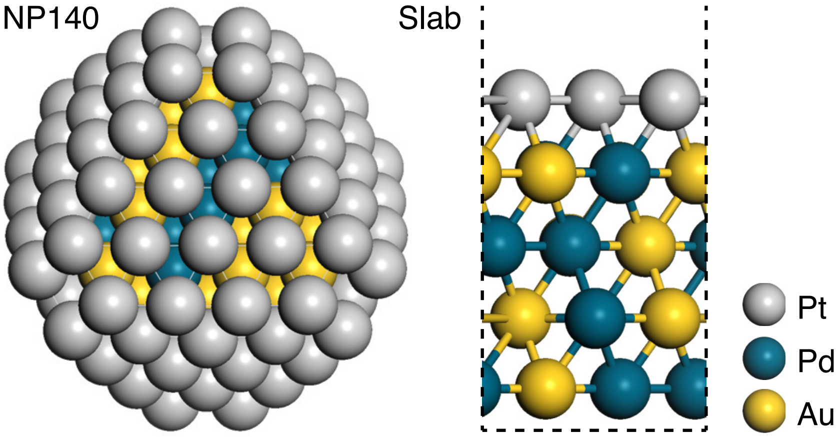

Figure 4.1: Structures of the alloy-core@shell NP140 and slab models.

4.3 Computational Models and Methods

In this study, adsorbate binding energies were calculated with density functional theory (DFT), as implemented in the Vienna Ab initio Simulation Package[63, 64]. Core electrons were described using the projector augmented wave method[66, 67]. Kohn-Sham single-electron wave functions were expanded in a plane wave basis with a kinetic energy cutoff of 300 eV to describe the valence electrons. The generalized gradient approximation using the revised Perdew-Burke-Ernzerhof functional [103] was chosen to evaluate the exchange-correlation energy. Spin-polarization was tested and was used when necessary. All atoms in the nanoparticle were allowed to relax; geometries were considered optimized when the force on each atom was less than 0.01 eV/Å. Two geometries were involved in this chapter, a nanoparticle containing 140 atoms, and a face centered cubic (FCC) single crystal (111) surface with a Pt monolayer skin covering a Pd/Au random alloy, as illustrated in Fig. 4.1. The nanoparticles were modeled as FCC crystallites in the shape of a truncated octahedron (denoted as NP140) with 44 core and 96 shell atoms. A cubic box of side length 26 Å was used to contain the particle with a vacuum gap of 11 Å in all directions to avoid interactions from periodic images. A Γ-point sampling of the Brillouin zone was used for the isolated particles. Convergence was checked by increasing the energy cutoff to 400 eV and the *k*-point mesh sampling to 2×2×2; the oxygen binding energy on a Pt 140-atom nanoparticle was found to change by only 1 meV ($< 0.1\%$). For each configuration, an adsorbate atom or molecule was bound to the center of each (111) facet, giving eight adsorbates in total. The binding energy Eb of adsorbate A was calculated by averaging over these eight sites as

$$Eb = \frac{1}{8}(E_{\mathrm{NP+8A}} - E_{\mathrm{NP}} - 8E_{\mathrm{A}}), \tag{4.1}$$

where $E_{\mathrm{NP+8A}}$ is the energy of the particle with eight bound adsorbates A, E_{NP} is the energy of the bare particle, and E_{A} is the reference energy of the adsorbate, A.

Single crystal surfaces were modeled with five-layer (3×3) slabs, to simulate the (111) facets of large nanoparticles[1, 104]. The bottom four layers consisted of a PdAu random alloy and the topmost layer contained monometallic Pt. A surface of this size and a vacuum gap of at least 12 Å between slabs was used to isolate the adsorbates from their periodic images. A (4×4×1) Monkhorst-Pack *k*-point mesh was used to sample the Brillouin zone. In all calculations, the bottom two layers of the slab were held frozen in their lattice positions. For each configuration, the binding energy of adsorbate A on the nine different FCC hollow sites are calculated as

$$Eb = E_{\mathrm{Slab+A}} - E_{\mathrm{Slab}} - E_{\mathrm{A}}. \tag{4.2}$$

4.4 O Binding on PdCu@Pd

4.4.1 Oxygen Binding Energy Trends

We first take $\mathrm{Cu}_x\mathrm{Pd}_{1-x}$@Pd NP140 as a case study. The two extremes of $\mathrm{Cu}_x\mathrm{Pd}_{1-x}$@Pd ($x = 0$ and 1) are pure Pd and Cu@Pd particles, which are on opposite sides of the peak in the volcano plot. Both are expected to have lower activity as compared to Pt(111); the Pd particle binds O too strongly, whereas Cu@Pd binds O too weakly. When the composition of the core is varied, however, we have an opportunity to find an optimal alloy-core@shell structure that has the target O binding.

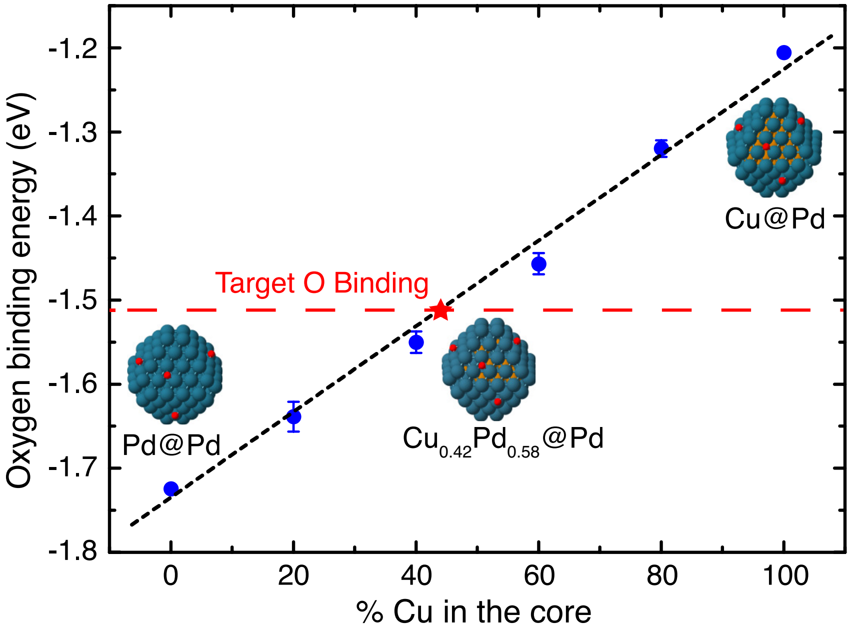

Figure 4.2: Average binding energy of oxygen to the Pd(111) facets of Pd/Cu alloy-core@Pd shell nanoparticles. The inset figures show the Pd (blue) shelled nanoparticles with varying Cu (orange) composition in the core, as well as the oxygen (red) binding sites.

Figure 4.2 shows the average binding energy of atomic oxygen on $\mathrm{Cu}_x\mathrm{Pd}_{1-x}$@Pd NP140. A near-linear relationship between the average atomic O binding energy and Cu ratio in the alloy core is shown in the figure. The red dashed line marks the O binding energy on Pt(111), which is the target O binding. Each O binding energy data point is averaged over ten different configurations with the specified core composition. The standard deviation of the O binding distribution is indicated by the error-bars. Using the O binding energy as a descriptor for ORR activity and O binding on Pt(111) as the target, we are able to predict a volcano-shaped relationship between ORR activity and the

Cu ratio in the alloy core with its peak at 42% Cu in the alloy core. Since there are 44 atoms in the core of a 140-atom particle, we predict that $Cu_{18}Pd_{26}$@Pd should give the best catalytic activity for the ORR.

Compared with a previous study of Pd/Cu random alloy nanoparticles, Cu_xPd_{1-x}@Pd NP140 have two distinct features in the trend of O binding energy as a function of composition[94]. First, unlike the quadratic relationship between O binding energy and Cu composition calculated for Pd/Cu random alloys, the relationship for Cu_xPd_{1-x}@Pd NP140 is linear. Second, the distribution of O binding energies on Cu_xPd_{1-x}@Pd is much narrower than for Pd/Cu random alloys. These two distinctions arise from the homogeneity of the shell composition. In Pd/Cu random alloys, the average O binding energy varies linearly with the binding energy to the component metals, and the significance of these contributions to the average vary linearly with composition. The product of these two factors leads to the quadratic O binding trend with alloy composition. In the Pd shell particles, there is no variation in the species to which O binds, it is always Pd, and so the O binding trend is linear in composition. Similarly, the distribution of O binding energy is large in the Pd/Cu random alloy particles where O binds to FCC sites on the (111) facets, which have four distinct compositions (Pd_3, Pd_2Cu_1, Pd_1Cu_2, and Cu_3). In Cu_xPd_{1-x}@Pd NP140, the FCC sites always consist of three Pd atoms, which reduces the width of the O binding energy distribution.

4.4.2 *d*-band Model

The *d*-band model proposed by Hammer and Nørskov has been widely used to understand trends in chemisorption of adsorbates on transition-metal surface[14, 15, 16]. In this model, interaction between the metal surface and the adsorbate molecule is described as a function of the *d*-band of the metal. When a shift in *d*-band center of metal surface is the dominant factor determining chemisorption strength, a differential change in chemisorption energy is linearly correlated to the shift in the position of *d*-band center[16, 17]. In the case of Pd-O interaction, this linear relationship can be expressed as

$$\delta E_{\mathrm{Pd-O}} \simeq -4 f_d \frac{V^2}{|\epsilon_d - \epsilon_{\mathrm{O}}|^2}\, \delta\epsilon_d \tag{4.3}$$

where f_d is the local filling of the Pd *d*-states, ϵ_{O} is the center of the oxygen $2p$ states, and V is the coupling matrix element between the oxygen $2p$ orbitals and Pd *d*-states. When comparing similar binding geometries, changes in f_d and V can be small as compared to the *d*-band center shift so that in a small range of ϵ_d, the slope $\delta E_{\mathrm{Pd-O}}/\delta\epsilon_d$ can be approximated as a constant.

Figure 4.3 shows the linear relationship between the average *d*-band center of Pd atoms on (111) facets and the Cu ratio in the nanoparticle core. Increasing the Cu ratio in the alloy core lowers the *d*-band center of the shell. As the *d*-band center is lowered from the Fermi-level (E_F), there is less overlap between the *d*-states of the surface Pd atoms and the $2p$ states of the adsorbed O, resulting in weaker O binding. Thus the linear O binding trend calculated with DFT can be explained by the linear shift in the *d*-band center with Cu concentration in the core.

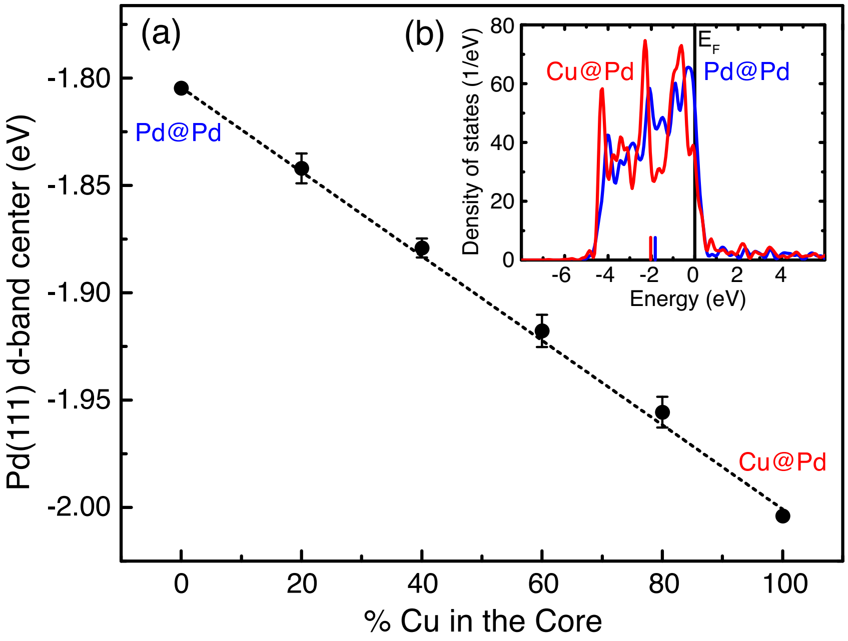

Figure 4.3: (a) The average d-band center of Pd atoms on the (111) facets is lowered by the addition of Cu in the core, which in turn weakens the O binding energy. (b) The d-band density of states for Pd (111) atoms in the two extremes: Pd@Pd (blue) and Cu@Pd (red). The small vertical marks above the x-axis indicate the center of the d-bands. The Cu core lowers the d-band of the Pd shell as compared to the Pd core.

To better understand the relationship between the d-band center and core composition, it is helpful to determine the factors which affect the d-band center. In the discussion by Tang *et al.* on core-shell nanoparticles[18] , it was found that changes of d-band filling and d-band width are two important factors that shift the d-band center. Change of the d-band filling is mainly due to charge redistribution between the Pd surface atoms and the alloy core; change of the d-band width is attributed to bond-length variation in the surface (the strain effect) and electronic overlap with subsurface alloy atoms (the ligand effect). Using the approach of Tang *et al.*, we were able to determine by how much the d-band center shift is caused by charge redistribution and how much by the widening of the surface d-band.

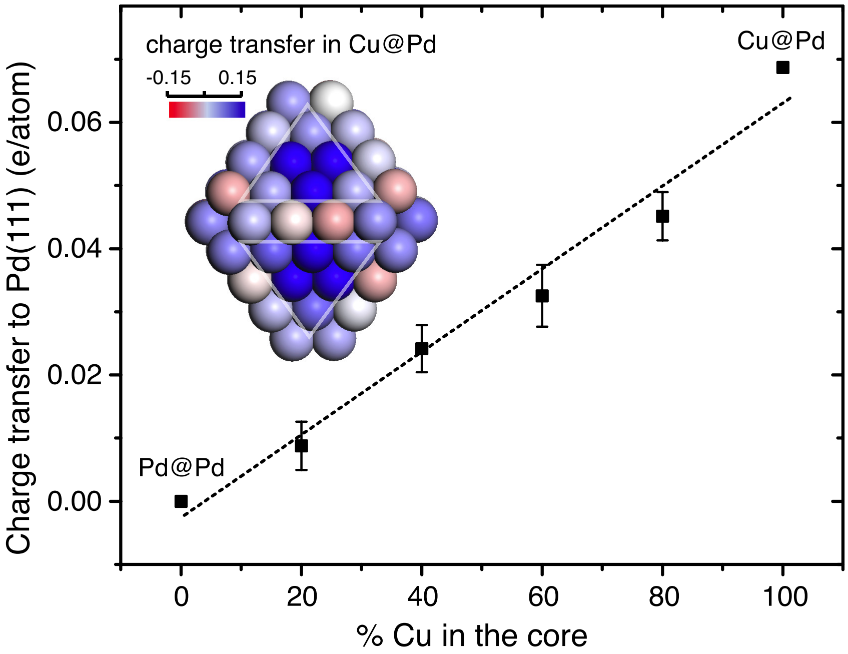

Figure 4.4: Average net charge on Pd (111) facet atoms (indicated by triangles in the inset figure) in alloy core nanoparticles as compared to monometallic Pd particles as a function of the Cu ratio in the core. The inset shows the Bader charge redistribution on the Pd shell atoms due to the change of core metal from Pd to Cu.

Figure 4.4 shows the amount of charge transferred to Pd atoms on (111) facets with respect to the pure Pd@Pd nanoparticle. The charge was calculated as an integration of valence charge within Bader volumes surrounding each Pd atom. As shown in Fig. 4.4, the net charge on the surface Pd atoms is proportional to the ratio of Cu in the alloy core. Because Cu has a higher Fermi energy than Pd[105], charge flows from Cu to Pd, when Cu is alloyed in the core of the nanoparticles. Since the number of Pd shell atoms is fixed at 96, more Cu in the alloy core results in more net charge distributed on the Pd atoms. The transferred charge from Cu to Pd then increases the filling of of the Pd *d*-band and lowers the *d*-band center respect to the Fermi level. This lowering of *d*-band can be estimated by dividing the DOS at the Fermi level into the amount of charge transferred. The DOS of the Pd (111) surface atoms at the Fermi level is 52 states/eV for Pd@Pd, and 35 states/eV for Cu@Pd. Considering that the total number of Pd (111) facet atoms is 48, the average Pd DOS at the Fermi level is 43 states/eV or 0.89 states/eV/atom. As shown in Fig. 4.4, comparing Pd@Pd to Cu@Pd, 0.07 e/atom of charge flows from Cu in the subsurface to Pd in the shell. Using the above values, the effect of charge transfer is estimated to lower the *d*-band center by 0.08 eV.

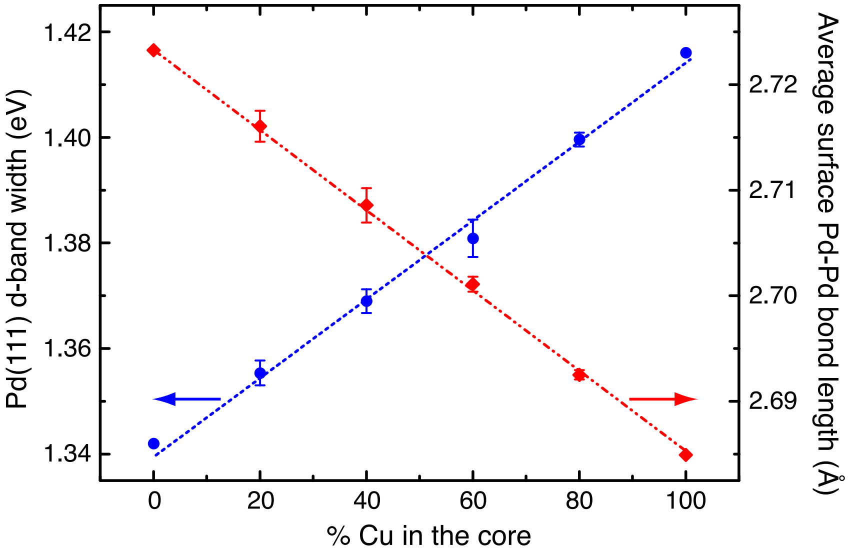

Figure 4.5: Trends of average *d*-band width (blue) and average Pd-Pd bond length (red) of Pd (111) facet atoms as a function of the ratio of Cu in the alloy core

Figure 4.5 shows a linear increase of the *d*-band width with the ratio of Cu in the alloy core. Since Cu has a smaller lattice constant than Pd, alloying Cu into the core shrinks the size of the nanoparticle, causing a shorter Pd-Pd bond length in the Pd shell. The average Pd-Pd bond length between Pd atoms on the (111) facets decreases linearly with the ratio of Cu in the alloy core, from 2.725 to 2.685 Å. The compression of the Pd-Pd bond enhances the overlap between states and widens the *d*-band. The effect of *d*-band widening on the shift of the *d*-band center can be estimated in a rectangular model of the *d*-band[19]. The correlation between this two *d*-band character parameters is given by

$$\delta\epsilon_d = \sqrt{12}(0.5 - f_d)\delta w \tag{4.4}$$

where δw is the change of *d*-band width, $\delta\epsilon_d$ is the corresponding shift of *d*-band center, and f_d is the filling of Pd *d*-band. As shown in Fig. 4.5, the *d*-band width increases by 0.08 eV with the replacement of Pd for Cu in the core. The average filling of the Pd NP140 *d*-band is 0.91. Using Eq. 4.4, the lowering of the *d*-band center due to band widening is estimated to be 0.11 eV.

From the above analysis, replacing Cu in the core of a Pd particle linearly increases the Pd shell *d*-band filling and the Pd *d*-band width. These two effects are estimated to lower the *d*-band center of Pd (111) facet atoms by 0.08 and 0.11 eV respectively. The total estimated *d*-band shift from these two factors is in excellent agreement with what is calculated explicitly (0.2 eV). Our results are consistent with the finding of Tang *et al.* on core-shell nanoparticles; charge transfer can be an important factor for tuning the *d*-band structure of small nanoparticles.

4.5 Universality of Linear Binding Correlation of Alloy-core@shell NP

In this section, we will show that the linear binding trend is a general picture of the adsorbate binding to alloy-core@shell nanoparticles, which can be applied to design new catalysts for various catalytic reactions on nanoparticles. We expect this trend to be independent of types of alloy-core elements, shell element, adsorbates, particles size.

4.5.1 Oxygen Binding to Other M_xPd_{1-x}@Pd NP140

O binding trends of other M_xPd_{1-x}@Pd NP140 were studied to examine the universality of the linear relation between O binding energy trend and core component ratio. Since Pd@Pd binds O stronger than the target Pt(111) slab, we selected metals M for which M-core@Pd-shell particles bind O weaker than the target, in order to tune the O binding of the Pd-shell particles towards the target value. The choice of such metals to mix with Pd in the core can be Ir, Rh, Cu, Ru or Mo. Figure 4.6 shows that each O binding energy trend is linear with the ratio of the alloying metal M in the core. Furthermore, in the case study of Cu_xPd_{1-x}@Pd NP140, the electronic structure (e.g. *d*-band center) of the Pd shell was also observed to vary linearly with the alloy-core composition.

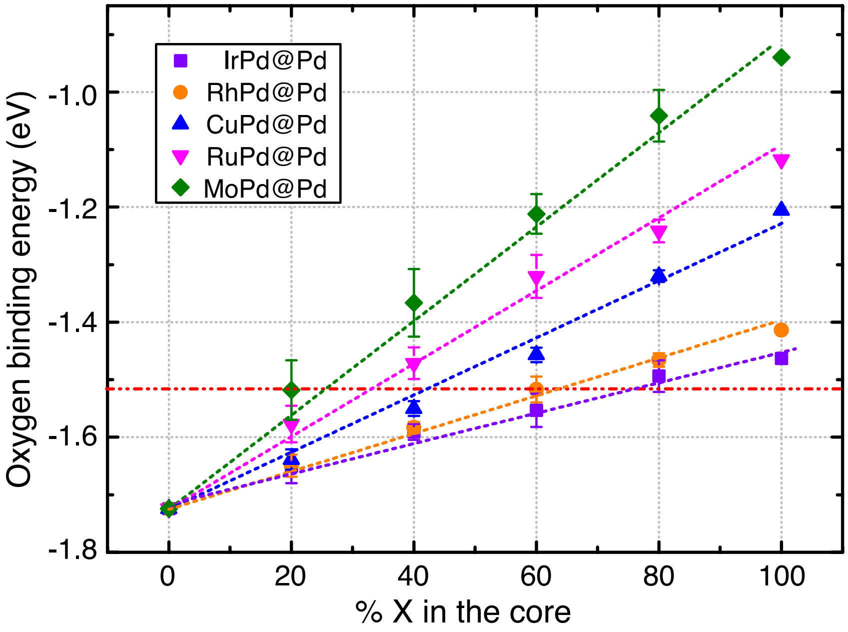

Figure 4.6: O binding to various M_xPd_{1-x}@Pd NP140 (M=Ir, Rh, Cu, Ru and Mo)

4.5.2 Oxygen Binding to X_xY_{1-x}@Pt NP140

Following the above discussion on Pd-shelled particles, the core metals can be classified into two groups: Pd, Cu, Ir, Ru, and Rh reduce the O binding to the Pt shell when they are added into the core, while Au and Ag increase the O binding energy. The target O binding can be achieved by alloying metal X from the first group (X = Pd, Cu, Ir, Rh, and Rh) and metal Y from the second group (Y = Au and Ag) in the core. Figure 4.7 shows the average O binding energies of (a) X_xAu_{1-x}@Pt and (b) X_xAg_{1-x}@Pt as a function of core composition.

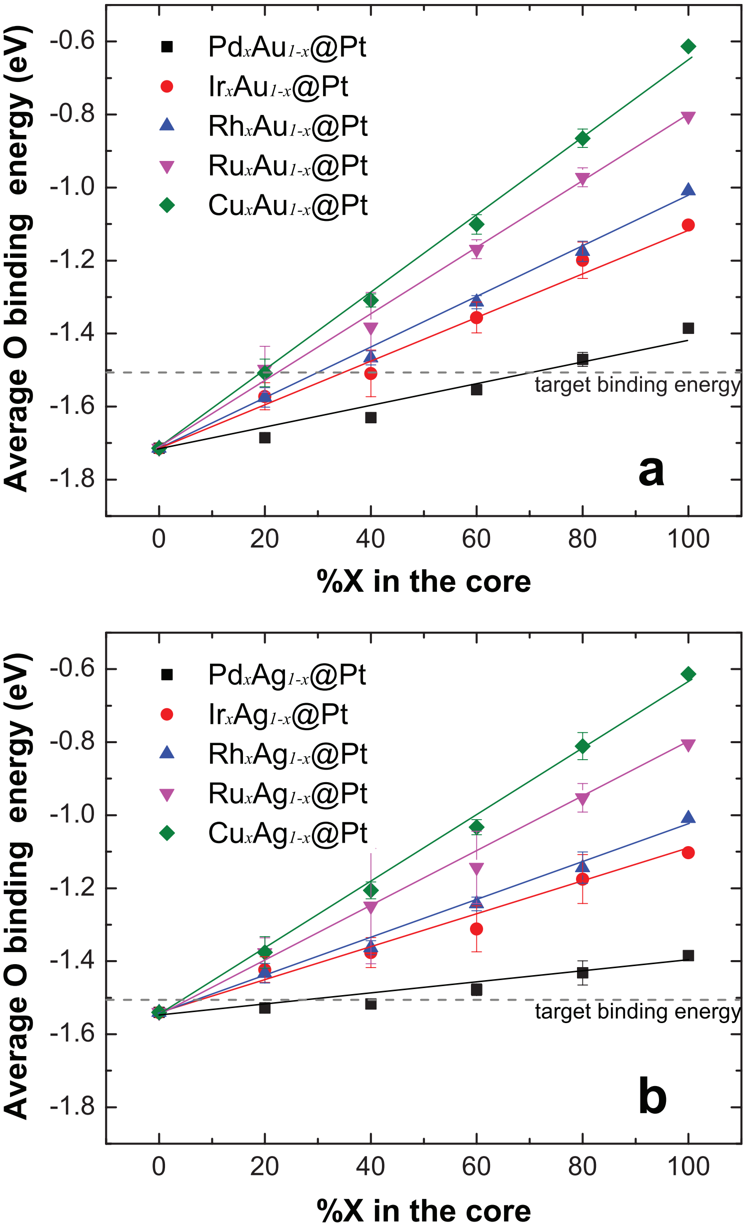

Figure 4.7: Oxygen binding energy trends for (a) X_xAu_{1-x}@Pt and (b) X_xAg_{1-x}@Pt NP140 (X = Pd, Ir, Rh, Ru, and Cu). The gray dashed line represents the target oxygen binding energy.

4.5.3 Variation of Adsorbates and Particle Size

Trends in the binding energy of the seven adsorbates (A = O, C, H, N, S, CO, NO) were calculated as a function of composition in a Pd/Au subsurface alloy, covered with a monolayer of Pt: the NP140 and slab models. Binding of adsorbates were studied on the FCC-hollow sites of the (111) facet, while CO was bound to on-top sites. CO adsorption energies are corrected based on the CO stretch frequency as proposed by Mason[106].

Reference energy of all adsorbates E_{A} (A=O, C, H, N, S, CO, NO) in equations are calculated as follow:

$$\begin{aligned} E_{\mathrm{CO}} &= E^{m}_{\mathrm{CO}} \\ E_{\mathrm{NO}} &= E^{m}_{\mathrm{NO}} \\ E_{\mathrm{H}} &= \frac{1}{2}E^{m}_{\mathrm{H_2}} \\ E_{\mathrm{N}} &= \frac{1}{2}E^{m}_{\mathrm{N_2}} \\ E_{\mathrm{O}} &= E^{m}_{\mathrm{H_2O}} - E^{m}_{\mathrm{H_2}} \\ E_{\mathrm{S}} &= E^{m}_{\mathrm{H_2S}} - E^{m}_{\mathrm{H_2}} \\ E_{\mathrm{C}} &= E^{m}_{\mathrm{CH_4}} - 2E^{m}_{\mathrm{H_2}} \end{aligned}$$

, where E^m is the calculated DFT energy of the molecule in the gas phase. O binding energies are referenced to O_2 gas phase molecule in other places of this dissertation. Ten different random-alloy configurations were generated to calculate the average binding energy for each core composition, giving a total of 80 binding sites for the nanoparticle and 90 sites for the slab model, contributing to the average. Although the number of random configurations we considered is less than the total possible number, our sampling provides a sufficient estimation for capturing trends in binding energies.

As demonstrated by Nørskov *et al.*, there is a good scaling relationship between a single atomic adsorbate and its hydrides with the same binding geometry, e.g. O vs OH, C vs CH_n, and N vs NH_n[8, 9]. Accordingly, the seven adsorbates were chosen to cover most of the key reactant motifs of interest for heterogeneous catalysis related to energy. Figure 4.8 shows the average binding energy of the adsorbates on the Pd_xAu_{1-x}@Pt NP140 and slab geometries (refer to large size NP) with Pd ratios x = 0, 0.25, 0.5, 0.75 and 1.0, in the random alloy core. The standard deviation of the binding energy distribution is indicated by the error bars. The linear relationship between the binding energy and core-composition is a result of the linear response of shell *d*-band center shift to the variation of the alloy-core composition. Figure 4.9 shows that the average *d*-band center of PdAu@Pt NP140 also varies linearly with the alloy-core composition.

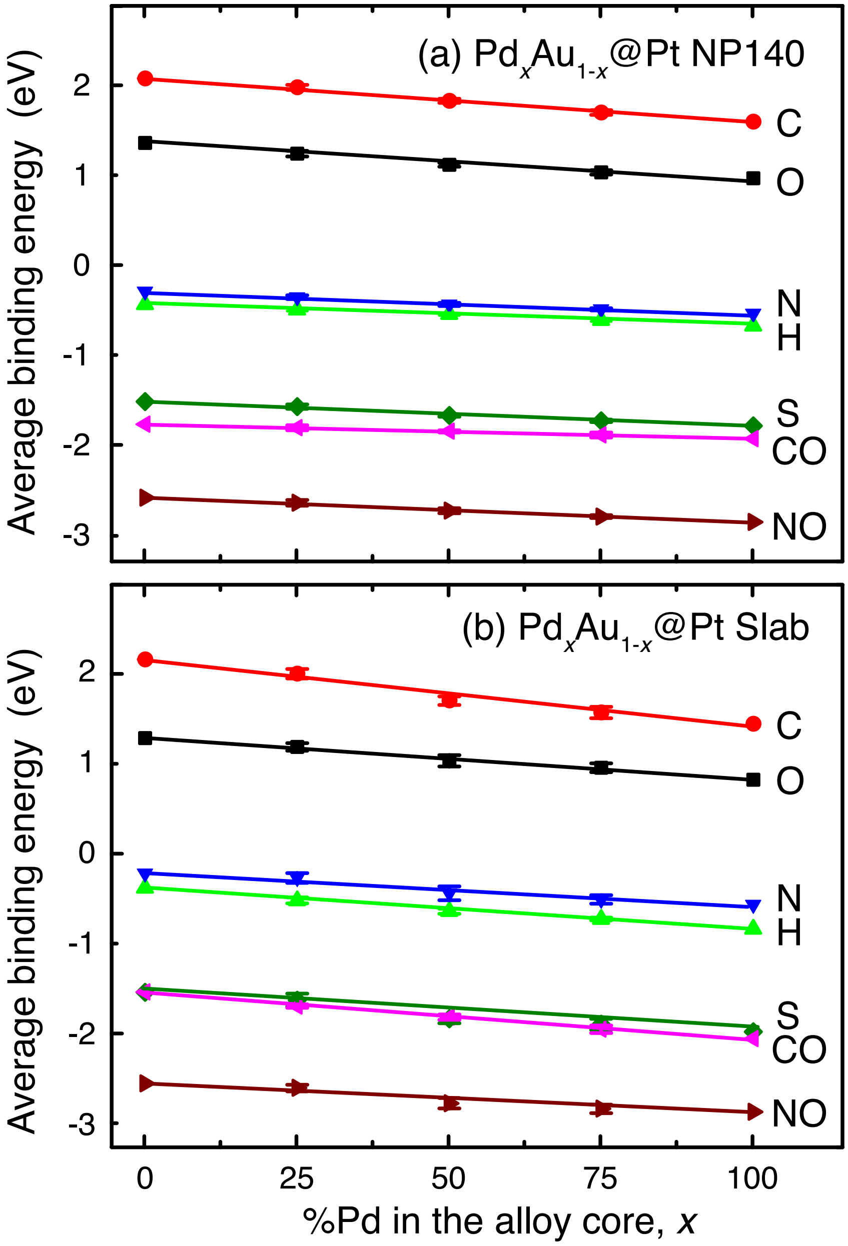

Figure 4.8: Average binding energy of seven adsorbates to the Pt(111) facets of Pd_xAu_{1-x}@Pt (a) NP140 and (b) slab geometries as a function of the Pd ratio in the alloy core, x.

Similar linear correlation trends between the core composition and the *d*-band center of the shell was observed previously for the PdCu@Pd system[107]. In that work, it was shown that strain and charge redistribution are two major factors affecting the *d*-band of the nanoparticle shell. In the PdCu@Pd system, the two effects had a similar influence on the *d*-band center, but in general their relative weight will depend upon the specific metals. In the PdAu@Pt system, for example, the *d*-band center shift is dominated by strain effect; while charge redistribution is much more important in PdIr@Pt system, where the variation in Pt-Pt bond lengths is much smaller. Details of these extreme examples are given in Figure 4.10.

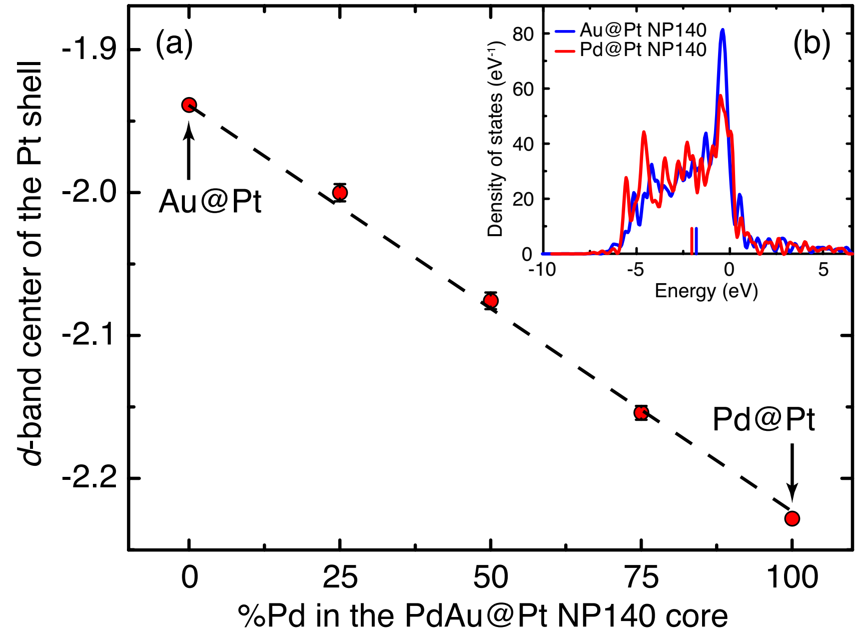

Figure 4.9: (a) Average d-band center (red circles) of the Pt shell varies linearly with the fraction of Pd in the alloy-core, x, in $\mathrm{Pd}_x\mathrm{Au}_{1-x}$@Pt NP140. (b) d-band density of states for the Pt shell at the two endpoint structures: Au@Pt (blue) and Pd@Pt (red) NP140. The small vertical marks above the x-axis indicate the center of the d-bands. The Pd core lowers the d-band of the Pt shell as compared with the Au core.

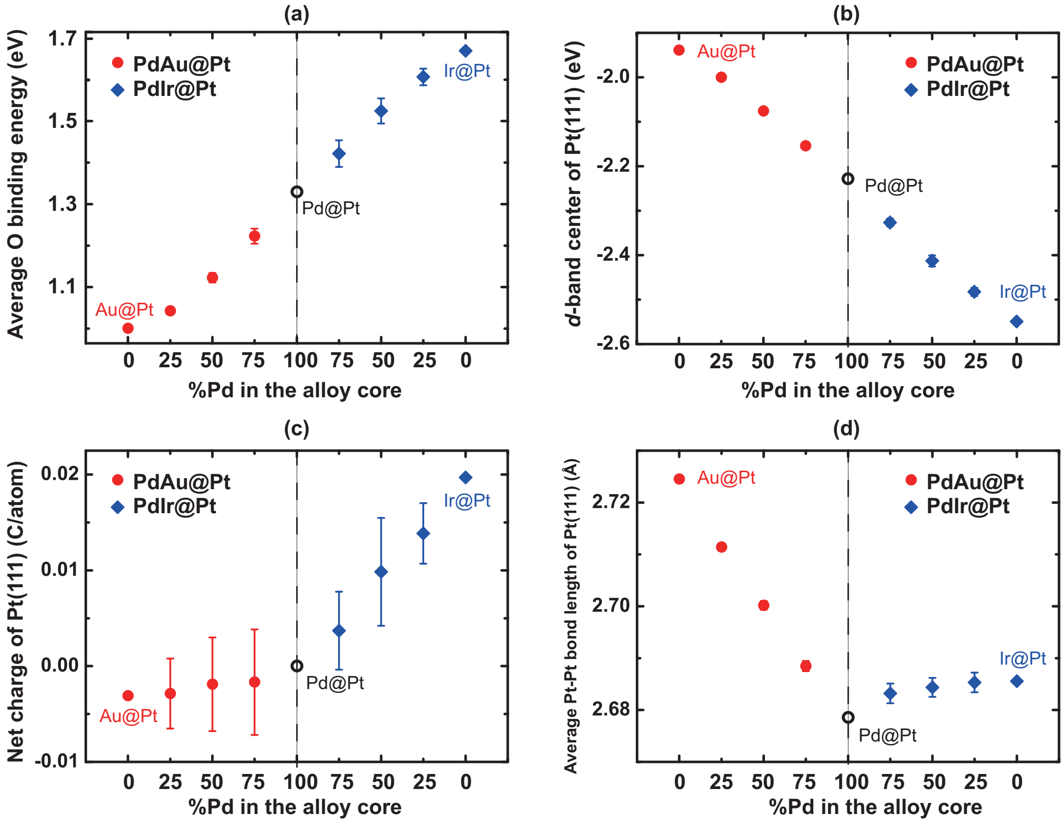

Figure 4.10: Effect of alloy Au and Ir into Pd core with Pt shell NP140. (a) Average O binding energy and (b) *d*-band center of Pt(111) facets are linearly tuned by the alloy core compositions. (c) Average net charge on Pt shell referenced to Pd@Pt, alloying Ir to Pd core has much more significant impact on charge redistribution. (d) Average Pt-Pt bond length on Pt shell, alloying Au to Pd core has much more significant impact on strain of the Pt shell.

4.6 Alloy-core Composition Optimization

We have shown there is a general linear correlation between the core composition and adsorbate binding of alloy-core@shell nanoparticles. In order to optimize the composition for catalytic reactions of interest, we need a model that correlates adsorbate binding with the overall catalytic activity. In the past decade, much work has been done to reduce the number of parameters used to describe the activity of complex reactions. Nørskov *et al.* proposed a systematic method to construct the Sabatier rate as a function of one or two key reactants' binding energy using mean-field micro-kinetic models[6, 5, 7]. Building upon on the adsorption energy scaling[8, 9] and Brønsted-Evans-Polanyi (BEP) relationships[6], this "Sabatier analysis method" significantly reduces the number of parameters and computational effort required for materials screening.

In the alloy-core@shell system, the binding energy of adsorbates are all functions of alloy-core composition. Two properties of alloy-core@shell structures gives rise to advantages in catalyst design. First, the number of descriptors for the reaction can be reduced to just one, that is the alloy-core composition. Second, the core composition with a desired adsorbate binding energy can be determined from the single-core@shell structures. In other words, by calculating adsorbate binding to the single-core@shell structures, we are able to explore the parameter space of alloy cores connected by any two structures with the same shell metal.

Following the theoretical framework of Nørskov *et al.* the Sabatier rate of a reaction $r_s(\mathbf{v})$ is constructed as a function of the reactivity descriptors $\{Eb^i\}$, where $\mathbf{v} = \{Eb^1, Eb^2, ..., Eb^n\}$ is the descriptor vector and Eb^i is the binding energy of key adsorbate. For the alloy-core@shell structures $\mathrm{X}_x\mathrm{Y}_{1-x}$@Z, the descriptor vector at an intermediate alloy-core composition x

can be estimated from a linear interpolation between the two single-core@shell structures as

$$\mathbf{v}(x) = x\mathbf{v}_{\mathrm{X@Z}} + (1-x)\mathbf{v}_{\mathrm{Y@Z}} \tag{4.5}$$

$\mathbf{v}_{\mathrm{X@Z}}$ and $\mathbf{v}_{\mathrm{Y@Z}}$ are the descriptor vector of X@Z and Y@Z, respectively. The Sabatier rate is then expressed as a function of alloy core composition x, and the extremum of the reaction rate of $\mathrm{X}_x\mathrm{Y}_{1-x}$@Z is achieved where

$$\begin{aligned}\frac{\partial r_s}{\partial x} &= \frac{\partial r_s}{\partial \mathbf{v}}\frac{\partial \mathbf{v}}{\partial x} \\ &= \nabla r_s \cdot (\mathbf{v}_{\mathrm{X@Z}} - \mathbf{v}_{\mathrm{Y@Z}}) = 0. \end{aligned} \tag{4.6}$$

In principal, the extremum composition can be obtained analytically by solving Eq. 4.6, where the gradient of the rate is normal to the vector connecting the two single-core@shell compositions. In a special case where the dimension of the descriptor vector is one, *e.g.* the ORR and HER, where the catalytic activity of the reaction can be described by the binding energy Eb of a single adsorbate[2, 108], Eq. 4.6 can be simplified as $\nabla r = \frac{\mathrm{d}r_s}{\mathrm{d}Eb} = 0$. If the reaction rate reaches its extremum at Eb^*, where $\frac{\mathrm{d}r_s}{\mathrm{d}Eb} = 0$, then the composition x^* with the extreme rate is

$$x^* = \frac{Eb^* - Eb_{\mathrm{Y@Z}}}{Eb_{\mathrm{X@Z}} - Eb_{\mathrm{Y@Z}}}. \tag{4.7}$$

To have $x^* \in [0, 1]$, the condition $(Eb^* - Eb_{\mathrm{X@Z}})(Eb^* - Eb_{\mathrm{Y@Z}}) < 0$ must be satisfied. In other words, X@Z and Y@Z must be on different sides of the volcano peak.

The above optimization scheme works on the basis of linear binding energy correlations for alloy-core@shell nanoparticles, as well as models that correlate binding with the catalytic activity. There are a couple of approximations in this approach which should be highlighted. First, in binding energy calculations the random alloy core compositions were held fixed. Thus effects of large geometric deformations due to variations of composition are not considered in our model. Structural rearrangements and alloy core segregation may cause deviations from the linear correlations presented. Second, the BEP relations and Sabatier analysis is essential to obtain the correlation of descriptors and activity. Uncertainties in both approximations will also affect the accuracy of this optimization scheme.

4.7 Application of Alloy-core@shell NP for Catalysis

4.7.1 Oxygen Reduction Reaction

Fuel cells show promise as a future power source that combines the high chemical energy density of fuels with high efficiency conversion to electricity and zero or low emissions. The widespread application of current proton exchange membrane fuel cells, however, is impeded by several limitations in the oxygen reduction catalyst at the cathode. As the best catalyst for the oxygen reduction reaction (ORR) so far, Pt-based materials still have some deficiencies, such as slow oxygen reduction kinetics and a high material cost, preventing them from being commercially valuable in large-scale (e.g. automotive) applications.

Bligaard *et al.* reported that O binding energy is an effective descriptor for ORR activity[6]. Nørskov *et al.* showed a volcano-shaped relationship between the ORR rate and the oxygen adsorption energy[2]. On one side of the volcano peak, O or OH strongly binds to the metal so that the reaction rate is limited by the removal of product (hydroxyl). On the other side of the peak, oxygen binds weakly to metals such as Ag and Au, and the kinetics are limited by high dissociation barriers. According to the volcano plot, the peak in activity is predicted to be at an oxygen binding slightly weaker than on a Pt(111) surface. In this paper, we choose a target oxygen binding energy of the Pt(111) surface, -1.51 eV, which is calculated on a 4 layer 3×3 slab model using a half of a free O_2 molecule as reference energy. Although oxygen binding on bulk Pt(111) is not necessarily the optimal for ORR, it gives a close enough estimate of the location of the volcano peak to understand trends in nanoparticle activity.

Table 4.1: Oxygen Binding Energy of Pd-shell NP140

M@Pd	group I			group II				
core metal	Au	Ag	Pd	Ir	Rh	Cu	Ru	Mo
BE_{O} (eV)	-1.81	-1.75	-1.72	-1.46	-1.41	-1.21	-1.12	-0.94

Table 4.1 lists the O binding energy of various kinds of Pd-shell NP140 with a single core element. Compared to a Pt(111) slab, these Pd-shell NP140 can be classified into two groups. Group I includes the strong O binding structures: Au@Pd, Ag@Pd, and Pd@Pd; while Group II contains structures with weaker O binding: Ir@Pd, Rh@Pd, Cu@Pd, Ru@Pd, and Mo@Pd. The more

Table 4.2: Optimal Ratio X^* of Metal X Alloyed with Metal Y in the Core Of A X_xY_{1-x}@Pd NP140

M@Pd	metal Y		
metal X	Au	Ag	Pd
Ir	0.86	0.83	0.81
Rh	0.75	0.71	0.68
Cu	0.49	0.44	0.41
Ru	0.43	0.38	0.35
Mo	0.34	0.29	0.27

noble the core metal is, the more reactive the corresponding Pd-shell nanoparticles are. For instance, Au itself is known to have the weakest O binding among all the transitional metals, however Au@Pd binds O most strongly of the Pd-shell particles. Follow the above optimization strategy, the target O binding of a Pd-shell particle can be achieved by alloying a metal X from the second group (X=Ir, Rh, Cu, Ru, Mo) with metal Y from the first group (Y=Au, Ag, Pd) in core. The optimal ratio x^* for the X_xY_{1-x}@Pd nanoparticle calculated by Eq. 4.7 are listed in Table 4.2 with a Eb^* of -1.51eV. Similar procedure can be applied to Pt-shell NP140 as well.The predicted optimal alloy-core compositions shown in Figure 4.7 are summarized in Table 4.3.

Table 4.3: Optimal Ratio X^* of Metal X Alloyed with Metal Y in the Core Of A X_xY_{1-x}@Pt NP140

M@Pd	metal Y	
metal X	Au	Ag
Pd	0.72	0.30
Ir	0.35	0.09
Rh	0.30	0.08
Ru	0.22	0.07
Cu	0.19	0.05

4.7.2 Examination of PdAu@Pt NP for ORR

Because Au is easier to work with than Ag, we selected PdAu@Pt DENs as our model system for comparison with the foregoing calculations. Briefly, Pd_nAu_{140-n} DENs were synthesized electrochemically by Cu UPD onto Pd_nAu_{140-n} alloy cores, followed by galvanic exchange of the Cu layer for Pt. The methodology used to prepare these alloy-core@shell DENs is similar to one we have previously reported[30]. The ORR activity of Au140, Pt_{140}, $Pd_{70}Au_{70}$, and Pd_nAu_{140-n}@Pt (n = 70, 90, 105, and 120) DENs was then determined using rotating disk voltammetry[25]. Note that the subscripts used here reflect the nominal elemental compositions of the DENs based on the percentages of Pd and Au used to prepare them. We have previously shown that these values are good (but not perfect) estimates of the experimentally determined stoichiometry of the nanoparticles[33, 34].

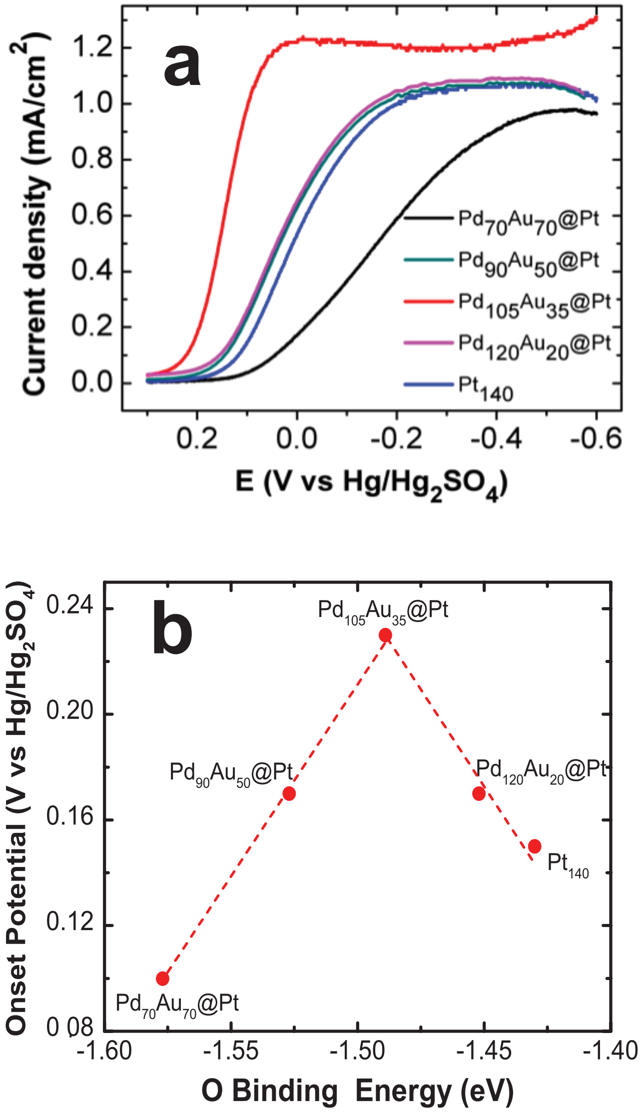

Figure 4.11: (a) Rotating disk voltammograms for glassy car- bon electrodes modified with Pd$_n$Au$_{140-n}$@Pt(n = 70, 90, 105, 120) and Pt140 DENs. (b) Onset potential for the ORR at Pd$_x$Au$_{1-x}$@Pt@Pt DENs measured by RDVs and plotted as a function of the corresponding oxygen binding energy calculated by DFT.

Figure 4.11(a) shows a series of rotating disk voltammograms (RDVs) for glassy carbon electrodes modified with Pd_nAu_{140-n}@Pt and Pt_{140} DENs. The RDVs were obtained in O_2-saturated, aqueous 0.10 M $HClO_4$ using a rotation rate of 1600 rpm at a scan rate of 5 mV/s. The onset potential for the ORR, which is defined as the potential of the inflection point on the quasi-steady-state polarization curve, at the $Pd_{70}Au_{70}$ DEN-modified electrode is -0.30 V. However, upon addition of the Pt shell, this value shifts positive to 0.10 V. For comparison, the ORR onset potential for the Pt_{140} DENs is at 0.15V which is more positive than that of the $Pd_{70}Au_{70}$@Pt electrocatal 4.11(a)yst. However, the ORR onset potentials for $Pd_{90}Au_{50}$@Pt and $Pd_{120}Au_{20}$@Pt DENs are shifted even more positive, to 0.17 V. The onset potential for the $Pd_{105}Au_{35}$@Pt DENs shifts much more positive, to 0.23 V, than any of the other DENs, and hence it has the lowest over potential and highest activity. Figure 4.11(b) summarizes the RDV data by showing the onset potential for the ORR as a function of corresponding O binding energy calculated from DFT. The measured activities exhibit a volcano-shaped trend when plotted against the theoretically determined O binding energy. The peak of the volcano, corresponding to $Pd_{105}Au_{35}$@Pt or 75% Pd in the core, is in very good agreement with our theoretical prediction of 72% Pd. Additionally, a Pt shell reduces the Pt loading as compared to a pure Pt particle. Figure 4.12 shows the average oxygen binding energy trend of PdAu@Pt NP140 in comparison to a bulk PdAu alloy substrate supporting a monolayer of Pt, denoted as PdAu/Pt. The latter system was chosen to compare with the larger (5.4

nm) PdAu@Pt nanoparticles studied by Adzic and co-workers[100]. Details of these slab calculations can be found in the Supporting Information. Notably, there is a shift in optimal core composition for our ∼2 nm DENs (72%) as compared to the slab geometry (90% Pd). The later composition was chosen by the Adzic group for their 5.4 nm nanoparticles. The shift of the activity peak with composition can be explained from two factors: (1) there is weaker O binding to the DENs; and (2) alloying Au to Pd has a more significant effect on the O binding energy to the slab. These factors correspond to the differences in intercepts and slopes of the trend lines in Figure 4.12, respectively. As we showed earlier in this section strain effect plays dominant role in PdAu@Pt system. These two factors can be understood in terms of a strain effect. The shell of Pd@Pt NP140 has an average Pt-Pt bond length of 2.68 Å, which is about 0.07 Åshorter than the surface Pt layer of the Pd/Pt slab. The shorter Pt-Pt bond length causes a higher strain, leading to a weaker oxygen binding energy. On the other hand, the Pt-Pt bond length difference between Pd@Pt and Au@Pt is 0.04 Å, which is smaller than the difference between Pd/Pt and Au/Pt (0.14 Å), resulting in a reduced effect of alloying Au to Pd on the O binding energy.

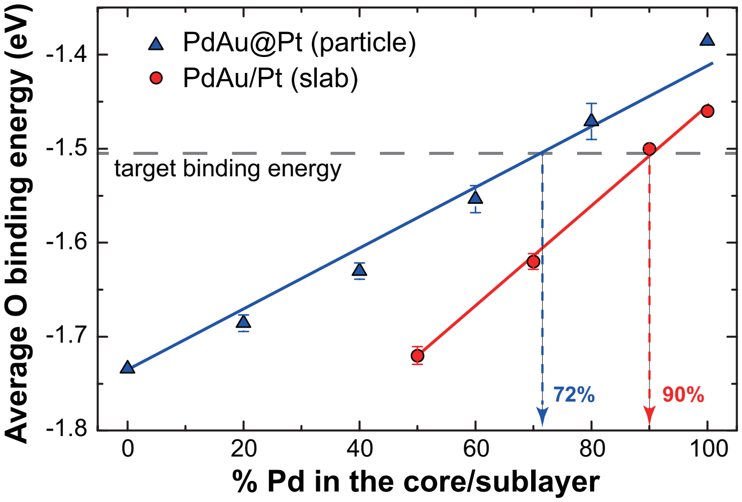

Figure 4.12: Trends of average oxygen binding energy as a function of core composition for Pd_xAu_{1-x}@Pt (nanoparticle geometry) and Pd_xAu_{1-x}/Pt (slab geometry).

We synthesized and tested additional Pd_nAu_{140-n}@Pt DEN compositions and were gratified to find that the activity of these electrocatalysts fell almost exactly on the predicted trend lines. Hence, this is an interesting case of first-principles theory leading to nearly perfect agreement with experimental results. We believe that this tuning mechanism is a general property of the alloy-core@shell system and hence provides a systematic means for designing nanoparticles to have desirable catalytic activity.

4.7.3 Hydrogen Evolution Reaction

The HER is the cathode reaction in water electrolysis, where hydrogen is produced from proton reduction. It was first proposed by Parsons that the free energy of hydrogen adsorption ΔG_{H} is a good reaction descriptor of the HER, and the optimal activity is near $\Delta G_{\mathrm{H}} = 0$[109]. With well-defined approximations for the zero point energy and entropy, the free energy of hydrogen adsorption on different surfaces can be calculated as $\Delta G_{\mathrm{H}} = Eb_{\mathrm{H}} + 0.24$ eV, where Eb_{H} is the binding energy of hydrogen atom on the surface[108]. Since this 0.24 eV shift is constant over different surface, the alloy-core composition optimization strategy of Eq. 4.7 is applicable to the HER. Table 4.4 lists the free energy of adsorption for hydrogen on a variety of single-core@Pd-shelled and Pt-shelled slabs. For both Pd and Pt shelled slab, the free energy of adsorption is negative when the core is Au, Ag, Pd, or Pt, and it is positive with cores of Ir, Rh, Ru, or Cu. In order to satisfy $x^* \in [0, 1]$, a metal X must be selected from {Au, Ag, Pd, Pt} and a metal Y from {Ir, Rh, Ru, Cu} to form an optimal alloy core. ΔG_{H} on $\mathrm{X}_x\mathrm{Y}_{1-x}$@Z (X = Au, Ag, Pd, Pt; Y = Ir, Rh, Ru, Cu; Z = Pd, Pt) will be tuned to zero, when the ratio of X in the alloy core is x^*. Table 4.5 lists the optimal compositions x^*. Notably, Table 4.5 shows that PtRu@Pd has the best HER performance at a Pt:Ru ratio of 1:1 in the alloy core. This is in a good agreement with pervious reports by Greeley *et al.*[110, 111].

Table 4.4: Free Energy of Adsorption for Hydrogen ΔG_{H} (eV) on a Variety of Pd- and Pt-shelled Slabs.

	core metals							
structures	Au	Ag	Pd	Pt	Ir	Rh	Ru	Cu
Pd-shell	-0.25	-0.22	-0.18	-0.18	0.10	0.11	0.17	0.25
Pt-shell	-0.27	-0.24	-0.11	-0.05	0.22	0.24	0.33	0.41

Table 4.5: Optimal Ratio x^* of Metal X Alloyed with Metal Y in the Xore of Pt- and Pd-covered Slabs for the HER.

	metal X							
	Pd-shell				Pt-shell			
metal Y	Au	Ag	Pd	Pt	Au	Ag	Pd	Pt
Ir	0.71	0.69	0.64	0.64	0.55	0.52	0.33	0.19
Rh	0.69	0.67	0.62	0.62	0.53	0.50	0.31	0.17
Ru	0.60	0.56	0.51	0.51	0.45	0.42	0.25	0.13
Cu	0.50	0.47	0.42	0.42	0.40	0.37	0.21	0.11

4.7.4 CO Oxidation

CO oxidation has been widely studied as a model catalytic reaction on a wide variety of systems, such as metal surfaces, clusters, and supported metal clusters. There are two primary reaction mechanisms involved: (1) the dissociative mechanism (R1-4), consisting of O_2 dissociation and subsequent association with CO to form CO_2; and (2) the associative mechanism (R5), which is active when the pressure of O_2 is high enough and the O_2 molecules can oxidize CO directly without dissociation[112, 10].

$$\mathrm{CO} + * \Longleftrightarrow \mathrm{CO}^* \tag{R1}$$

$$\mathrm{O}_2 + * \Longleftrightarrow \mathrm{O}_2^* \tag{R2}$$

$$\mathrm{O}_2^* + * \Longleftrightarrow 2\mathrm{O}^* \tag{R3}$$

$$\mathrm{CO}^* + \mathrm{O}^* \Longleftrightarrow \mathrm{CO}_2 + 2* \tag{R4}$$

$$\mathrm{CO}^* + \mathrm{O}_2^* \Longleftrightarrow \mathrm{CO}_2 + \mathrm{O}^* + * \tag{R5}$$

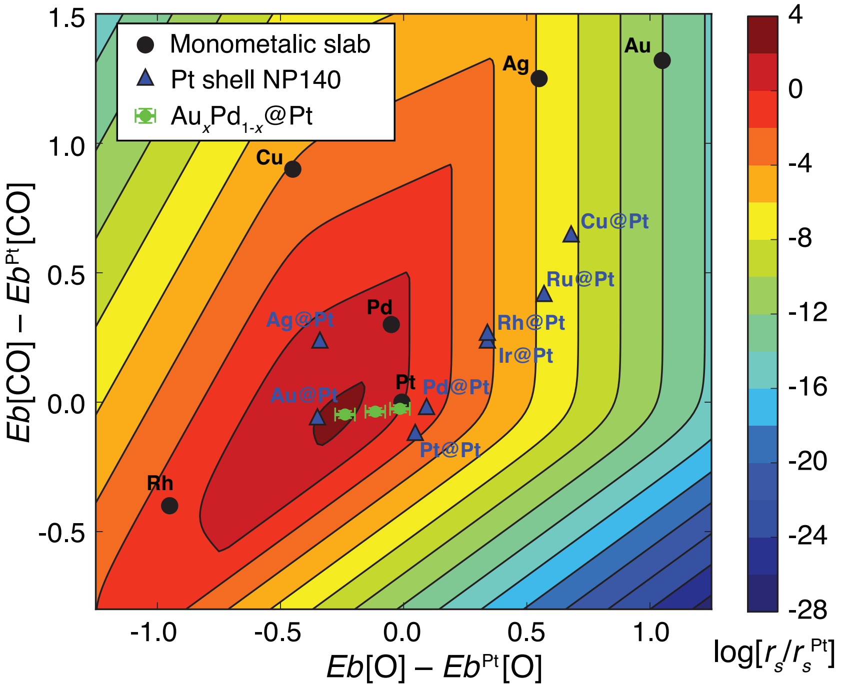

Figure 4.13: Contour plot of the relative Sabatier rate r_s/r_s^{Pt} on a logarithmic scale as a function of $Eb[\mathrm{O}] - Eb^{\mathrm{Pt}}[\mathrm{O}]$ and $Eb[\mathrm{CO}] - Eb^{\mathrm{Pt}}[\mathrm{CO}]$. The contours are reproduced from the model in Falsig's work[10]. Of the pure metal slabs (black circles) Pt emerges as the best catalyst. Several single-core@Pt-shell particles are also of high activity (blue triangles) with $\mathrm{Pd}_x\mathrm{Au}_{1-x}$@Pt NP140 (green points) passing close to the volcano peak.

Based upon these mechanisms (R1-R5), Falsig *et al.* built a volcano plot of the Sabatier rate over a closed-packed metal surface as function of the O and CO binding energies, $Eb[\mathrm{O}]$ and $Eb[\mathrm{CO}]$[10]. In this work, we have calculated $Eb[\mathrm{O}]$ and $Eb[\mathrm{CO}]$ for several single-core@Pt-shell NP140 and explored potential alloy-core@shell structures for CO oxidation based on Falsig's Sabatier rate model. In Fig. 4.13 we reproduce Falsig's contour plot of relative Sabatier activity for CO oxidation $\log[r_s/r_s^{\mathrm{Pt}}]$ as a function of

$Eb[\mathrm{O}] - Eb^{\mathrm{Pt}}[\mathrm{O}]$ and $Eb[\mathrm{CO}] - Eb^{\mathrm{Pt}}[\mathrm{CO}]$ under high-temperature conditions (T=600 K, $p_{\mathrm{O_2}}$=0.33 bar and p_{CO}=0.67 bar). We chose the Pt(111) slab as our reference because Pt(111) is one of the best catalysts under high-temperature conditions. The two single-core@Pt-shell NP140, Au@Pt and Ag@Pt, emerge as good candidates with comparable or higher activity of Pt(111). It is also possible to tune the activity even higher because there is a gap between these particles and the peak of the volcano.

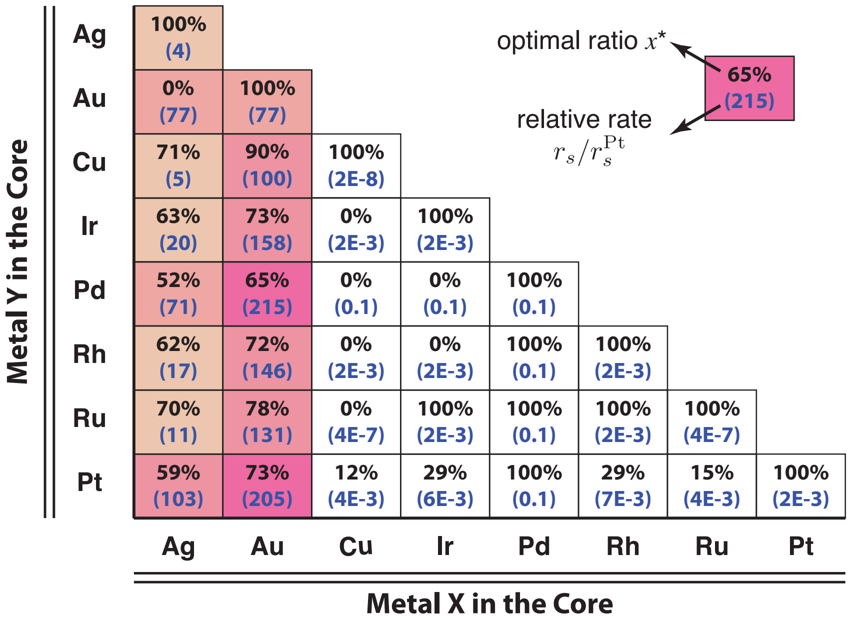

	Ag	Au	Cu	Ir	Pd	Rh	Ru	Pt
Ag	100% (4)							
Au	0% (77)	100% (77)						
Cu	71% (5)	90% (100)	100% (2E-8)					
Ir	63% (20)	73% (158)	0% (2E-3)	100% (2E-3)				
Pd	52% (71)	65% (215)	0% (0.1)	0% (0.1)	100% (0.1)			
Rh	62% (17)	72% (146)	0% (2E-3)	0% (2E-3)	100% (0.1)	100% (2E-3)		
Ru	70% (11)	78% (131)	0% (4E-7)	100% (2E-3)	100% (0.1)	100% (2E-3)	100% (4E-7)	
Pt	59% (103)	73% (205)	12% (4E-3)	29% (6E-3)	100% (0.1)	29% (7E-3)	15% (4E-3)	100% (2E-3)

Figure 4.14: Optimal ratio x^* of metal X alloyed with metal Y in the core of Pt-shelled NP140 for COox estimated from Falsig's Sabatier rate model. The blue numbers in brackets at the bottom of each cell is the calculated relative Sabatier rate r_s/r_s^{Pt} at the optimal alloy-core composition. The COox rate for $\mathrm{Au_{0.65}Pd_{0.35}}$@Pt and $\mathrm{Au_{0.73}Pt_{0.27}}$@Pt particles are 200 times that of a Pt(111) slab.

A quick way to understand how the alloy-core particles can be tuned is to draw a line connecting any two different single-core@Pt-shell NP140 on the contour plot. If the line intersects a region of high activity, a promising catalytic material can be achieved by alloying the elements of the endpoint particles in the core. As illustrated in Fig. 4.13, a line between the Au@Pt and Pd@Pt particles passes near the volcano peak. The green scatter points between Au@Pt and Pd@Pt represents $\mathrm{Pd}_x\mathrm{Au}_{1-x}$@Pt NP140, with $x = 0.25$, 0.50, and 0.75. The distribution of Eb[O] and Eb[CO] due to the different alloy cores and binding sites sampled is indicated by the error bars. Several other core element combinations also have the potential to reach the highly active region; a selection is presented in Fig. 4.14. In each cell of the table, the fraction on top is the optimal ratio x^* of metal X in the alloy core, and the blue number in brackets show the relative rate at this optimal alloy-core composition, which is also the highest activity this $\mathrm{X}_x\mathrm{Y}_{1-x}$@Pt-shell NP140 can attain. If $x^* = 0\%$, Y@Pt NP140 has the best performance for $\mathrm{X}_x\mathrm{Y}_{1-x}$@Pt and alloying X in the core will not improve the reactivity; while $x^* = 100\%$ indicates that X@Pt is the most reactive composition.

Highlighting one example, the CO oxidation activity of Ag- and Au-core@Pt-shell particles can be enhanced by alloying other transition metals into the core. As shown in Fig. 4.14, the CO oxidation rate of alloy-core@Pt NP140 with core compositions $\mathrm{Au}_{0.90}\mathrm{Cu}_{0.10}$, $\mathrm{Au}_{0.73}\mathrm{Ir}_{0.27}$, $\mathrm{Au}_{0.65}\mathrm{Pd}_{0.35}$, $\mathrm{Au}_{0.72}\mathrm{Rh}_{0.28}$, $\mathrm{Au}_{0.78}\mathrm{Ru}_{0.22}$, $\mathrm{Au}_{0.73}\mathrm{Pt}_{0.27}$ and $\mathrm{Ag}_{0.59}\mathrm{Pt}_{0.41}$ are two orders of magnitude faster the rate of CO oxidation on the Pt(111) surface. A 200 fold increase over Pt(111) is predicted for $Au_{0.65}Pd_{0.35}$@Pt and $Au_{0.73}Pt_{0.27}$@Pt. In the case of the PdAu@Pt system, Pd@Pt is limited by the O_2 dissociation process (R3) due to its relatively weak O binding. Alloying Au to the Pd core enhances both O and CO binding. On one hand, strengthened O binding facilitates the O_2 dissociation step; On the other hand, the barrier of CO oxidation step (R4) grows with stronger O and CO binding. The tradeoff of these two effect gives rise to a peak activity at a composition with 65% Au in the core. With less than 65% Au in the core, the overall reactivity is limited by O_2 dissociation; with more than 65% Au, the overall reactivity is limited by CO oxidation by atomic O (R4).

4.8 Stability of Pt and Pd Shell Nanoparticles

Another important consideration for nano-alloy catalysts is their stability. The relative surface energies and adsorbate binding are the two major factors contributing to their thermodynamic stability[113, 114]. Previous studies have used the surface segregation energy as a measure of the thermodynamic stability of near surface alloys[115, 116]. Here we follow the same strategy to investigate the stability in terms of the core/shell segregation energy of (111) facet atoms in our Pt and Pd shelled nanoparticles with monometallic cores. The core/shell segregation energy is calculated as the energy required to swap one shell atom (Pt or Pd) and its neighboring subsurface atom. Stability under reaction condition was also evaluated by considering adsorbates (O, C, H, N, S, CO and NO) bound at the surface site for which the segregation energy is calculated.

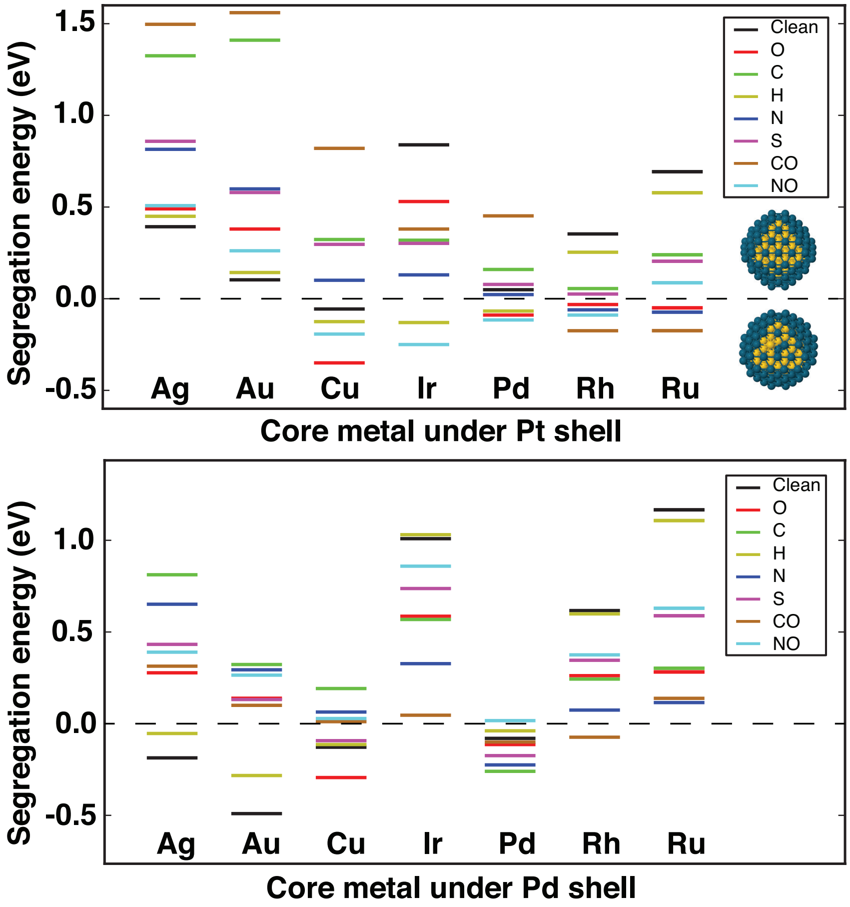

Figure 4.15: Calculated segregation energy of Pt shell nanoparticle with and without adsorbates (O, C, H, N, S, CO and NO).The insets indicate preferred structures according to the segregation energy.Adsorbates are not shown on the inserts.

Fig 4.15 shows the calculated segregation energy of Pt- and Pd- shelled nanoparticles with and without adsorbates. Here we mainly focus on Pt-shelled nanoparticles, similar discussion can be extended to Pd-shelled nanoparticles as well. The majority of the systems considered on the plot are thermodynamically stable, with positive segregation energies. Without adsorbates, all of the Pt nanoparticles are thermodynamically stable with positive segregation energy except for Cu@Pt. Ag and Au are less reactive than Pt, so that the presence of adsorbed increases the energetic cost of core/shell swapping, results in a enhanced stability. Ir, Rh and Ru bind the adsorbates more strongly than Pt, and their presence lowers the energy required for segregation. Due to the similarity of Pd and Pt, all segregation energies of Pd@Pt are close to zero, except in the case of CO where extra stability is gained. For HER, Ag, Au, Rh and Ru in the core of Pt shell nanoparticles are both stable in vacuum and a H rich environment.

For the systems identified as good candidates for CO oxidation, AgPd@Pt and AuPd@Pt, Ag and Au are stable under the Pt shell under all conditions. Pd@Pt has a positive segregation energy in vacuum and in a CO rich environment. Although the thermodynamic stability of the Pd@Pt nanoparticle is reduced with surface-bound oxygen species, it has been reported that introducing Au or Ag to the Pd core can enhance the stability and durability of a Pt surface layer under ORR conditions[99, 117]. It is also worth noting that nanoparticles with negative segregation energy may still be kinetically stable. For example, Cu@Pt adsorbed by O has the most negative segregation energy in the systems we investigated. However, however, Cu was found to be kinetically stable in the core of PdCu@Pt particles and more active in ORR experiments than Pd@Pt particles[118].

4.9 Conclusions

We have shown general linear correlations between the adsorbate binding energy to the shell of an alloy-core@shell nanoparticle and the composition of the core. This relationship allows for interpolation of the properties of single-core@shell particles and an approach for tuning the catalytic activity of the particle. Application to ORR, HER and COox reactions reveals a series of promising catalysts.Electrochemical measurements of ORR activities of AuPd@Pt dendrimer-encapsulated nanoparticles (DENs) are in a good agreement with the theoretical prediction that the peak of activity is achieved for a 28% Au/72% Pd alloy core supporting a Pt shell. A previously reported $Pt_{0.5}Ru_{0.5}$@Pd for HER is identified by this approach; many other predictions have not yet been tested. While our demonstration is only for the HER and COox reactions, this method of tuning catalytic activity provides a general framework for computational optimization of alloy-core@shell nanoparticles for other reactions of interest.

Chapter 5

CO Oxidation at the Interface of Bimetallic Nanoclusters Supported on $CeO_2(111)$

5.1 Abstract

DFT+U calculations of the structure of $CeO_2(111)$ supported Au-based bimetallic nanoclusters (NCs) show that a strong support-metal interaction induces a preferential segregation of the more reactive element to the NC-CeO_2 perimeter, generating an interface with the Au component. We studied several Au based bimetallic NCs (Au-X, X: Ag, Cu, Pd, Pt, Rh, and Ru) and found that (Au-Cu)/CeO_2 is optimal for catalyzing CO oxidation via a bifunctional mechanism. O_2 preferentially binds to the Cu-rich sites whereas CO binds to the Au-rich sites. Engineering a two-component system in which the reactants do not compete for binding sites is the key to the high catalytic activity at the interface between the components.

5.2 Introduction

The critical role of the interface between a supporting oxide and supported metal nanoparticles (NPs)/nanoclusters (NCs) has been highlighted by many experimental and theoretical studies[119, 120, 121, 122, 123, 124, 125, 126, 127, 128, 129, 130, 131, 132]. Moreover, recent studies are suggesting that interfaces in nanocatalysts can be designed at the atomic scale for specific purposes. The Rodriguez and Adzic groups, in particular, have reported various kinds of tunable interfaces; metal and oxide[127, 130, 133, 134, 135, 136], metal and carbide[137], and oxide and oxide[120, 130, 135, 138], and highlighted the important role of these interfaces for various heterogeneous catalytic reactions.

Since Haruta's pioneering finding on the excellent catalytic activity of oxide supported Au nanoparticles (NPs), the oxidation chemistry of oxide supported Au NPs or nanoclusters (NCs) has been studied extensively, with a focus on a determination of the active site[119, 120, 123, 125, 126]. Of particular interest is how the system is able to activate the oxygen molecule to give the high activity observed experimentally. Theoretical studies of O_2 activation by supported or unsupported Au NPs/NCs have reported low O_2 binding energies and high O_2 dissociation barriers[139] . In our previous study of CO oxidation by CeO_2 supported Au NCs (Au/CeO_2), we found a relatively strong CO binding as compared to O_2 on the Au NC or Au/CeO_2(111), leading to CO poisoning and a low oxidation rate. These results suggest that a different reaction mechanism is available that involves another source of oxygen[120]. In this regard, the oxygen spillover mechanism[119, 120, 124, 132], the Mars-van Krevelen (M-vK) mechanism of CO oxidation[119, 132], and O_2 binding at the Au-support interface[120, 122] are considered as better alternatives to explain the rich chemistry of CO oxidation by oxide supported Au catalysts that is observed experimentally. We have previously reported that the low-coordinated interfacial oxygen atoms oxidize CO bound to Au NCs (Au-CO*) by the M-vK mechanism of CO oxidation, emphasizing the role of the NC-CeO_2 interface[132].

We suggest a strategy to improve the catalytic activity of Au NPs/NCs by more intensive interface engineering, utilizing the strong metal-support interaction. We study a set of CeO_2(111) supported Au based bimetallic NCs comprised of 10 atoms (Au_7-X_3, where X is Ag, Cu, Pd, Pt, Rh, or Ru) and find that a strong oxygen affinity of the alloying elements, X, drives their preferential segregation to the NC-CeO_2(111) perimeter. Segregation of the metal components results in three interfaces between Au, CeO_2, and the alloying element. CO oxidation at these interfacial sites is examined using density functional theory (DFT). The different alloying elements change the reaction energetics; Cu is found to produce a particularly active CO oxidation mechanism at the interface with Au.

5.3 Computation Models and Methods

A 4×4 CeO_2(111) slab model with 6 atomic layers and 20 Åof vacuum was prepared to describe the CeO_2 support. Sensitivity tests on the model parameters (energy cutoff, k-point sampling, and system size) showed that our calculation parameters reasonably describes the energetics of the oxidation catalysis by CeO_2 supported Au NP/NCs[119, 120, 132]. A highly symmetric hexagonal two-layered Au NC composed of 10 atoms was supported on the CeO_2(111) surface (Figure 5.1a). The entire Au/CeO_2 system was fully optimized prior to catalysis studies.

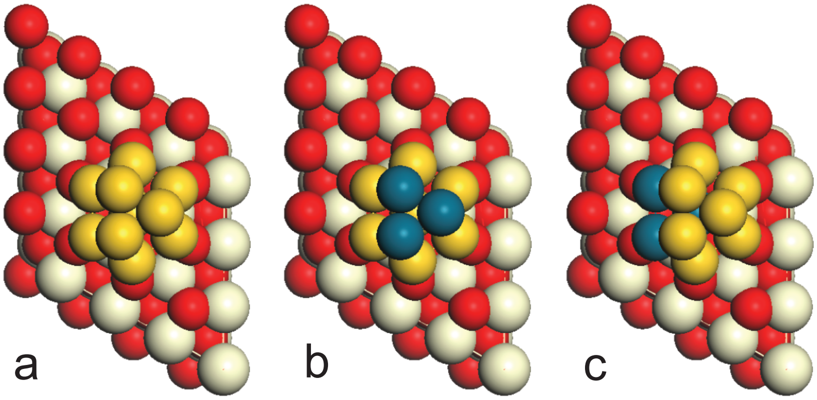

Figure 5.1: Au_{10} (a) and Au_7X_3 (b,c) clusters supported on the $CeO_2(111)$ surface. Yellow, ivory, and red spheres represent Au, Ce, and O atoms, respectively. Green spheres in panels b and c represent the initial and final location of alloying element. Energetics associated with the segregation of alloying element to the NC-CeO_2 interface (from b to c) are shown in Table 5.1.

We performed spin-polarized DFT calculations with the VASP code[63, 64] using the PBE[140] functional. In order to treat the highly localized Ce 4f-orbital, DFT+U[141] with Ueff = 5 eV was applied[119, 120, 132]. The interaction between the ionic core and the valence electrons was described by the projector augmented wave method[66, 67] and the valence electrons with a plane wave basis up to an energy cutoff of 400 eV. The Brillouin zone was sampled at the Γ-point. The convergence criteria for the electronic structure and the atomic geometry were 10^{-4} eV and 0.01 eV/Å, respectively. Sensitivity tests show that our results are robust with respect to the calculation and model parameters, including the k-point grid, cutoff energy, and thickness of the slab[119, 120, 132]. Increasing the energy cutoff to 500 eV changed the co-adsorption energy of CO and O_2 on the segregated CeO_2/AuCu cluster (considering both co-adsorption geometries) by less than 0.004 eV. A similar change in binding energy was found for increasing the k-point mesh and the slab thickness. The location and energy of transition states (TSs) were calculated with the climbing-image nudged elastic band method[142, 143]. Reaction energetics of CO oxidation catalysis was calculated with reference to the energy of gas phase CO and O_2.

5.4 Segregation of Bimetallic Nanoclusters

To study the effect of the $CeO_2(111)$ support on the structure of supported Au-X bimetallic nanoparticles, three Au atoms in the top layer of the Au_{10} NC were replaced with one of the following alloying elements; Ag, Cu, Pd, Pt, Rh, or Ru (Figure 5.1b). The preferred geometry for the alloying elements in the clusters was determined using two metrics. First, the segregation energy E^{seg}_{w/CeO_2} is calculated as the energy gained by exchanging three alloying atoms at the top layer of the $(Au_7\text{-}X_3)/CeO_2$ with bottom layer Au atoms, as shown in Figure 5.1c. A second measure the segregation energy $E^{seg}_{w/o,CeO_2}$ for the same process without CeO_2 support, in other word, the exchange enengy in gas phase for detail). Thus CeO_2 induced preferential segregation energy, E^{seg}_{pref}, can be defined as the change in exchange energy between a supported cluster and a gas phase cluster, $E^{seg}_{pref} = E^{seg}_{w/CeO_2} - E^{seg}_{w/o,CeO_2}$. As such, E^{seg}_{pref} indicates whether the bond energy between the X and the CeO_2 surface is stronger than to Au. Calculations of CO and O_2 adsorption, as well as the subsequent CO oxidation catalysis were examined on the most stable cluster.

Table 5.1: DFT Calculated values of E^{seg}_{w/CeO_2}, $E^{seg}_{w/o,CeO_2}$ and E^{seg}_{pref} for AuX/CeO$_2$ (X=Ag, Cu, Pd, Pt, Rh)

	Alloying Elements					
Segregation Energy(eV)	Ag	Cu	Pd	Pt	Rh	Ru
E^{seg}_{w/CeO_2}	-0.89	-2.56	-1.30	-1.25	-2.63	-3.69
$E^{seg}_{w/o,CeO_2}$	-0.74	-1.17	-0.97	-0.94	-0.98	-2.08
E^{seg}_{pref}	-0.15	-1.39	-0.33	-0.31	-1.65	-1.61

We have previously reported that the bonding between the CeO$_2$ support and the supporting Au NC is governed by the hybridization of Au-5d and O-2p orbitals[132]. The same nature of bonding between the Au-X and CeO$_2$ support was found here (see Figure 5.2). The calculated values of E^{seg}_{pref} in the Au-X systems shows that CeO$_2$ prefers to bond with the alloying element rather than with Au atoms, showing that the CeO$_2$ support induces a preferential segregation of the oxophilic element to the (Au-X)-CeO$_2$ perimeter (see Table 5.1). The effect of the CeO$_2$ support on the preferential segregation of the alloying element to the NC-CeO$_2$ interface is more prominent in the system where E^{seg}_{pref} is greater than $E^{seg}_{w/o,CeO_2}$ including Au-Cu, Au-Rh, and Au-Rh NCs. These systems were considered for further CO oxidation studies.

In Au-Ag, Au-Pd, and Au-Pt NCs, the energy acquired from the CeO$_2$-X bond formation, E^{seg}_{pref} is smaller than the energy gained from the surface

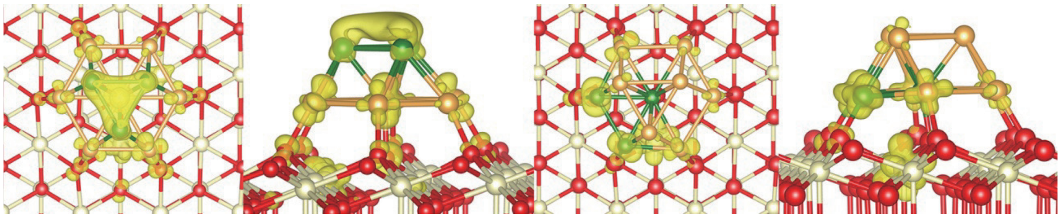

Figure 5.2: Density plots of highest occupied Kohn-Sham molecular orbitals of the (Au-Cu)/CeO_2 NP: (left) Cu at the top layer, and (right) Cu at the NP-CeO_2 interface. Bonding between Au-Cu NP and CeO_2 is thorough metal-O bonds (hybridization of metal-d and O-p orbitals).

energy reduction, $E^{seg}_{w/o,CeO_2}$, indicating that the CeO_2-X bond formation is not strong enough to induce a segregation of the alloying element to the NC-CeO_2 interface. In larger NPs, therefore, the alloying element is expected to be found in the core of the Au-X NP rather than at the NP-CeO_2 interface.

A strong interaction between the CeO_2 support and supported NPs/NCs, and especially on the defective or stepped CeO_2 surfaces, has been previously reported[120, 132, 144, 145]. In the case of Au NPs/NCs a strong interaction with the support is advantageous because pinned Au NPs/NCs are less susceptible to deactivation due to thermal sintering. Adding small amounts of an oxophilic alloying element to Au NPs/NCs can generate a pinning site of Au NPs/NCs on the Au NPs/NCs perimeter, and increase the lifetime of the catalyst.

5.5 Catalytic Activity for CO oxidaiton

In a previous study of CO oxidation on the Au NC of the Au/CeO_2 by the Langmuir-Hinshelwood mechanism it was found that even though the activation energy of CO oxidation by the Au-O_2* and Au-O* are both very low, an asymmetrically strong CO binding (E_{ad} = -1.05 eV) on the Au NC hinders the coadsorption of O_2 (E_{ad} = - 0.56 eV) leading to a low O_2 surface concentration and a low reaction rate[120]. In the case of this Au_{10}/CeO_2 model catalyst we confirmed again that the Au_3 top layer preferentially binds CO over O_2, so that this surface acts as a source of bound CO molecules. However, in the case of (Au-X)/CeO_2, we hypothesize that the oxophilic alloying element would generate a potential oxygen binding site, resulting in a different catalytic behavior as compared to the monometallic supported Au cluster. To validate our hypothesis we calculated the binding energy of reactants (CO and O_2) on the Au-X and X-X sites of the (Au-Cu)/CeO_2, (Au-Rh)/CeO_2, and (Au-Ru)/CeO_2 catalysts, where the alloying element is segregated to the NC-CeO_2 interface.

Table 5.2 shows the energy of CO and O_2 binding on the Au-X and X-X sites of tested catalysts and corresponding surface concentration of CO and O_2 at the binding site. The binding sites in the Au-Ru and Au-Rh systems that bind CO more strongly than O_2 would be saturated by CO when the catalyst is exposed to the CO oxidation condition (see Table 5.2). Because these systems do not have a preferential O_2 binding site, and their CO binding energy is higher than the Au/CeO_2 system, CO poisoning at the surface of Au-Rh and Au-Ru NCs would prevent CO oxidation by the Langmuir-Hinshelwood mechanism.

We should note here that DFT at the GGA level of theory is known to

Table 5.2: Binding Energy and Surface Concentration of CO and O_2 of Studied (Au-X)/CeO_2 Catalysts.Values in the parentheses represent the surface concentration of the corresponding reactant at 298 K, $p(O_2) = 0.21$, and $p(CO) = 0.01$.

		Au-X clusters on CeO_2		
Sites	Molecule	Au-Cu	Au-Rh	Au-Ru
Au-X	O_2	-0.64 (0.997)	-1.02 (0.00)	-1.19 (0.00)
	CO	-0.57 (0.003)	-1.37 (1.00)	-1.64 (1.00)
X-X	O_2	-0.77 (1.00)	-1.57 (0.007)	-1.31 (0.00)
	CO	-0.60 (0.00)	-1.78 (0.993)	-1.77 (1.00)

have systematic errors in the binding energy of molecules, arising for example, from the reference energy of gas-phase O_2. Thus, the relative binding energies and the relative reaction rates between different catalysts (as reported in Table 5.2) should be trusted more than the absolute values.

An oxygen spillover mechanism, involving the diffusion of a lattice oxygen atom of the CeO_2 support to the supported oxophilic metal NPs/NCs was found to be endothermic in the Au-Rh and Au-Ru systems; 0.77 eV and 0.63 eV in the (Au-Rh)/CeO_2 and (Au-Ru)/CeO_2, respectively. Even the O_2 binding energy in the Au-Rh and Au-Ru systems is stronger than Au-Cu; their absolute O_2 binding energy is far less than the vacancy formation energy of the $CeO_2(111)$ surface, which is 2.48 eV in our system. Therefore, there is no mechanism to provide a sufficient concentration of the (Au-Rh)-O* and (Au-Ru)-O* species for CO oxidation. Some caution of this result is appropriate, however, because oxygen spillover from the CeO_2 support to the supported pure Ag[146] and Pt[124] NCs/NPs has been reported. The case of Ag NPs is still controversial, Luches et al. claimed that oxygen spillover cannot occur from the $CeO_2(111)$ surface[147]. For Pt NP, oxygen spillover was reported from the low-coordinated oxygen atom of nanosized CeO_2. Modifying the oxygen binding energy to the NC by increasing the concentration of the oxophilic alloying element or decreasing the vacancy formation energy of the CeO_2 support by reducing the size may facilitate oxygen spillover and subsequent CO oxidation.

The (Au-Cu)/CeO_2 is the only system where both Au-Cu and Cu-Cu sites clearly prefer to bind O_2 more strongly than CO. The binding sites of O_2 and CO are well separated in this system, that is O_2 binds to the alloying atom sites, while CO binds to the Au sites. Benefiting from its ability to separate the CO and O_2 binding sites, the (Au-Cu)/CeO_2 system was selected for analysis of its catalytic activity. Coadsorption of CO and O_2 was tested on the region of Au-Cu interface. As shown in Figure 5.3, the top Au sites are dominated by CO, and O_2 can binds to either bottom Cu-Cu sites or edge Au-Cu sites in a bridge geometry, initiating two possible reaction pathways. These two reaction pathways are denoted as (1) BT: where O_2 binds to the

Cu-Cu sites in a bridge geometry and CO binds to the top layer Au atom; (2) ET: where O_2 binds to the Au-Cu sites in a bridge geometry and CO binds to the top layer Au atom.

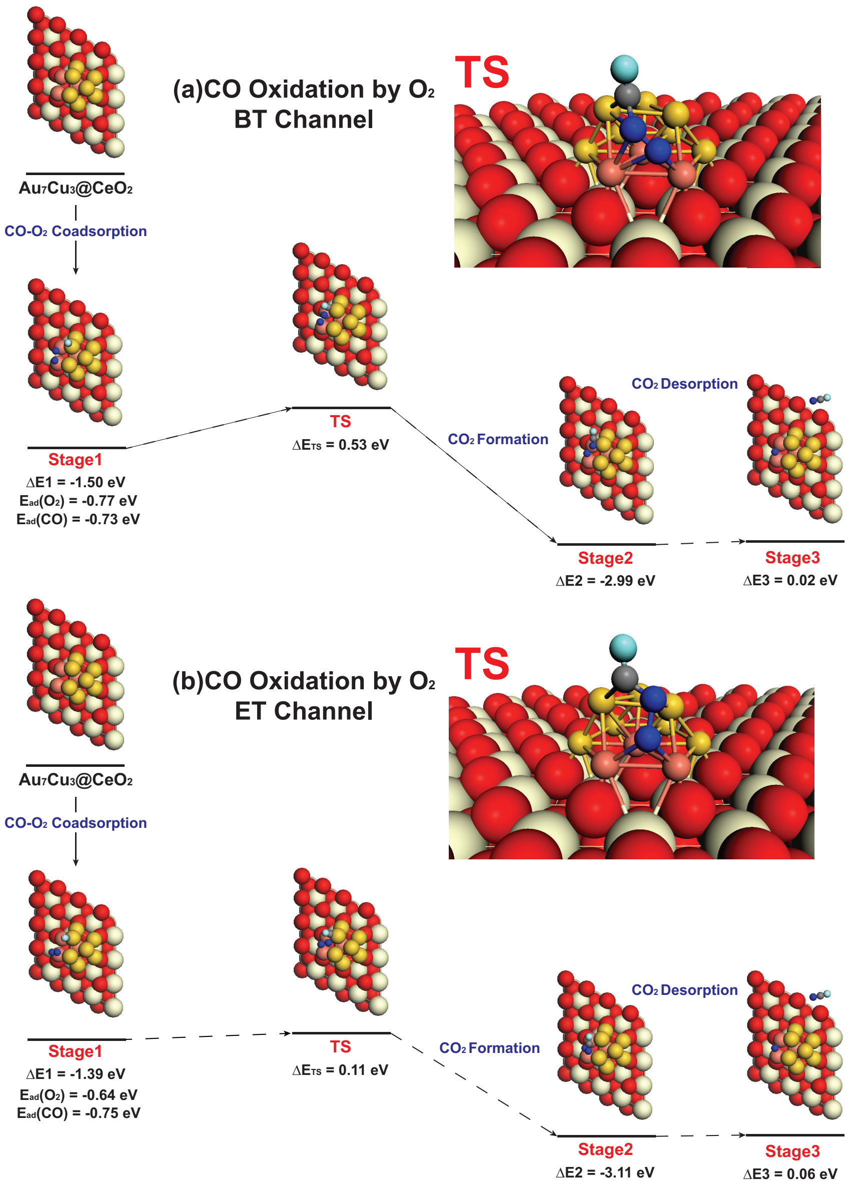

Figure 5.3: Two available initial CO oxidation channels catalyzed by Au_7Cu_3 NC supported on $CeO_2(111)$. The ET channel (b) provides the faster pathway with a lower activation energy (ΔE_{TS}). Ivory, red, blue, gray, and green spheres represents Ce, O (CeO_2), O (O_2), C, and O(CO) atoms, respectively. Au and Cu atoms in the Au_7Cu_3 NC were colored in yellow and copper. ΔE_x is the energy of the xth state relative to the previous stage; for example, ΔE_2 is the energy difference between stage 2 and stage 1.

Figure 5.3 shows the overall energy profiles of two reaction pathways. The coadsorption geometry of both reaction channels is almost equally favored: ΔE_1 (BT) = -1.50 eV and ΔE_1 (ET) = -1.39 eV. Association of coadsorbed CO and O_2, which is the rate-determining step of CO oxidation by the Langmuir-Hinshelwood reaction[120, 148] produces a gas phase CO_2 and a residual Au-O* with an activation energy of 0.53 eV for the BT channel and 0.11 eV for the ET channel. The accessible O_2 adsorption geometry in the ET channel (one of the O atoms of the adsorbed O_2 molecule is close to the Au-CO* species) lowers the activation energy of the first CO oxidation step, making the ET channel the favored CO oxidation pathway.

After the first CO oxidation step, the residual Au-O* oxidized one more CO molecule completing the CO oxidation process. Figure 5.4 shows the energy profile of the second CO oxidation by the Au-O*, which proceeds with an activation barrier of 0.23 eV.

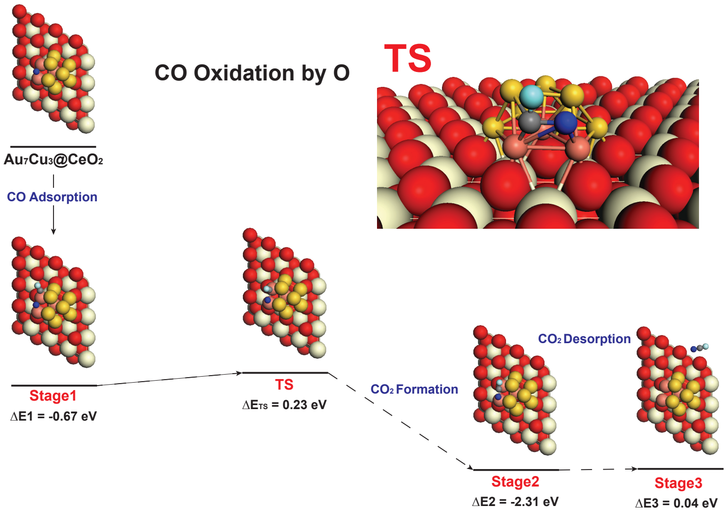

Figure 5.4: . Reaction pathway of the CO oxidation by the residual O* atom.

We have reported atomic oxygen on the Au NCs/NPs as a highly reactive species[120]. In the case of the Au-Cu bimetallic NC however, additional stabilizing effect from the oxophilic Cu atoms likely attributes to the increased barrier of CO oxidation by the Au-O* binding energy. We speculate that this barrier would increase as a function of the Cu concentration in the Au-Cu bimetallic NP. At higher Cu concentrations, oxygen atoms would oxidize Cu atoms converting them to Cu_2O or CuO_2 deactivating the CO oxidation mechanism reported here.

The rate of CO oxidation by the (Au-Cu)/CeO_2 catalyst was estimated with a microkinetic analysis[120, 148] and presented in Table 5.3 . Remarkably, the rate of CO oxidation of the (Au-Cu)/CeO_2 catalyst (ET pathway) is five orders of magnitude faster than the rate of CO oxidation by the Au NC

Table 5.3: Microkinetic analysis of the CO oxidation mechanism involving CO and O_2 coadsorbed on the (Au-Cu) NC of the (Au-Cu)/CeO_2 catalyst

	overall barrier (eV)	rate(s^{-1})
Au/CeO_2	0.14	7.0×10^3
(Au-Cu)/CeO_2-BT	0.53	1.2×10^3
(Au-Cu)/CeO_2-ET	0.23	1.4×10^8

of the Au/CeO_2 system reported in our previous study[120]. Under realistic conditions, such a high reactivity is likely not possible do to mass transport limitations, but the microkinetic model clearly indicates a higher activity for the bimetallic nanoparticle. While the difference in the overall activation barriers reported in the Au/CeO_2 (0.14 eV) and (Au-Cu)/CeO_2 (0.23 eV) catalysts is small, it is the distinct binding sites for the reactions in the (Au-Cu)/CeO_2 catalyst which leads to its high predicted activity.

Chapter 6

Distributed Replica Dynamics

6.1 Abstract

In this paper, we propose a distributed replica dynamics (DRD) method which utilizes distributed computing resources for molecular dynamics simulations of rare-event. Similar to Voter's parallel replica dynamics (PRD) method[149], the dynamics of independent replicas of the system are calculated on independent computational clients. In DRD, each replica ran fixed length of dynamics and then reported back to the server. Simulation clock on the server keeps on accumulating simulation time of each returned replica until the first repots transition. DRD is better compiled with the distributed computing architecture for free of synchronizing replicas. Using the uniqueness theorem and numerical simulation, We prove that DRD method is able to reproduce the original probability distribution of escaping time. Molecular dynamics simulation of Al(100) adatom diffusion using PRD and DRD give nearly the same exponential distribution and average value of escaping time. Guidelines for choosing the number and simulation time of the replications for the DRD method to run efficiently are provided.

6.2 Introduction

One of the most critical challenge in the molecular dynamics (MD) simulation is to overcome the enormous gap between the time scales of the atomic vibrational motion and the duration between transition events. This gap may be as large as several orders of magnitude. The time scale of atomic vibration in solid-state system is typically on the oder of fs (10^{-15} s). However, many interesting structural transitions, *e.g.* vacancy or adsorbate diffusion, film growth or island ripening, surface catalyzed bond breaking or bond formation and so on, are slower than the order of μs (10^{-6} s). In the past decade, remarkable advances have been made in the distributed computing technology as well as the network of massively distributed computing resource, offering a promising solution to bridge the above gap in MD simulation of the "rare event".

Several accelerating MD method have been developed by Voter to overcome the time scale limit of MD simulation, such as PRD, hyperdynamics (HD), and temperature accelerated dynamics (TAD)[149, 150, 151, 152, 153]. In PRD, a set of replicas of the current state are decorrelated to be independent of each other and then start simultaneously. Once the first transition is detected among these replicas, master node will be noticed to stop simulation on all the replicas. The total simulation clock is advanced by the sum of simulation time on all the replicas. HD applies a bias potential to the original potential energy surface to reduce the duration time in the basin. The bias potential is formulated to be zero at the transition ridges. The transition time is then corrected according to the transition state theory. TAD enhances the simulation by running dynamics at a high temperature, and then employ the harmonic transition-state theory to extrapolated the transition time at low temperature.

Among various of methods, PRD is the simplest method requires the least approximation and no information in advance about the transition channels. The PRD method nicely fits for the parallel architecture using a message passing interface with high parallel efficiency and can be easily combined with other accelerating MD methods. However, Voter's implement of PRD is hard to compile with distributed computing environment (DCE) due to the difficulty of synchronizing all the replicas to simultaneously start and stop. In this paper, we propose a new algorithm, DRD method, which is deigned for accelerating MD simulation based on DCE. Similar to PRD method method, the current configuration of system is replicated on multiple clients and then decorrelated. However each client runs for a fixed length of trajectory and reports back to the server when the assigned simulation task is done. Our scheme has no requirement on the synchronization and communication between replicas, thus, well matches the criteria of DCE.

6.3 Method

Following the framework of Voter[149], we consider a classic, canonical system consisted of N atoms evolving on the $3N$-dimensional potential energy surface. Escaping from one state is a first-order process, in other words, the probability of a successful crossing per unit time is a constant, which defined as the rate constant k. Thus the probability distribution of waiting time in the state is given by

$$p(t) = k \exp{(-kt)}. \tag{6.1}$$

The procedure of the DRD method are described as follows:

Step 1 The current configuration of the system is optimized for transition check, then replicated and sent to M independent clients in the DCE.

Step 2 On each client, independent initial momentum is randomly generated according to the Maxwell-Boltzmann distribution at desired simulation temperature. After that, Δt_{dph} is performed to decorrelate the replicated trajectories from each other. During this Δt_{dph} all transition attempts will be reflected.

Step 3 Regular molecular dynamics trajectory with length of t_{rep} is integrated on each client. State check will be performed by every Δt_{blk}. On each single client, if any transition is found, additional Δt_{cor} will be performed to prevent any miss of correlating events; otherwise the program on this client will run till t_{rep} is reached. Information about whether a transition is found, transition time and new state configuration will be recorded and sent back to the server.

Step 4 On the server side, returned data packs from clients will be registered chronologically. As illustrated in Fig. 6.1, the simulation clock will be accumulated by t_{rep} if no transition is found until the first transition is reported with transition time t_1 from replica i. The simulation clock is then advanced by $t_1 + \Delta t_{\text{cor}}$. The product configuration from replica i is then chosen as the new state.

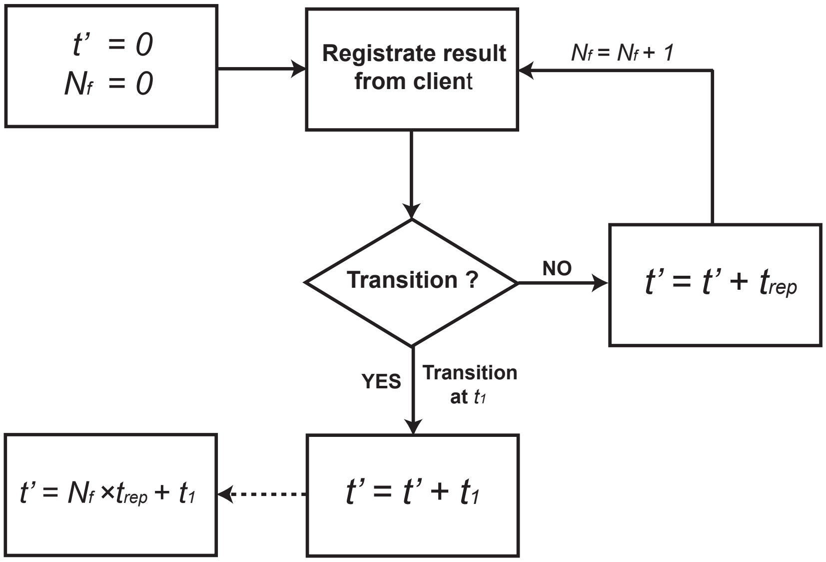

Figure 6.1: Flowchart shows how simulation clock is accumulated at the server in the DRD method.

Once a new state is found, repeat **Steps 1-4**. Assume that before the first transition event is reported, there are N_f replicas registered on the server which failed to detect a transition event in the t_{rep} simulation. The total simulation time of transition to the new state is

$$t' = N_f t_{\text{rep}} + t_1. \tag{6.2}$$

In order to prove the validation of the above DRD scheme, we use the concept of the moment generating function (MGF) and the uniqueness theorem (UT). The MGF of a random valuable X is defined as

$$M_X(m) = E\left[e^{mX}\right], m \in \mathbb{R}, \tag{6.3}$$

where $E[\cdots]$ represents the expectation value.

The **Uniqueness Theorem** states that *suppose that random variables* X *and* Y *have MGF given by* $M_X(m)$ *and* $M_Y(m)$ *respectively. If* $M_X(m) = M_Y(m)$ *for all values of* m *, then* X *and* Y *have the same probability distribution*[154].

Assume an event of which the escaping time t follows the probability distribution given by Eq. 6.1, and t' is collected using our DRD method, it can be proven that the MGF of t' and t is the same

$$M_t(m) = M_{t'}(m) = \frac{k}{k-m}. \tag{6.4}$$

Thus, according to the UT, the probability distribution of t' and t are identical at all point and the dynamics simulated by our scheme is correct. Derivations of the DRD and PRD MGFs are shown in the Appendix.

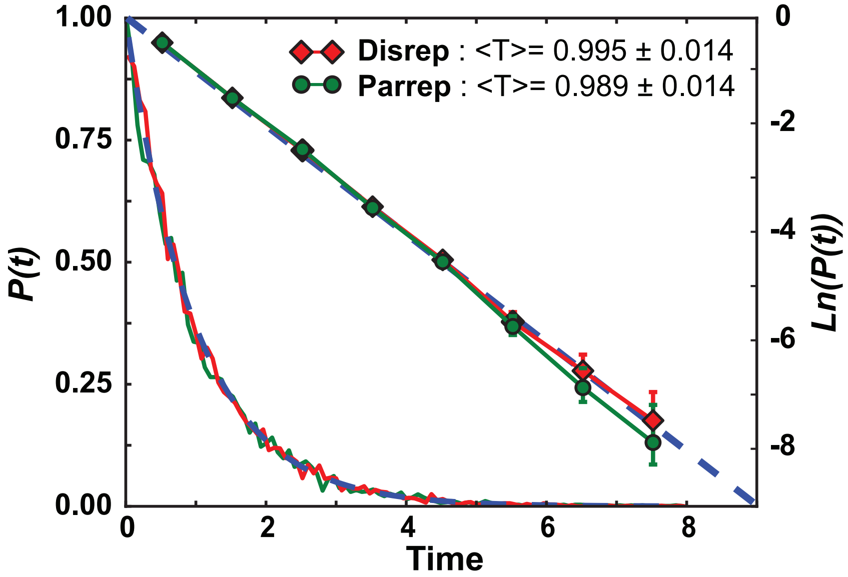

Figure 6.2: The probability distribution function of the escaping time counted by DRD (green) and PRD (red) with ten thousand samples. The blue line in the figure is the original exponential distribution from where random numbers were generated with a rate parameter $k = 1.0$

6.4 Results

6.4.1 Numerical Simulation

Fig. 6.2 shows the numerical simulation results of the probability distribution of the escaping time using DRD and PRD. For each replica, instead of running dynamics of a real physics system, we generated a random number t_i from exponential distribution with rate parameter $k = 1/\langle T_{\text{esp}} \rangle$ as the pseudo-escaping time of a single trajectory. $\langle T_{\text{esp}} \rangle$ is the average escaping time, and was chosen to be 1.0 in the numerical simulation. Distribution of transition time collected by DRD and PRD are compared with the original exponential distribution. In the simulation using DRD, random numbers $\{t_i\}$ were generated one by one until the first transition is detected within a pre-chosen simulation length $t_{\text{rep}} = 0.1$ (first $t_i <= t_{\text{rep}}$). For each generated random number, simulation clock of a single sample was accumulated by $\min\{t_i, t_{\text{rep}}\}$. In PRD, $N_{\text{rep}} = 20$ random number were generated (represents N replicas), the minima in these N_{rep} random numbers times N_{rep} is recorded as the escaping time a single sample. As shown in Fig. 6.2 the red and green solid lines represents DRD and PRD respectively, while the blue dash line is the original exponential distribution where random numbers are generated with $k = 1.0$. The probability distribution of escaping time collected by both DRD and PRD reproduce the original exponential distribution within an acceptable variance.

6.4.2 Adatom Hopping on Al(100)

To demonstrate our method, we simulated the adatom diffusion on the Al(100) surface at $T = 225\ K$. The aluminum interaction was described by an embedded-atom potential developed by Voter. The system was molded as six layers (10×10) with the bottom two layers frozen. Langevin-Verlet algorithm was adapted to integrate the dynamics of the system with a time step of 1.0 fs and a Langevin coupling constant of 0.01 fs^{-1}. Simulation was distributed to 150 clients using the EON and BOINC. Each DRD trajectory ran for 100 ps and reported back to server no matter whether a transition event was detected. Δt_{dph} and Δt_{cor} were both set to 1 ps. Each trajectory was thermalized to 225 K and then Δt_{dph} dynamics was performed during which any transition was rejected.

Every Δt_{blk} of 2.0 ps, a state check was performed to see whether the system entered in a new state by examining whether it belongs to the same reactant basin as the initial state. Once a transition was detected at t_1, the configuration at the time $t_1 + \Delta t_{\mathrm{cor}}$ would be passed back to server when the assigned task was accomplished.

To check the validity of our method, we ran a PRD simulation on the same system with 50 replicas and the same settings as the above DRD simulation. Five hundred events were simulated using both DRD and PRD. The probability distributions of escape time of these events are shown in Fig. 6.3. DRD produces nearly the same exponential distribution of escape time and average escape time as PRD ($\langle T_{\mathrm{esp}}^{DRD} \rangle = 2.07 \pm 0.09$ ns, $\langle T_{\mathrm{esp}}^{\mathrm{PRD}} \rangle = 2.19 \pm 0.09$ ns)

6.4.3 Efficiency of DRD

The efficiency of DRD is dependent on the server job launching strategy. Here is the strategy we used: every time a bundle of N_{rep} jobs is distributed from server to clients. If no transition is found in this bundle of jobs, another bundle of N_{rep} jobs is then distributed until the first detected event. This simple strategy is not necessarily the best, but gives us an opportunity to get a basic idea of relationship between efficiency and the choose of N_{rep}, N_{rep}. Assuming N_{rep} replicas are used, for each replica dephasing time is Δt_{dph}. In order to simplify the discussion, we scale all the time in this section in unit of average transition time $\langle T_{\mathrm{esp}} \rangle$, in other word, $\langle T_{\mathrm{esp}} \rangle = 1$. Efficiency is defined as the ratio of average force calls needed by single trajectory and DRD to have

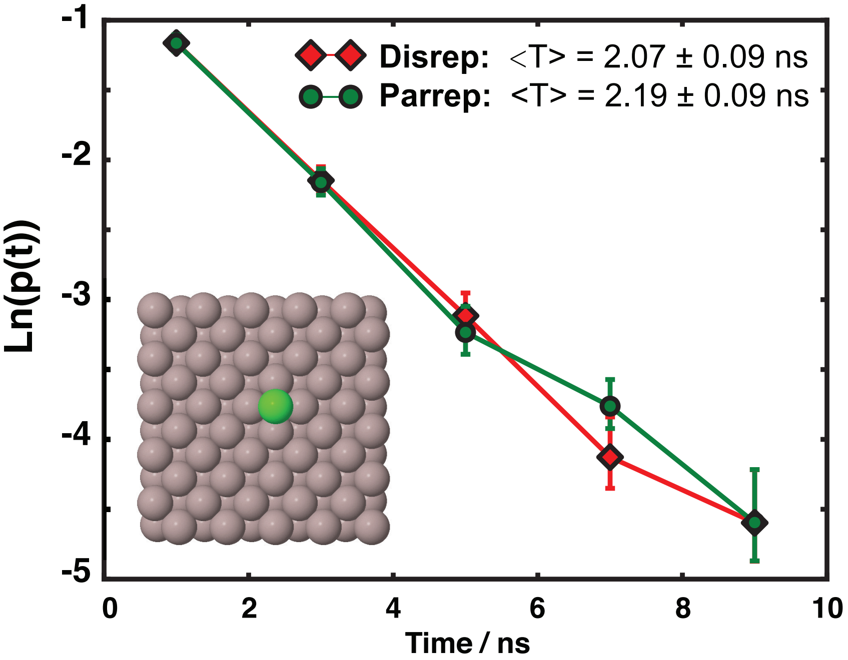

Figure 6.3: Probability distribution of transition time for adatom hopping on Al(100). Red line shows the distribution from DRD simulation while green line is obtained from the simulation using Voter's PRD method. The inset shows a top view of our model for Al(100) surface, with adatom highlighted in green.

one transition. Given the same time step and force call per step, the efficiency can be expressed as

$$E_f = \frac{\langle T_{\text{esp}} \rangle}{\langle N_{\text{fcs}} \rangle} = \frac{1}{\langle N_{\text{fcs}} \rangle}, \tag{6.5}$$

while $\langle N_{\text{fcs}} \rangle$ is given by

$$\langle N_{\text{fcs}} \rangle = (t_{\text{rep}} + \Delta t_{\text{dph}}) N_{\text{bun}} N_{\text{rep}}, \tag{6.6}$$

where

$$N_{\text{bun}} = \begin{cases} 1 & 0 < t < t_{\text{cut}} \\ \cdots & \\ i & (i-1)N_{\text{rep}}t_{\text{rep}} < t < iN_{\text{rep}}t_{\text{rep}}) \end{cases}$$

Set $u = N_{\text{rep}}t_{\text{rep}}$ and $v = N_{\text{rep}}\Delta t_{dph}$, the expectation value of N_{bun} is

$$\langle N_{\text{bun}} \rangle = \frac{1}{1 - e^{-u}} \tag{6.7}$$

Detailed derivation of $\langle N_{\text{bun}} \rangle$ can be found in the Appendix. Pulling $\langle N_{\text{bun}} \rangle$ back to Eq. 6.6, efficiency is then given as follow:

$$E_f = \frac{1 - e^{-u}}{u + v} \tag{6.8}$$

For long-time simulations we except DRD to work on usually have a time scale of μs or more, and Δt_{dph} of ∼ps. Giving this condition, *i.e.* $\Delta t_{\text{dph}} \cong 10^{-6}$ s, Fig. 6.4 shows the efficiency contour as a function of N_{rep} and t_{rep}. Generally, with the same t_{rep}, efficiency decays with the increase of N_{rep}. As long as $N_{\text{rep}}t_{\text{rep}} < 1$, an efficiency over 75% can be approached. For instance, to simulate a 1μs long event, a chose of $\Delta t_{\text{dph}} = 1$ ps, $\Delta t_{\text{rep}} = 100$ ps and $N_{\text{rep}} = 1000$ can give an efficiency around 80%.

6.5 Conclusion

In conclusion, we proved that our DRD produces correct dynamics as Voter's PRD. As discussed above, high efficiency can be achieved with an appropriate choose of N_{rep} and t_{rep} for long-time MD simulation. The efficiency can be further improved if redundant events can be recycled. DRD

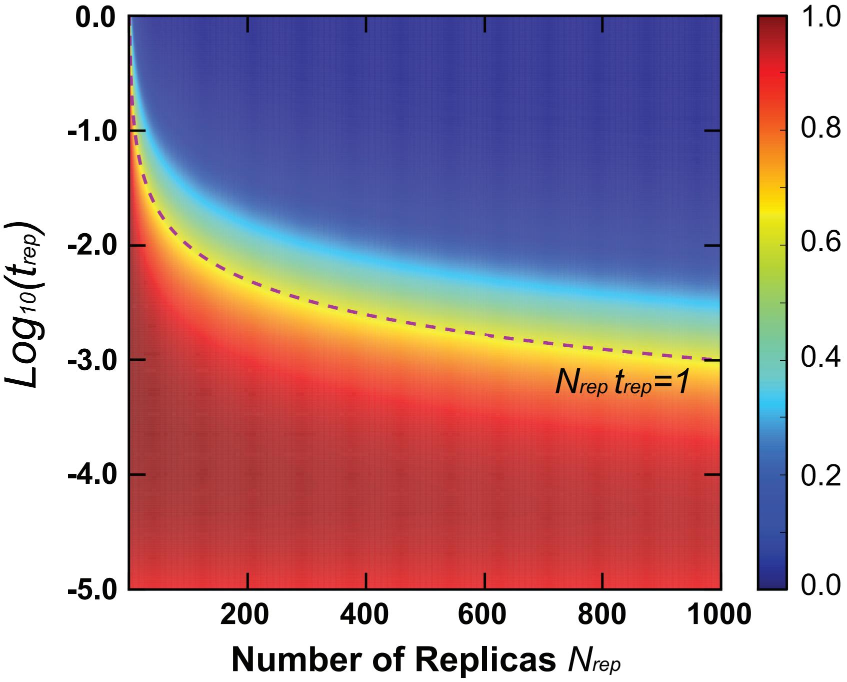

Figure 6.4: Efficiency contour as a function of $N_{\rm rep}$ and $t_{\rm rep}$ described by Eq. 6.8 with $\Delta t_{\rm dph} \cong 10^{-6}$ s. The dashed line is for $N_{\rm rep}t_{\rm rep} = 1$

offers a mean to efficiently utilize enormous distributed computing resources to accelerate long-time MD simulation.

6.6 Appendix

6.6.1 MGF of an exponential distribution

A classical, canonical system of N atoms vibrating in a basin of the $3N$-dimensional potential energy surface with the assumption that dynamical exploration of this basin is ergodic. Escaping from one state is a first-order process with rate constant of k, the probability distribution function of escaping time is given by Eq. 6.1.

$$p(t) = k \exp(-kt).$$

The MGF of the above exponential distribution of waiting time t can be obtained as

$$\begin{aligned} M_t(m) &= \int_0^{+\infty} e^{mt} k e^{-kt} \mathrm{d}t \\ &= \frac{k}{k-m}. \end{aligned} \tag{A6.6.1}$$

6.6.2 MGF of t' for DRD

In DRD, the current configuration of the system is replicated to clients to run a fixed length of trajectory t_{rep}. The the first replica reports back with a successful transition at t_1. Before that, N_f replicas has been registered on the sever with no event detected. t' is the waiting time counted by DRD,

$$t' = N_f t_{\text{rep}} + t_1.$$

Its MGF is given by

$$M_{t'}(m) = \int_0^{+\infty} e^{mt'} p(t') \mathrm{d}t' \tag{A6.6.2}$$

The probability of failing to find a transition within t_{rep} is $F(t_{\text{rep}})$, where

$$\begin{aligned} F(t_{\text{rep}}) &= 1 - P(t < t_{\text{rep}}) \\ &= 1 - \int_0^{t_{\text{rep}}} k e^{-kt} \mathrm{d}t \\ &= e^{-kt_{\text{rep}}} \end{aligned} \tag{A6.6.3}$$

It is not trivial to write down the general formula of $p(t')$, however $p(t')$ can be treated as the mixed joint probability density function of discrete random variable N_f and continuous random variable t_1.

$$p(t') = P(N_f)p(t_1) \tag{A6.6.4}$$

where $P(N_f)$ is the probability of having N_f replicas registered with no transition, and $p(t_1)$ has the same probability density function as Eq. 6.1 but constrained in the section of $[0, t_{\text{rep}})$. If the probability of having N_f replicas registered with no transition is the same as N_f failed Bernoulli trial with probability of success $F(t_{\text{rep}})$ in each trail. Then $p(t')$ can be expressed in term of N_f and t_1,

$$p(t') = F(t_{\text{rep}})^{N_f} k e^{-kt_1},\ t_1 \in [0, t_{\text{rep}}). \tag{A6.6.5}$$

Since $N_f$and t_1 are separable, the MGF of t' can be derived,

$$\begin{aligned}
M_{t'}(m) &= \int_0^{+\infty} e^{mt'} p(t')\mathrm{d}t' \\
&= \sum_{N_f=0} \int_0^{t_{\text{rep}}} e^{m(N_f t_{\text{rep}}+t1)} F(t_{\text{rep}})^{N_f} k e^{-kt_1} \mathrm{d}t_1 \\
&= \sum_{N_f=0} e^{m(N_f t_{\text{rep}})} F(t_{\text{rep}})^{N_f} \int_0^{t_{\text{rep}}} k e^{(m-k)t_1} \mathrm{d}t_1 \\
&= \frac{k}{m-k}[e^{(m-k)t_{\text{rep}}} - 1] \sum_{N_f=0} [e^{mt_{\text{rep}}} F(t_{\text{rep}})]^{N_f} \\
&= \frac{k}{m-k}[e^{(m-k)t_{\text{rep}}} - 1] \frac{1}{1 - e^{mt_{\text{rep}}} e^{-kt_{\text{rep}}}} \\
&= \frac{k}{k-m}.
\end{aligned} \tag{A6.6.6}$$

As we proved above, $M_{t'}(m)$ is independent of t_{rep} and is exactly the same as the $M_t(m)$ shown in Eq A6.6.1, demonstrating that the distribution of transition times in DRD is identical as the original one.

6.6.3 Derivation of $\langle N_{\text{bun}} \rangle$

As we discussed in Section IIIB,

$$N_{\text{bun}} = \begin{cases} 1 & 0 < t < t_{\text{cut}} \\ \dots & \\ i & (i-1)N_{\text{rep}}t_{\text{rep}} < t < iN_{\text{rep}}t_{\text{rep}}) \end{cases}$$

expectation of N_{bun} is given by

$$\begin{aligned} \langle N_{\text{bun}} \rangle &= \sum_{i=1}^{\infty} iPr[(i-1)N_{\text{rep}}t_{\text{rep}} < t < iN_{\text{rep}}t_{\text{rep}}] \\ &= (e^{N_{\text{rep}}t_{\text{rep}}} - 1) \sum_{i=1}^{\infty} ie^{-iN_{\text{rep}}t_{\text{rep}}} \end{aligned} \tag{A6.6.7}$$

set $u = N_{\text{rep}}t_{\text{rep}}$,

$$\begin{aligned} \langle N_{\text{bun}} \rangle &= (e^u - 1) \sum_{i=1}^{\infty} ie^{-ui} \\ &= \frac{1}{1 - e^{-u}} \end{aligned} \tag{A6.6.8}$$

Bibliography

[1] Li, L.; Larsen, A. H.; Romero, N. A.; Morozov, V. A.; Glinsvad, C.; Abild-Pedersen, F.; Greeley, J.; Jacobsen, K. W.; Nørskov, J. K. *J. Phys. Chem. Lett.* **2013**, *4*, 222–226.

[2] Nørskov, J. K.; Rossmeisl, J.; Logadottir, A.; Lindqvist, L.; Kitchin, J. R.; Bligaard, T.; Jónsson, H. *J. Phys. Chem. B* **2004**, *108*, 17886–17892.

[3] Groß, A. *J. Phys.: Conden. Matter* **2009**, *21*, 84205.

[4] Groß, A. *Top. Catal.* **2006**, *37*, 29–39.

[5] Nørskov, J. K.; Bligaard, T.; Rossmeisl, J.; Christensen, C. H. *Nat. Chem.* **2009**, *1*, 37–46.

[6] Bligaard, T.; Nørskov, J.; Dahl, S.; Matthiesen, J.; Christensen, C.; Sehested, J. *J. Catal.* **2004**, *224*, 206–217.

[7] Nørskov, J. K.; Abild-Pedersen, F.; Studt, F.; Bligaard, T. *Proc. Natl. Acad. Sci.* **2011**, *108*, 937–943.

[8] Abild-Pedersen, F.; Greeley, J.; Studt, F.; Rossmeisl, J.; Munter, T. R.; Moses, P. G.; Skúlason, E.; Bligaard, T.; Nørskov, J. K. *Phys. Rev. Lett.* **2007**, *99*, 016105.

[9] Fernández, E. M.; Moses, P. G.; Toftelund, A.; Hansen, H. A.; Martínez, J. I.; Abild-Pedersen, F.; Kleis, J.; Hinnemann, B.; Rossmeisl, J.; Bligaard, T.; Nørskov, J. K. *Angew. Chem. Int. Ed.* **2008**, *47*, 4683–4686.

[10] Falsig, H.; Hvolbæk, B.; Kristensen, I. S.; Jiang, T.; Bligaard, T.; Christensen, C. H.; Nørskov, J. K. *Angew. Chem. Int. Ed.* **2008**, *47*, 4835–4839.

[11] Xu, Y.; Lausche, A. C.; Wang, S.; Khan, T. S.; Abild-Pedersen, F.; Studt, F.; Nørskov, J. K.; Bligaard, T. *New J. Phys.* **2013**, *15*, 125021.

[12] Lausche, A. C.; Medford, A. J.; Khan, T. S.; Xu, Y.; Bligaard, T.; Abild-Pedersen, F.; Nørskov, J. K.; Studt, F. *J. Catal.* **2013**, *307*, 275–282.

[13] Yoo, J. S.; Abild-Pedersen, F.; Nørskov, J. K.; Studt, F. *ACS Catal.* **2014**, *4*, 1226–1233.

[14] Hammer, B.; Nørskov, J. K. *Adv. Catal.* **2000**, *45*, 71–129.

[15] Hammer, B.; Nørskov, J. K. *Surf. Sci.* **1995**, *343*, 211–220.

[16] Ruban, A.; Hammer, B.; Stoltze, P.; Skriver, H. L.; Nørskov, J. K. *J. Mol. Catal. A: Chem.* **1997**, *115*, 421–429.

[17] Xu, Y.; Ruban, A. V.; Mavrikakis, M. *J. Am. Chem. Soc.* **2004**, *126*, 4717–4725.

[18] Tang, W.; Henkelman, G. *J. Chem. Phys.* **2009**, *130*, 194504.

[19] Kitchin, J.; Nørskov, J. K.; Barteau, M. A.; Chen, J. G. *J. Chem. Phys.* **2004**, *120*, 10240–10246.

[20] Yamamoto, D.; Watanabe, S.; Miyahara, M. T. *Langmuir* **2010**, *26*, 2339–2345.

[21] Scott, R. W. J.; Wilson, O. M.; Crooks, R. M. *J. Phys. Chem. B* **2005**, *109*, 692–704.

[22] Lang, H.; May, R. A.; Iversen, B. L.; Chandler, B. D. *J. Am. Chem. Soc.* **2003**, *125*, 14832–14836.

[23] Bernechea, M.; García-Rodríguez, S.; Terreros, P.; de Jesús, E.; Fierro, J. L. G.; Rojas, S. *J. Phys. Chem. C* **2011**, *115*, 1287–1294.

[24] Ye, H.; Crooks, J. A.; Crooks, R. M. *Langmuir* **2007**, *23*, 11901–11906.

[25] Ye, H.; Crooks, R. M. *J. Am. Chem. Soc.* **2007**, *129*, 3627–3633.

[26] Ye, H.; Crooks, R. M. *J. Am. Chem. Soc.* **2005**, *127*, 4930–4934.

[27] Crooks, R. M.; Zhao, M.; Sun, L.; Chechik, V.; Yeung, L. K. *Acc. Chem. Res.* **2001**, *34*, 181–190.

[28] Carino, E. V.; Crooks, R. M. *Langmuir* **2011**, *27*, 4227–4235.

[29] Yancey, D. F.; Carino, E. V.; Crooks, R. M. *J. Am. Chem. Soc.* **2010**, *132*, 10988–10989.

[30] Yancey, D. F.; Zhang, L.; Crooks, R. M.; Henkelman, G. *Chem. Sci.* **2012**, *3*, 1033–1040.

[31] Anderson, R. M.; Zhang, L.; Loussaert, J. A.; Frenkel, A. I.; Henkelman, G.; Crooks, R. M. *ACS Nano* **2013**, *7*, 9345–9353.

[32] Wilson, O. M.; Scott, R. W. J.; Garcia-Martinez, J. C.; Crooks, R. M. *J. Am. Chem. Soc.* **2005**, *127*, 1015–1024.

[33] Knecht, M. R.; Weir, M. G.; Frenkel, A. I.; Crooks, R. M. *Chem. Mat.* **2008**, *20*, 1019–1028.

[34] Weir, M. G.; Knecht, M. R.; Frenkel, A. I.; Crooks, R. M. *Langmuir* **2010**, *26*, 1137–1146.

[35] Myers, S. V.; Frenkel, A. I.; Crooks, R. M. *Chem. Mat.* **2009**, *21*, 4824–4829.

[36] Zhang, L.; Iyyamperumal, R.; Yancey, D. F.; Crooks, R. M.; Henkelman, G. *ACS Nano* **2013**, *7*, 9168–9172.

[37] Hernández, J.; Solla-Gullón, J.; Herrero, E.; Aldaz, A.; Feliu, J. M. *J. Phys. Chem. B* **2005**, *109*, 12651–12654.

[38] Hernández, J.; Solla-Gullón, J.; Herrero, E.; Aldaz, A.; Feliu, J. M. *J. Phys. Chem. C* **2007**, *111*, 14078–14083.

[39] Hernández, J.; Solla-Gullón, J.; Herrero, E.; Feliu, J. M.; Aldaz, A. *J. Nanosci. Nanotechnol.* **2009**, *9*, 2256–2273.

[40] Froemming, N. S.; Henkelman, G. *J. Chem. Phys* **2009**, *131*, 234103.

[41] Wang, J. X.; Inada, H.; Wu, L.; Zhu, Y.; Choi, Y.; Liu, P.; Zhou, W.-P.; Adzic, R. R. *J. Am. Chem. Soc.* **2009**, *131*, 17298–17302.

[42] Gong, K.; Su, D.; Adzic, R. R. *J. Am. Chem. Soc.* **2010**, *132*, 14364–14366.

[43] Pande, S.; Ghosh, S. K.; Praharaj, S.; Panigrahi, S.; Basu, S.; Jana, S.; Pal, A.; Tsukuda, T.; Pal, T. *J. Phys. Chem. C* **2007**, *111*, 10806–10813.

[44] Fang, P.-P.; Duan, S.; Lin, X.-D.; Anema, J. R.; Li, J.-F.; Buriez, O.; Ding, Y.; Fan, F.-R.; Wu, D.-Y.; Ren, B.; Wang, Z. L.; Amatore, C.; Tian, Z.-Q. *Chem. Sci.* **2011**, *2*, 531–539.

[45] Nilekar, A. U.; Xu, Y.; Zhang, J.; Vukmirovic, M.; Sasaki, K.; Adzic, R.; Mavrikakis, M. *Top. Catal.* **2007**, *46*, 276–284.

[46] Barcaro, G.; Fortunelli, A.; Polak, M.; Rubinovich, L. *Nano Lett.* **2011**, *11*, 1766–1769.

[47] Lai, F.-J.; Chou, H.-L.; Sarma, L. S.; Wang, D.-Y.; Lin, Y.-C.; Lee, J.-F.; Hwang, B.-J.; Chen, C.-C. *Nanoscale* **2010**, *2*, 573–581.

[48] Weber, M.; Wang, J.; Wasmus, S.; Savinell, R. F. *J. Electrochem. Soc.* **1996**, *143*, L158–L160.

[49] Capon, A.; Parson, R. *J. electroanal. chem. interfacial electrochem.* **1973**, *44*, 1 – 7.

[50] Zhang, S.; Shao, Y.; Liao, H.-g.; Liu, J.; Aksay, I. A.; Yin, G.; Lin, Y. *Chem. Mat.* **2011**, *23*, 1079–1081.

[51] Park, I.-S.; Lee, K.-S.; Choi, J.-H.; Park, H.-Y.; Sung, Y.-E. *J. Phys. Chem. C* **2007**, *111*, 19126–19133.

[52] Kristian, N.; Yan, Y.; Wang, X. *Chem. Commun.* **2008**, 353–355.

[53] Zhang, G.-R.; Zhao, D.; Feng, Y.-Y.; Zhang, B.; Su, D. S.; Liu, G.; Xu, B.-Q. *ACS Nano* **2012**, *6*, 2226–2236.

[54] Rice, C.; Ha, S.; Masel, R.; Waszczuk, P.; Wieckowski, A.; Barnard, T. *J. Power Sources* **2002**, *111*, 83 – 89.

[55] Yu, X.; Pickup, P. G. *Electrochem. Commun.* **2009**, *11*, 2012 – 2014.

[56] Zhang, J.; Mo, Y.; Vukmirovic, M. B.; Klie, R.; Sasaki, K.; Adzic, R. R. *J. Phys. Chem. B* **2004**, *108*, 10955–10964.

[57] Tessier, B. C.; Russell, A. E.; Theobald, B. R.; Thompsett, D. *ECS Trans.* **2009**, *16*, 1–11.

[58] Sanchez, S. I.; Small, M. W.; Zuo, J.-m.; Nuzzo, R. G. *J. Am. Chem. Soc.* **2009**, *131*, 8683–8689.

[59] Wang, Y.; Toshima, N. *J. Phys. Chem. B* **1997**, *101*, 5301–5306.

[60] Li, G.; Lu, W.; Luo, Y.; Xia, M.; Chai, C.; Wang, X. *Chin. J. Chem.* **2012**, *30*, 541–546.

[61] Taufany, F.; Pan, C.-J.; Rick, J.; Chou, H.-L.; Tsai, M.-C.; Hwang, B.-J.; Liu, D.-G.; Lee, J.-F.; Tang, M.-T.; Lee, Y.-C.; Chen, C.-I. *ACS Nano* **2011**, *5*, 9370–9381.

[62] Frenkel, A. I.; Wang, Q.; Sanchez, S. I.; Small, M. W.; Nuzzo, R. G. *J. Chem. Phys* **2013**, *138*, –.

[63] Kresse, G. *Phys. Rev. B* **2000**, *62*, 8295–8305.

[64] Kresse, G.; Hafner, J. *Surf. Sci.* **2000**, *459*, 287–302.

[65] Perdew, J. P.; Wang, Y. *Phys. Rev. B* **1992**, *45*, 13244–13249.

[66] Blöchl, P. E. *Phys. Rev. B* **1994**, *50*, 17953.

[67] Kresse, G.; Joubert, D. *Phys. Rev. B* **1999**, *59*, 1758.

[68] Zhang, J.; Vukmirovic, M. B.; Xu, Y.; Mavrikakis, M.; Adzic, R. R. *Angew. Chem. Int. Ed.* **2005**, *44*, 2132–2135.

[69] Lima, F. H. B.; Zhang, J.; Shao, M. H.; Sasaki, K.; Vukmirovic, M. B.; Ticianelli, E. A.; Adzic, R. R. *J. Phys. Chem. C* **2007**, *111*, 404–410.

[70] Adzic, R.; Zhang, J.; Sasaki, K.; Vukmirovic, M.; Shao, M.; Wang, J.; Nilekar, A.; Mavrikakis, M.; Valerio, J.; Uribe, F. *Top. Catal.* **2007**, *46*, 249–262.

[71] Kanan, M. W.; Nocera, D. G. *Science* **2008**, *321*, 1072–1075.

[72] Rhee, C. K.; Kim, B.-J.; Ham, C.; Kim, Y.-J.; Song, K.; Kwon, K. *Langmuir* **2009**, *25*, 7140–7147.

[73] Maciá, M. D.; Herrero, E.; Feliu, J. M. *Electrochim. Acta* **2002**, *47*, 3653 – 3661.

[74] Friedrich, K.; Henglein, F.; Stimming, U.; Unkauf, W. *Electrochim. Acta* **2000**, *45*, 3283 – 3293.

[75] Frenkel, A. I. *Chem. Soc. Rev.* **2012**, *41*, 8163–8178.

[76] Shao, M. H.; Sasaki, K.; Adzic, R. *J. Am. Chem. Soc.* **2006**, *128*, 3526–3527.

[77] Shao, M. H.; Huang, T.; Liu, P.; Zhang, J.; Sasaki, K.; Vukmirovic, M. B.; Adzic, R. R. *Langmuir* **2006**, *22*, 10409–10415.

[78] Fernández, J. L.; Walsh, D. A.; Bard, A. J. *J. Am. Chem. Soc.* **2005**, *127*, 357–365.

[79] Stamenkovic, V. R.; Fowler, B.; Mun, B. S.; Wang, G.; Ross, P. N.; Lucas, C. A.; Marković, N. M. *Science* **2007**, *315*, 493–497.

[80] Koh, S.; Strasser, P. *J. Am. Chem. Soc.* **2007**, *129*, 12624–12625.

[81] Savadogo, O.; Lee, K.; Oishi, K.; Mitsushima, S.; Kamiya, N.; Ota, K.-I. *Electrochem. Comm.* **2004**, *6*, 105–109.

[82] Brönsted, J. N. *Chem. Rev.* **1928**, *5*, 231–338.

[83] Evans, M. G.; Polanyi, N. P. *Trans. Faraday Soc.* **1938**, *34*, 11.

[84] Wang, X.; Kariuki, N.; Vaughey, J. T.; Goodpaster, J.; Kumar, R.; Myers, D. J. *J. Electrochem. Soc* **2008**, *155*, B602–B609.

[85] Fouda-Onana, F.; Bah, S.; Savadogo, O. *J. Electroanal. Chem.* **2009**, *636*, 1–9.

[86] Bader, R. F. W. *Atoms in Molecules: A Quantum Theory*; Oxford University Press: New York, 1990.

[87] Tang, W.; Sanville, E.; Henkelman, G. *J. Phys.: Condens. Matter* **2009**, *21*, 84204.

[88] Ruban, A.; Hammer, B.; Stoltze, P.; Skriver, H. L.; Nørskov, J. K. *J. Mol. Catal. A* **1997**, *115*, 421–429.

[89] Vitos, L.; Ruban, A.; Skriver, H.; Kollár, J. *Surf. Sci.* **1998**, *411*, 186 – 202.

[90] Tkatchenko, A.; Scheffler, M. *Phys. Rev. Lett.* **2009**, *102*, 073005.

[91] Rossmeisl, J.; Qu, Z.-W.; Zhu, H.; Kroes, G.-J.; Nørskov, J. *J. Electroanal. Chem.* **2007**, *607*, 83 – 89, Theoretical and Computational Electrochemistry.

[92] Maroun, F.; Ozanam, F.; Magnussen, O. M.; Behm, R. J. *Science* **2001**, *293*, 1811–1814.

[93] Liu, P.; Norskov, J. K. *Phys. Chem. Chem. Phys.* **2001**, *3*, 3814–3818.

[94] Tang, W.; Zhang, L.; Henkelman, G. *J. Phys. Chem. Lett.* **2011**, *2*, 1328–1331.

[95] Wang, C.; Chi, M.; Li, D.; Strmcnik, D.; van der Vliet, D.; Wang, G.; Komanicky, V.; Chang, K.-C.; Paulikas, A. P.; Tripkovic, D.; Pearson, J.; More, K. L.; Markovic, N. M.; Stamenkovic, V. R. *J. Am. Chem. Soc.* **2011**, *133*, 14396–14403.

[96] Stamenkovic, V. R.; Mun, B. S.; Arenz, M.; Mayrhofers, K. J. J.; Lucas, C. A.; Wang, G.; Ross, P. N.; Marković, N. M. *Nat. Mater.* **2007**, *6*, 241–247.

[97] Stamenkovic, V. R.; Mun, B. S.; Mayrhofer, K. J. J.; Ross, P. N.; Markovic, N. M. *J. Am. Chem. Soc.* **2006**, *128*, 8813–8819.

[98] Stamenkovic, V.; Mun, B. S.; Mayrhofer, K. J.; Ross, P. N.; Markovic, N. M.; Rossmeisl, J.; Greeley, J.; Nørskov, J. K. *Angew. Chem. Int. Ed.* **2006**, *45*, 2897–2901.

[99] Sasaki, K.; Wang, J.; Naohara, H.; Marinkovic, N.; More, K.; Inada, H.; Adzic, R. *Electrochim. Acta.* **2010**, *55*, 2645–2652.

[100] Sasaki, K.; Naohara, H.; Choi, Y.; Cai, Y.; Chen, W.-F.; Liu, P.; Adzic, R. R. *Nat. Commun.* **2012**, *3*, 1115.

[101] Koenigsmann, C.; Sutter, E.; Adzic, R. R.; Wong, S. S. *J. Phys. Chem. C* **2012**, *116*, 15297–15306.

[102] Nørskov, J.; Bligaard, T.; Logadottir, A.; Bahn, S.; Hansen, L.; Bollinger, M.; Bengaard, H.; Hammer, B.; Sljivancanin, Z.; Mavrikakis, M.; Xu, Y.; Dahl, S.; Jacobsen, C. *J. Catal.* **2002**, *209*, 275 – 278.

[103] Hammer, B.; Hansen, L. B.; Nørskov, J. K. *Phys. Rev. B* **1999**, *59*, 7413–7421.

[104] Peterson, A. A.; Grabow, L. C.; Brennan, T. P.; Shong, B.; Ooi, C.; Wu, D. M.; Li, C. W.; Kushwaha, A.; Medford, A. J.; Mbuga, F.; Li, L.; Nørskov, J. K. *Top. Catal.* **2012**, *55*, 1276–1282.

[105] Sigalas, M.; Papaconstantopoulos, D. A.; Bacalis, N. C. *Phys. Rev. B* **1992**, *45*, 5777.

[106] Mason, S. E.; Grinberg, I.; Rappe, A. M. *Phys. Rev. B* **2004**, *69*, 161401.

[107] Zhang, L.; Henkelman, G. *J. Phys. Chem. C* **2012**, *116*, 20860–20865.

[108] Nørskov, J. K.; Bligaard, T.; Logadottir, A.; Kitchin, J. R.; Chen, J. G.; Pandelov, S.; Stimming, U. *J. Electrochem. Soc.* **2005**, *152*, J23–J26.

[109] Parsons, R. *Trans. Faraday Soc.* **1958**, *54*, 1053–1063.

[110] Greeley, J.; Nørskov, J. K.; Kibler, L. A.; El-Aziz, A. M.; Kolb, D. M. *ChemPhysChem* **2006**, *7*, 1032–1035.

[111] Greeley, J.; Jaramillo, T. F.; Bonde, J.; Chorkendorff, I.; Norskov, J. K. *Nat. Mater.* **2006**, *5*, 909–913.

[112] Liu, Z.-P.; Hu, P.; Alavi, A. *J. Am. Chem. Soc.* **2002**, *124*, 14770–14779.

[113] Wang, L.-L.; Johnson, D. D. *J. Am. Chem. Soc.* **2009**, *131*, 14023–14029.

[114] Ferrando, R.; Jellinek, J.; Johnston, R. L. *Chem. Rev.* **2008**, *108*, 845–910.

[115] Ruban, A. V.; Skriver, H. L.; Nørskov, J. K. *Phys. Rev. B* **1999**, *59*, 15990–16000.

[116] Greeley, J.; Mavrikakis, M. *Catal. Today* **2006**, *111*, 52–58.

[117] Yang, J.; Yang, J.; Ying, J. Y. *ACS Nano* **2012**, *6*, 9373–9382.

[118] Cochell, T.; Manthiram, A. *Langmuir* **2012**, *28*, 1579–1587.

[119] Kim, H. Y.; Henkelman, G. *J. Phys. Chem. Lett.* **2012**, *3*, 2194.

[120] Kim, H. Y.; Lee, H. M.; Henkelman, G. *J. Am. Chem. Soc.* **2012**, *134*, 1560.

[121] Rodriguez, J. A.; Ma, S.; Liu, P.; Hrbek, J.; Evans, J.; Perez, M. *Science* **2007**, *318*, 1757.

[122] Green, I. X.; Tang, W. J.; Neurock, M.; Yates, J. T. *Science* **2011**, *333*, 736.

[123] Camellone, M. F.; Fabris, S. *J. Am. Chem. Soc.* **2009**, *131*, 10473.

[124] Vayssilov, G. N.; Lykhach, Y.; Migani, A.; Staudt, T.; Petrova, G. P.; Tsud, N.; Skala, T.; Bruix, A.; Illas, F.; Prince, K. C. *Nat. Mater.* **2011**, *10*, 310.

[125] Carrettin, S.; Concepcion, P.; Corma, A.; Nieto, J. M. L.; Puntes, V. F. *Angew. Chem., Int. Ed.* **2004**, *43*, 2538.

[126] Guzman, J.; Carrettin, S.; Corma, A. *J. Am. Chem. Soc.* **2005**, *127*, 3286.

[127] Bruix, A.; Rodriguez, J. A.; Ramirez, P. J.; Senanayake, S. D.; Evans, J.; Park, J. B.; Stacchiola, D.; Liu, P.; Hrbek, J.; Illas, F. *J. Am. Chem. Soc.* **2012**, *134*, 8968.

[128] Nie, X.; Qian, H.; Ge, Q.; Xu, H.; Jin, R. *ACS Nano* **2012**, *6*, 6014.

[129] López-Haro, M.; Cíes, J. M.; Trasobares, S.; Pérez-Omil, J. A.; Delgado, J. J.; Bernal, S.; Bayle-Guillemaud, P.; Stéphan, O.; Yoshida, K.; Boyes, E. D. *ACS Nano* **2012**, *6*, 6812.

[130] Park, J. B.; Graciani, J.; Evans, J.; Stacchiola, D.; Senanayake, S. D.; Barrio, L.; Liu, P.; Sanz, J. F.; Hrbek, J.; Rodriguez, J. A. *J. Am. Chem. Soc.* **2010**, *132*, 356.

[131] Stamatakis, M.; Christiansen, M. A.; Vlachos, D. G.; Mpourmpakis, G. *Nano Lett.* **2012**, *12*, 3621.

[132] Kim, H. Y.; Henkelman, G. *J. Phys. Chem. Lett.* **2013**, *4*, 216.

[133] Kowal, A.; Li, M.; Shao, M.; Sasaki, K.; Vukmirovic, M. B.; Zhang, J.; Marinkovic, N. S.; Liu, P.; Frenkel, A. I.; Adzic, R. R. *Nat. Mater.* **2009**, *8*, 325.

[134] Zhou, W.-P.; An, W.; Su, D.; Palomino, R.; Liu, P.; White, M. G.; Adzic, R. R. *J. Phys. Chem. Lett.* **2012**, *3*, 3286.

[135] Park, J. B.; Graciani, J.; Evans, J.; Stacchiola, D.; Ma, S. G.; Liu, P.; Nambu, A.; Sanz, J. F.; Hrbek, J.; Rodriguez, J. A. *Proc. Natl. Acad. Sci.* **2009**, *106*, 4975.

[136] Senanayake, S. D.; Stacchiola, D.; Rodriguez, J. A. *Acc. Chem. Res.* **2013**,

[137] Vidal, A. B.; Feria, L.; Evans, J.; Takahashi, Y.; Liu, P.; Nakamura, K.; Illas, F.; Rodriguez, J. A. *J. Phys. Chem. Lett.* **2012**, *3*, 2275.

[138] Stacchiola, D. J.; Senanayake, S. D.; Liu, P.; Rodriguez, J. A. *Chem. Rev.* **2013**, *113*, 4373.

[139] Roldan, A.; Ricart, J. M.; Illas, F.; Pacchioni, G. *Phys. Chem. Chem. Phys.* **2010**, *12*, 10723.

[140] Perdew, J. P.; Burke, K.; Ernzerhof, M. *Phys. Rev. Lett.* **1996**, *77*, 3865.

[141] Dudarev, S. L.; Botton, G. A.; Savrasov, S. Y.; Humphreys, C. J.; Sutton, A. P. *Phys. Rev. B* **1998**, *57*, 1505.

[142] Henkelman, G.; Jonsson, H. *J. Chem. Phys.* **2000**, *113*, 9978.

[143] Henkelman, G.; Uberuaga, B. P.; Jonsson, H. *J. Chem. Phys.* **2000**, *113*, 9901.

[144] Ta, N.; Liu, J.; Chenna, S.; Crozier, P. A.; Li, Y.; Chen, A.; Shen, W. *J. Am. Chem. Soc.* **2012**, *134*, 20585.

[145] Farmer, J. A.; Campbell, C. T. *Science* **2010**, *329*, 933.

[146] Kong, D.; Wang, G.; Pan, Y.; Hu, S.; Hou, J.; Pan, H.; Campbell, C. T.; Zhu, J. *J. Phys. Chem. C* **2011**, *115*, 6715.

[147] Luches, P.; Pagliuca, F.; Valeri, S.; Illas, F.; Preda, G.; Pacchioni, G. *J. Phys. Chem. C* **2011**, *116*, 1122.

[148] Falsig, H.; Hvolbaek, B.; Kristensen, I. S.; Jiang, T.; Bligaard, T.; Christensen, C. H.; Nørskov, J. K. *Angew. Chem., Int. Ed.* **2008**, *47*, 4835.

[149] Voter, A. F. *Phys. Rev. B* **1998**, *57*, R13985–R13988.

[150] Voter, A. F. *J. Chem. Phys.* **1997**, *106*, 4665–4677.

[151] Voter, A. F. *Phys. Rev. Lett.* **1997**, *78*, 3908–3911.

[152] Voter, A. F.; Sørensen, M. R. *Mat. Res. Soc. Symp. Proc.* **2000**, *591*, 427.

[153] Sørensen, M. R.; Voter, A. F. *J. Chem. Phys.* **2000**, *112*, 9599–9606.

[154] Kenney, J. F.; Keeping, E. S. *Mathematics of Statistics*; Van Nostrand: Princeton,NJ, 1951.

Vita

Liang Zhang was born in Huzhou Zhejiang, China in1986. After being enrolled in the University of Science and Technology of China, he then met Ting Tan, the one he decided to devote his lifetime. In 2009, He received a Bachelor of Science degree in Chemical Physics from the University of Science and Technology of China and then was accepted to the University of Texas at Austin. After seven years of courtship, he married with Ting at Austin, Texas, in 2013.

Permanent address: lzhang@utexas.edu

This dissertation was typeset with LaTeX[†] by the author.

[†] LaTeX is a document preparation system developed by Leslie Lamport as a special version of Donald Knuth's TeX Program.